

93

Interstitial-Lymphatic Transport Phenomena

by

Melody A. Swartz

B.S. Chemical Engineering
The Johns Hopkins University
(1991)

Submitted to the
Department of Chemical Engineering
in partial fulfillment of the requirements for the degree of
DOCTOR OF PHILOSOPHY

at the
MASSACHUSETTS INSTITUTE OF TECHNOLOGY
June 1998

© 1998 Massachusetts Institute of Technology

Signature of Author: _____
Department of Chemical Engineering
April 17, 1998

Certified by: _____
Rakesh K. Jain
Professor, Harvard Medical School
Thesis Supervisor

Certified by: _____
Linda G. Griffith
Associate Professor, Department of Chemical Engineering
Thesis Supervisor

Accepted by: _____
Robert E. Cohen
St. Laurent Professor of Chemical Engineering
Chairman, Committee for Graduate Students

MASSACHUSETTS INSTITUTE
OF TECHNOLOGY

JUL 09 1998

LIBRARIES

Science

Interstitial-Lymphatic Transport Phenomena

Melody A. Swartz

Submitted to the Department of Chemical Engineering
on April 27, 1998, in partial fulfillment of the
requirements for the degree of Doctor of Philosophy

Abstract

The lymphatic system plays important roles in tissue fluid balance, protein transport, and the immune system, and has great potential for the delivery of certain drugs. Despite its importance, our quantitative understanding of interstitial-lymphatic transport is limited. The first goal of this work was to examine lymphatic function as an integral component of interstitial mechanics. A theoretical description of this mechanical equilibrium was developed in parallel with a novel experimental model. Tissue was modeled as a poroelastic continuum to describe the fluid pressure distribution following an interstitial injection, predicting that spatial gradients would be governed by the ratio of lymphatic to tissue resistances and temporal gradients governed additionally by elasticity. The mouse tail was a unique experimental model for examining both of these theoretical frameworks because of its geometry and anatomical features. Pressure measurements using micropipettes showed remarkable consistency with the theoretical assumptions and gave unique *in vivo* estimates of the effective parameter values (for tail skin, hydraulic conductivity was $1.5 \times 10^{-6} \text{ cm}^2 \cdot \text{sec}^{-1} \cdot \text{mm Hg}^{-1}$, lymphatic conductance was $4 \times 10^{-5} \text{ sec}^{-1} \cdot \text{mm Hg}^{-1}$, and the bulk elastic modulus was 110 20 mm Hg). The second part of the thesis built on this model of tissue fluid balance to describe convective transport of macromolecules. 1-D concentration gradients in the tail could be observed using fluorescence microscopy. These gradients were described in terms of a dispersivity and excluded volume fraction as well as fluid convection. The model could characterize differences in transport profiles of various molecules (differing in size, shape, and charge) and constituted an extremely useful model for *in vivo* studies of convective transport. Finally, the model was applied to studies in gene expression of the lymphatic system and to investigate the effects of edema, tissue grafting, and mechanical forces on overall lymphatic function. This is the first *in vivo* model of interstitial-lymphatic transport which accounts for the dynamics of the interstitium and allows for simple and accurate *in situ* measurements of tissue elasticity, hydraulic conductivity, and molecular transport parameters. Furthermore, it yields estimates for an effective or overall conductance of the lymphatics which is important for examining pathological changes in interstitial-lymphatic fluid.

Thesis supervisors: Rakesh K. Jain
Professor, Harvard Medical School

Linda G. Griffith
Associate Professor, Department of Chemical Engineering

Acknowledgments

I would first like to thank my thesis advisor, Professor Rakesh Jain. I value his guidance and support as well as his positive perspective. He has constantly granted me enthusiasm and confidence, always advocating my endeavors, encouraging my ideas, and showing me countless opportunities. He has supported me in every way.

I am grateful to my co-advisor, Professor Linda Griffith; my committee members, Professors David Berk (Harvard Medical School), Alan Grodzinsky (Department of Electrical Engineering), Doug Lauffenburger, and Ken Smith; and Professors Mike Karweit and Kate Stebe of Johns Hopkins. Their support, both professional as well as personal, has been invaluable.

I would also like to thank Professor Howard Brenner. He has been a true mentor, teacher, and friend throughout these 5 years.

The Steele Lab for Tumor Biology is a wonderful group of people, rich with expertise, generous with time and advice, and a lot of fun. It is a diverse group with a wide variety of knowledge and I have learned so much from them. Special thanks to Larry Baxter, David Berk, Yves Boucher, Mit Endo, Dai Fukumura, Julia Kahn, Claus Kristensen, Anders Leu, Bob Melder, Paolo Netti, Sybill Patan, Sylvie Roberge, and Fan Yuan. Also thanks to Phyllis McNally and Carol Lyons, Christian Brekken, Sue Hobbs, Gerald Koenig, Sybill Patan, Wayne Monsky, Gerald Koenig, Lance Munn, Yi Chen, and Marc Dellian. Sachiko Hirose, Talid Sinno, and Howard Covert at MIT have also given to me an endless supply of help and support.

I thank my collaborators outside the lab including Bert Losken and Sumner Slavin (Beth Israel Hospital), Annick van den Abbeele (Dana Farber), Alan Grodzinsky, Kari Alitalo (University of Helsinki), and especially Arja Kaipainen (Children's Hospital).

I thank my sisters & brothers - Wendy and D, Dan and Kell, Jim and Maria - and friends Talid, Sachiko, Arja, Kim, Kath, Chris, Pie, Stu, Mike, Enzo, Scott, Ali, Claus.

Most of all, I thank my parents. They are the greatest people in my life and I would be nothing without their support and love.

Contents

1	Introduction	12
2	Background	15
2.1	The lymphatic system	
2.1.1	Lymph formation	15
2.1.2	Lymphatic uptake of molecules and particles	18
2.1.3	Lymphatic endothelium	19
2.1.4	Methods for the assessment of lymphatic function	20
2.2	The extracellular matrix	21
2.3	Edema	22
2.4	Summary	24
3	Experimental Model and Methods	25
3.1	Introduction	
3.1.1	Lymphangiography and microlymphangiography	25
3.1.2	Mouse tail skin model	26
	<i>Model features</i>	27
3.2	Experimental setup	
3.2.1	Animals	31
3.2.2	Step increase in IFP	31
3.3	Intensity measurements	33
3.4	Flow measurements	35
3.5	Pressure measurements	
3.5.1	Wick-in-needle	37
3.5.2	Micropipette	39
3.6	Tissue are determination	39
3.7	<i>In vitro</i> mechanical tests	41

3.8	Model applications	41
4	Measurements of Flow Velocity	42
4.1	Introducion	42
4.2	Theory	
4.2.1	Macroscale (average) velocity	43
4.2.2	Microscale (local) velocity	45
4.3	Methods	
4.3.1	Macroscopic data acquisition and analysis	45
4.3.2	Microscopic data acquisition and analysis	47
4.4	Results	
4.4.1	Macroscopic velocity and the effects of injection pressure	48
4.4.2	Effects of particle size	51
4.4.3	Microscale velocity in individual capillaries using FRAP	51
4.4.4	Flow visualization using microspheres	56
4.5	Discussion	57
5	Interstitial-lymphatic fluid balance	61
5.1	Introduction	61
	<i>Modeling foundation</i>	64
5.2	Theory	
5.2.1	General	65
5.2.2	Application to the experimental model	71
5.2.3	Special case of oscillating pressure	74
5.2.4	<i>In vitro</i> elastic modulus	75
5.3	Results	
5.3.1	Tissue fluid balance parameters	75
5.3.2	<i>In vitro</i> parameters	81
5.3.3	Oscillating surface pressure simulations	81
5.4	Discussion	83
5.4.1	Hydraulic conductivity	84
5.4.2	Tissue elasticity	85
5.4.3	Net lymphatic conductance	86
5.4.4	Distribution of hydration and fluid velocity	87
5.4.5	Assumptions and limitations	88

5.5	Alternative methods	
5.5.1	Theory	89
5.5.2	Methods	90
5.5.3	Results and implications	91
5.6	Conclusions	93
6	Convective interstitial-lymphatic solute transport	94
6.1	Introduction	94
6.2	Background	96
6.3	Solute convection	97
6.4	Convection and adsorption of solute	102
6.5	Dispersive effects	
6.5.1	General	105
6.5.2	Constitutive equations and variable definitions	106
	<i>Effective solute velocity</i> U^*	107
	<i>Effective dispersivity</i>	109
	<i>Lymphatic drainage</i>	111
6.5.3	Conservation equation	111
	<i>Simulations</i>	112
6.6	Experimental data	122
6.7	Analysis and discussion	
6.7.1	Net solute velocity	124
6.7.2	Spatial profiles	128
6.8	Conclusions	129
7	Model Applications	130
7.1	Introduction	130
7.2	Surgical models of lymphedema and tissue flap transfer	
7.2.1	Background	131
7.2.2	Methods	
	<i>Experimental groups</i>	131
	<i>Lymphatic ligation</i>	132
	<i>Myocutaneous tissue flap transfer</i>	132
	<i>Lymphoscintigraphy (LS)</i>	133
	<i>Fluorescence microlymphangiography (FM)</i>	134

7.2.3	Results	
	<i>Establishment of lymphedema</i>	135
	<i>Lymphatic continuity demonstrated by LS</i>	138
	<i>Flow patterns visualized by FM</i>	140
	<i>Evaluation of tissue fluid balance parameters</i>	142
7.2.5	Discussion	145
7.2.5	Physiological implications	146
7.2.6	Clinical implications	147
7.3	Lymphatic hyperplasia	148
8	Conclusions	151
	Appendices	155
A	Nomenclature	155
B	Experimental data: pressure propagation	158
C	Experimental data: solute transport	161
	Bibliography	168

List of Figures

1-1	Flow diagram of thesis outline	14
2-1	Cartoon depicting the blood-tissue-lymph interface	16
2-2	The lymphatic capillary cross-section and its anchoring filaments	18
2-3	Congenital lymphedema of the leg	23
3-1	Microlymphangiography in the mouse tail	27
3-2	Cross section of a mouse tail	29
3-3	Roentgen-photograph of the lymphatic pathways of the rat tail	30
3-4	Experimental setup for a constant pressure infusion into the mouse tail skin	32
3-5	Imposed fluid velocity vs. measured bubble velocity in the bubble flow meter	36
3-6	Wick-in-needle setup to measure IFP	37
3-7	Pressure recordings to test fluid communication in the wick-and-needle setup	38
3-8	Matrix protein density in the mouse tail	40
4-1	Staining of the lymphatic network measured by fluorescence intensity	44
4-2	Representative MRT vs. distance data for each injection pressure	49
4-3	The photobleaching and subsequent recovery of fluorescent material in a lymphatic vessel	52
4-4	Spatial Fourier analysis of FRAP images	53
4-5	Instantaneous velocity within two individual capillaries as a function of time	54
4-6	Relation between velocity magnitude and time of dye infusion	55
4-7	Images of fluorescent microspheres in the superficial lymphatic capillaries	56
5-1	Mechanical aspects of tissue fluid balance	63
5-2	IFP at 3.2 mm following a step infusion of saline at 52 cm water	64
5-3	Spatial pressure profile following establishment of steady state	76
5-4	Typical data showing dependence of infusion flow rate on infusion pressure	77
5-5	The transient IFP profile at 3.2 mm and its fit to Equation 5.19	78
5-6	Sensitivity analysis of the transient pressure profile	80
5-7	Comparison of constant vs. oscillating pressure at the boundary $x=0$. (a) Pressure vs. normalized time (b) flow rate vs. time (c) total uptake vs. time	82

5-8	Position of the “leading edge” of fluorescent solute or moving front with time	91
5-9	Length of infusion, as measured by the saturation of the interstitium with fluorescent tracer (FITC-Dx 2M), vs. $\ln(P_o^*)$	92
6-1	Spatial profiles of FITC-Dextran 2M	95
6-2	Relationship between injection pressure and “characteristic uptake time”	97
6-3	(a): Concentration vs. time for several distances as predicted by Eq. 6.4. (b): Steady-state concentration profiles and the effects of varying the parameters ζ , and σ_L .	101
6-4	Spatial profiles described by Equation 6.9 using the same parameter values as before (see Figure 6-3 legend)	104
6-5	Transient development of interstitial fluid pressure (IFP) and solute concentration at a point approximately 3 mm from infusion	109
6-6	Graphical representation of Equation 6.23	
	(a) Baseline parameter values of $A=1.0$ mm, $\phi/\varepsilon=2$, and $(1-\sigma_L)/\varepsilon=3.3$	112
	(b) A is decreased to a value of 0.1 mm	113
	(c) A is increased to a value of 5 mm	114
	(d) ϕ/ε is increased to a value of 2.67	115
	(e) ϕ/ε is decreased to a value of 1.0	116
	(f) σ_L is increased to a value of 0.1	117
	(g) σ_L is increased to a value of 0.3	118
6-7	Spatial profiles of each case shown in Figures 6-6 (a)-(g) at one hour	121
6-8	Solute concentration profiles for two co-injected molecules at 10 minutes	123
6-9	Mean distance vs. time for FITC-Dx 2M and TR-Dx3K	125
6-10	Mean solute transport profiles for each of the cases in Figure 6-6	127
7-1	Myocutaneous flap design	133
7-2	<i>Left:</i> sham flap control without ligation (B5). <i>Center:</i> flap with lymphatic ligation (B2). <i>Right:</i> ligation-only animal (B1)	136
7-3	Average tail diameter increases for the experimental groups	137
7-4	Lymphatic vessels and nodal groups in mice as evaluated by LS	139
7-5	Fluorescent images of the cutaneous lymphatic network near the base of the tail following an interstitial infusion of FITC-Dextran 2M at the tail tip	141
7-6	Representative data for infusion pressure vs. infusion flow rate for each experimental group	143

7-7	Representative data for infusion pressure vs. length of interstitial “front” for each experimental group	143
7-8	Parameters <i>IFP</i> , <i>IFV</i> , <i>K</i> , and β relative to the normal controls	144
7-9	Fluorescent microlymphangiography images of the superficial capillary network of normal and transgenic mouse tail skin	149
B-1	(a)-(e) Transient pressure profiles of each experiment used in Chapter 5	158
C-1	(a)-(c) Spatial profiles of anionic FITC-Dx 3K with TR-Dx 3K	161
C-2	(a)-(c) Spatial profiles of FITC-Dx 71K with TR-Dx 3K	163
C-3	(a)-(c) Spatial profiles of FITC-Dx 2M with TR-Dx 3K	164
C-4	(a)-(c) Spatial profiles of FITC-BSA with TR-Dx 3K	166

List of Tables

4.1	Network velocity analysis data for injection pressures of 10 and 40 cm H ₂ O .	50
5.1	Results of 6 experiments with infusion pressures of 40-60 cm water	79
6.1	Summary of the coefficients used for Figures 6-6(a)-(g) with corresponding effective parameter values and implications for fast times	121
6.2	Average solute volume fraction relative to that of the standard for four different macromolecules	127
6.3	Data analysis according to the adsorption model presented in Section 6.4 . .	129
7.1	Averaged parameter values from all groups at ten days	144

Chapter 1

Introduction

The lymphatics comprise a one-way transport system which is parallel to that of the blood circulation. Its main function is to drain fluid and proteins from the interstitial space and return them to the blood circulation. Lymph forms as fluid and molecules are driven from the interstitium into the lymphatic capillaries (also called initial lymphatics) by hydrostatic and osmotic pressure differences, and imbalance in the interstitial-lymphatic complex can result in edema. Proteins and other macromolecules depend on the lymphatics for interstitial clearance and systemic transport. Furthermore, any molecules or particles traveling in the lymphatics pass through lymph nodes - reservoirs in which material can be filtered and examined by white blood cells - yielding important immunological consequences. Despite its importance, our physical understanding of lymph formation is inadequate for application. For example, edema remains an untreatable condition, and the clinical potentials of lymphatic drug delivery and targeting are largely unexplored. While numerous aspects of blood flow have been studied extensively, tools for studying lymphatic function are lacking and lymphatic transport remains largely ignored by the bioengineering community.

A comprehensive and quantitative model is necessary to gain a better understanding of interstitial fluid balance and the role of the lymphatics in maintaining this fluid balance. Such a model would also be required to exploit the increasing potential of lymphatic drug delivery (Charman *et al* 1992). Furthermore, the recent discovery of the first growth factor for lymphatic endothelium (Jeltsch *et al* 1997) has ignited interest in lymphatic cell biology; its relevance in lymphatic (tumor) metastasis and edema also motivates a quantitative functional model.

The work presented in this thesis outlines (1) the development of the mouse tail as an experimental model for quantitative investigations into interstitial-lymphatic transport, (2) the parallel development of a theoretical framework to describe fluid and solute transport in this experimental model, and (3) some applications of the model to relevant physiological issues. This is diagrammed in Figure 1-1. After a brief summary of the background in Chapter 2, Chapter 3 describes the experimental model and the techniques which were used for various measurements. Chapter 4 examines flow within the lymphatic capillary network both on an averaged scale using residence time distribution theory as well as locally using photobleaching methods. Chapter 5 investigates interstitial-lymphatic mechanics by evaluating the mechanical response to a perturbation in tissue stress. Interstitial solute transport is examined in Chapter 6, building on the mechanical framework of Chapter 5 along with convective-dispersive theory. Finally, Chapter 7 describes the application of the model along with surgical techniques and the tools of molecular biology to evaluate changes in tissue fluid balance during lymphedema, tissue grafting, wound healing, and lymphatic hyperplasia.

In all these studies, tissue is treated as a “packed bed” for analyses of fluid and macromolecular transport. Modeled as a porous fluid-filled elastic medium, pressure gradients can be measured to estimate fluid transport parameters *in situ*. Modeled as a chromatography column, resistances to interstitial and lymphatic transport of macromolecules can be estimated. Coupled with the potentials of surgical and genetic alterations and measurements of gene expression, this constitutes a very powerful tool for simultaneous studies of nearly every aspect of interstitial-lymphatic transport.

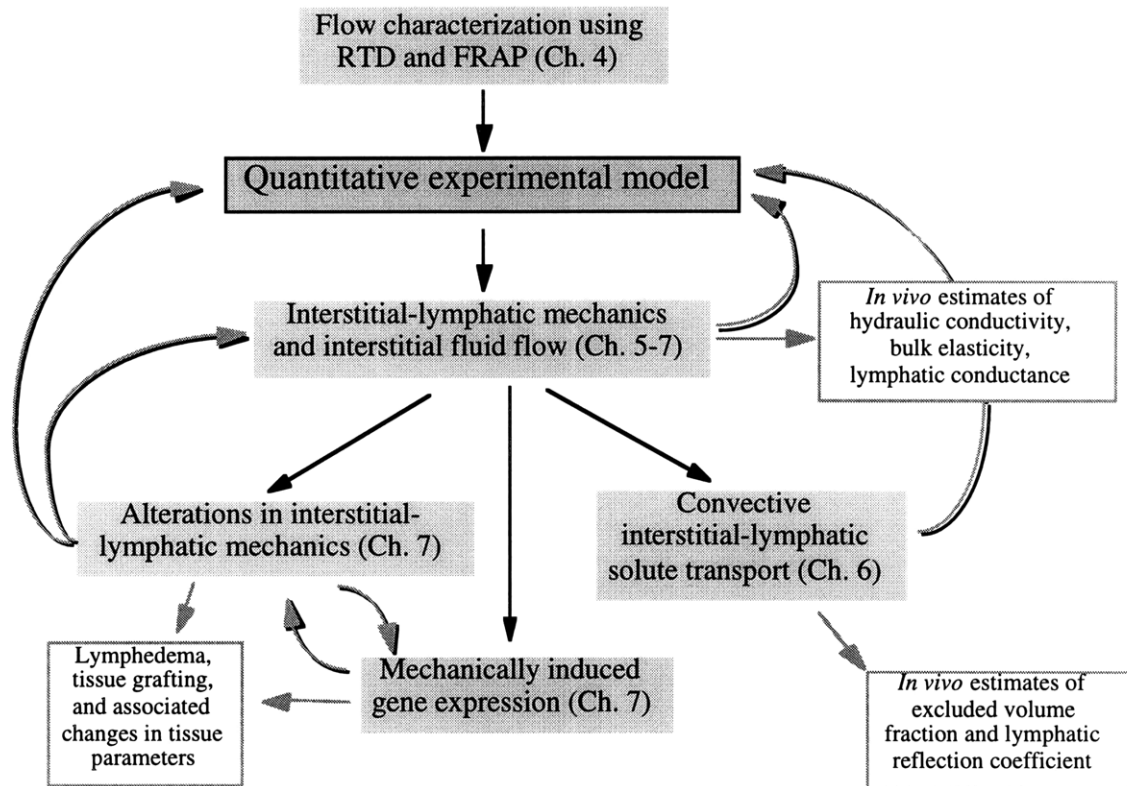


Figure 1-1. Flow diagram of thesis outline.

Chapter 2

Background

2.1 The lymphatic system

2.1.1 Lymph formation

The lymphatics comprise a one-way transport system for fluid and proteins which are collected from the interstitial space and returned to the blood circulation. The terms "lymphatic capillaries" or "initial lymphatics" are used to describe the blind-ended structures in which lymph initially forms. The simplified relation between blood, interstitium, and lymph is depicted in Figure 2-1. As blood travels from the branching arteries down to the smallest capillaries, plasma and proteins are forced out into the interstitial space or interstitium (the tissue space not occupied by cells). Most of this fluid gets reabsorbed into the post-capillary venules, but a small fraction remains in the tissue due to osmotic forces resulting from the leakage of proteins. This excess is drained by the initial lymphatics, which are more permeable to macromolecules than the interstitium and thus serve a crucial role in maintaining osmotic and hydrostatic pressures within the tissue space. Finally, the cell entering the lymphatic in Figure 2-1 signifies the importance of the lymphatic system for the transport (and residence) of white blood cells and sometimes metastasizing cancer cells.

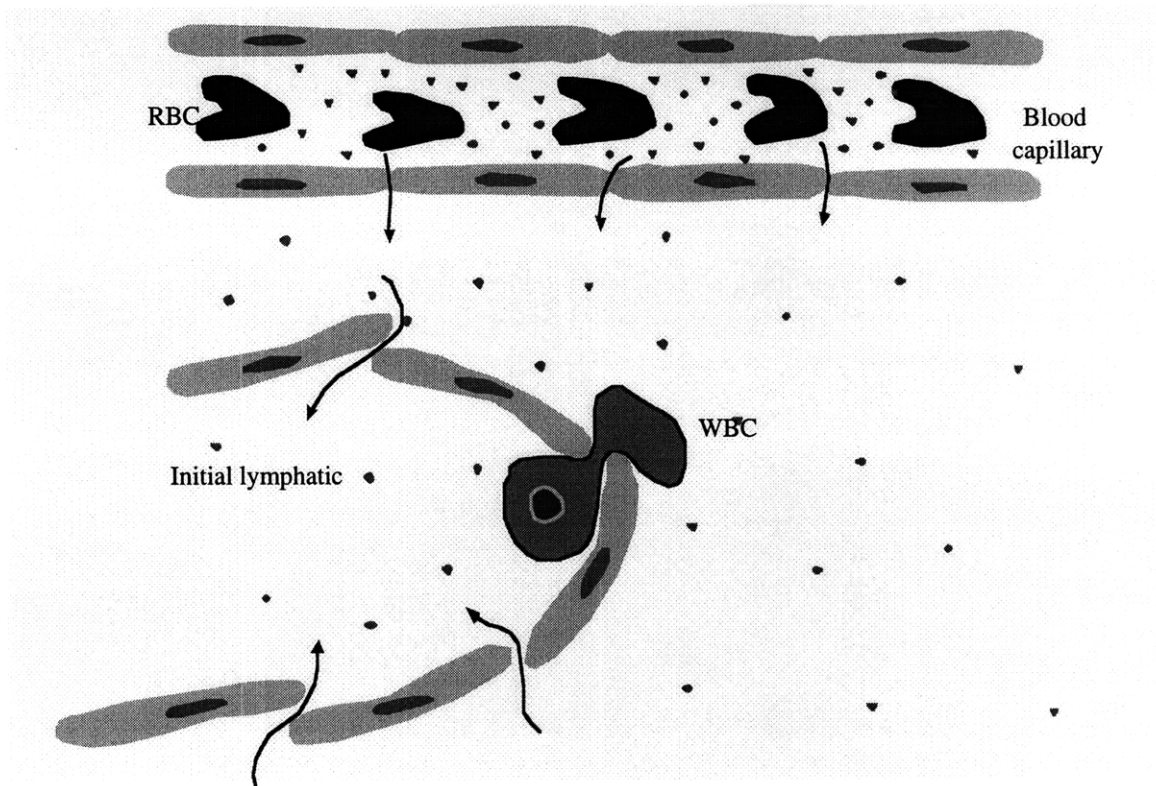


Figure 2-1. Cartoon depicting the blood-tissue-lymph interface. RBC = red blood cell; WBC = white blood cell.

Lymph formation is presumably driven by hydrostatic pressure differences and controlled by a permeability or conductance. Starling's Law is the equivalent of Darcy's Law for fluid flux into or out of a vessel (J_v) and has been used for over 100 years to describe lymph formation:

$$J_v = L_p \frac{S}{V} (\Delta P - \sigma \Delta \pi) \quad (2.1)$$

where L_p is the permeability, S/V is the surface-area-to-volume ratio, ΔP and $\Delta \pi$ are the local hydrostatic and osmotic pressure differences across the lymphatic capillary wall,

respectively, and σ is the capillary osmotic reflection coefficient. For the lymphatics, $\Delta\pi$ is typically considered negligible compared to ΔP because lymphatic vessels have overlapping junctions between endothelial cells and thus permeability to solute molecules is high (Schmid-Schönbein 1990, Hammersen and Hammersen 1985, Castenholz 1984, Leake and Burke 1966). While Starling's Law may hold true, it is not useful for evaluating experimental data because (1) L_p strongly depends on the state of stress of the tissue, and (2) the high permeability of the lymphatic capillaries results in a very small driving force for lymph formation (ΔP). Reddy *et al* (1975) proposed that the pressure within the initial lymphatics (P_L) mimicks that of the tissue (P_T) according to the hoop stress, σ_{hoop} , which depends on various properties of the lymphatic vessel such as its elastic modulus and unstressed radius:

$$P_L = P_T + \frac{h}{a} \sigma_{hoop} \quad (2.2)$$

where h and a are the thickness and instantaneous radius of the vessel, respectively. However, this is an oversimplified description: it does not account for natural stress oscillations or the oscillations in L_p , and moreover, the initial lymphatics are *not* cylindrical in their unstressed state. The fact that the initial lymphatic is an integral part of the interstitium is ignored, which is a common mistake in mathematical descriptions of lymph formation.

The interstitial-lymphatic interface is depicted in Figure 2-2. Since they have no smooth muscle or basement membrane (Schmid-Schönbein 1990) and are often found in a collapsed or partially collapsed state, the lymphatic capillaries rely on sensitive connections to the extracellular matrix (ECM) called anchoring filaments. These fibers strongly attach the basal lamina to adjacent collagen fibers (Leak and Burke 1966, Leak 1970) which have similar structure and composition to the elastin components of the ECM (Gerli *et al* 1991) Responding to slight tissue stresses, they exert radial tension on the lymphatic endothelial cells and pull the capillary towards a cylindrical shape to facilitate lymph formation. This creates a slight vacuum into which fluid may be drained. Since most natural stresses within the tissue are oscillatory, this mechanism is adequate for the relatively small volumetric rate of lymph formation.

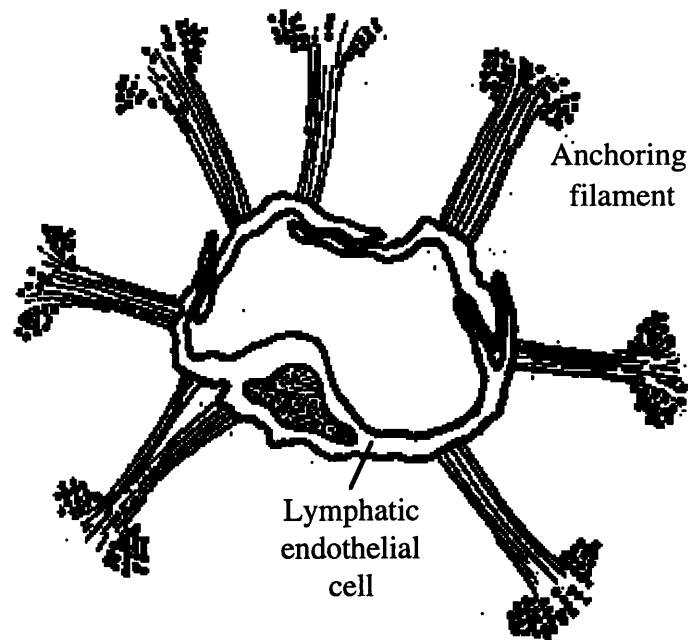


Figure 2-2. Drawing of the lymphatic capillary cross-section and its anchoring filaments (not to scale). Courtesy of Arja Kaipainen.

Following lymph formation, lymph flows from the initial lymphatics or capillaries to the collecting lymphatics, which have some smooth muscle and one-way valves to aid in lymph propulsion. These valves are critical in lymph flow, since the lymphatic system does not have a central pump as does the blood circulation. Furthermore, lymph flows at low Reynolds numbers (Schmid-Schönbein 1990, Fung 1984) and therefore the valves prevent retrograde flow. Most valves are bicuspid (Ohtani *et al* 1986, Fabian 1983, Gnepp 1976, Lauweryns 1971, Takada 1971, Kampmeier 1928) to facilitate such slow flow. Details of the collecting lymphatics and larger vessels are described in a recent review by Schmid-Schönbein (1990).

2.1.2 Lymphatic uptake of molecules and particles

It is believed that size is the most important determinant of lymphatic uptake (Bergqvist *et al* 1983) and lymph node retention (Charman *et al* 1992). Molecules which

are smaller than 10 nm are preferentially reabsorbed into the blood capillaries, but the optimal size for lymphatic uptake is between 10 and ~100 nm. Molecules or particles up to 1 μm may be taken into the lymphatics, but above 100 nm, a percentage of injected solute will remain trapped in the interstitial spaces for longer periods of time and thus have lower uptake efficiencies. For example, liposomes of 30-60 nm were found to have faster uptake rates than those of 400 nm, but the smaller ones also showed higher level in the blood circulation (Strand and Bergqvist 1989).

The composition of the molecule or particle is also important in determining uptake and lymph node retention. Colloids and liposomes seem to improve uptake efficiency. Colloidal carbon has been suggested for lymphatic drug delivery applications because of its apparent benefit to lymphatic uptake. Anticancer drugs absorbed to colloid carbon particles of 200 nm showed markedly increased lymph node levels than those obtained with solutions of the same drugs (Hagiwara *et al* 1989, Hagiwara and Takahashi 1987, Hagiwara *et al* 1985); furthermore, the activated carbon enhanced preferential adherence to malignant cells and slowed release characteristics. Lipophilicity has also been associated with uptake efficiency (Torchilin 1996, Hirano *et al* 1985, Tumer *et al* 1983, Jackson 1981). Depending on the size, charge, method of preparation, and composition, various molecules such as monoclonal antibodies, peptide drugs, and anticancer agents may be encapsulated into liposomes and optimally targeted to lymph nodes (Charman *et al* 1992, Hirano *et al* 1985, Mangat and Patel 1985, Ohsawa *et al* 1985, Weinstein 1984, Ryman *et al* 1978). Furthermore, the liposome can be coated (e.g. with polyethylene glycol) to improve lymph node retention by avoiding white blood cell phagocytosis; such "stealth" liposomes are well-characterized and can be designed for a number of specific purposes (Torchilin 1996). Microspheres of various materials have also been shown to be effective drug carriers which can be targeted to lymph nodes; for example, microspheres of L-lactic acid oligomer are stable, nontoxic, biodegradable, and show good release characteristics (Yoshikawa *et al* 1989).

2.1.3 Lymphatic endothelium

There are many similarities between endothelium of blood vessels and that of lymphatics. For example, the requirements and characteristics of cell growth are similar (Yong and Jones, 1991) and lymphocyte binding to lymphatic endothelial cells is not significantly different from binding to venous or arterial endothelial cells (Borron and Hay 1994). With respect to morphogenetic properties, lymphatic endothelial cells

behave similarly to vascular endothelial cells *in vitro*. They both exhibit spontaneous angiogenesis, and they both respond to bFGF and VEGF similarly (Pepper *et al* 1994), express anti-thrombin 3 and von Willebrand factor on their surfaces, and actively metabolize acetylated low density lipoprotein (Borron and Hay 1994).

The endothelia of the lymphatic capillaries differ from those of the blood in that they have little or no basement membrane, overlapping cell junctions, and anchoring filaments which adhere to the surrounding collagen fibers of the ECM. Therefore they may be distinguishable by staining for the structural proteins of the basement membrane, such as collagen IV and laminin (Barsky *et al* 1983). Furthermore, histological distinctions include the use of 5'-nucleotidase (5'Nase), which is specific for lymphatic endothelium, along with alkaline phosphatase (ALPase) or guanylate cyclase (GC) for blood endothelium (Endo *et al* 1994, Yoshizawa *et al* 1994). Finally, it has been shown that an fms-like tyrosine kinase receptor, Flt4 (also called vascular endothelial growth factor receptor-3, or VEGFR-3), becomes restricted to the lymphatic endothelium during development (Kaipainen *et al* 1995). Receptors of the tyrosine kinase family are known to play important roles in the proliferation, migration, and permeability of endothelial cells (Ullrich and Schlessinger 1990, Folkman and Klagsbrun 1987). This particular receptor is activated by the lymphatic-specific vascular endothelial growth factor VEGF-C (Jeltsch *et al* 1997). Therefore Flt4 can be used to identify lymphatic endothelial cells.

2.1.4 Methods for the assessment of lymphatic function

Transport studies in lymphatic capillaries have been limited by the lack of an appropriate quantitative *in vivo* model. Cannulation of small vessels is technically difficult and highly invasive. Lymphatic function is usually characterized by the tissue clearance rate, which describes the removal of labeled molecules or colloids in terms of amount per unit time per unit tissue volume. This method is straightforward and provides a relative or semi-quantitative measure of lymphatic function (Mortimer *et al* 1990, Hollander *et al* 1961). Lymph formation can be observed in skin and mesentery by injecting an optical contrast agent such as mercury (Mandell *et al* 1993, McNeill 1989, Engeset and Tjötta 1960, Hudack and McMaster 1933) or fluorescently labeled macromolecules (Castenholz 1991, Bollinger *et al* 1981). This procedure is commonly termed microlymphangiography and can provide a clinical diagnostic tool for the characterization of edema (Bollinger and Fagrell 1990). Other methods for evaluating lymphatic function include measurements of plasma-to-lymph clearance (Renkin and Wiig 1994, Mortimer *et al* 1990) and local

measurements of lymphatic capillary pressures (Ikomi *et al* 1997, Wen *et al* 1994, Bates *et al* 1994, Zaugg-Vesti *et al* 1993, Zweifach and Prather 1975).

While these methods are useful both experimentally and clinically in understanding lymphatic function and edema, they have limited use in identifying and exploring the dynamics of lymph formation and the physiological variables which govern lymphatic function. Specifically, they present a lumped or grossly macroscopic picture of the entire interstitial-lymphatic system. For example, the local uptake of an injected solution is the net result of both tissue and lymphatic transport processes whose initial equilibrium is disturbed by the injection in undefined ways, and as such, a measurement of the overall uptake rate alone cannot elucidate the mechanisms by which lymphatic uptake occurs.

2.2 The extracellular matrix

The composition and organization of the extracellular matrix (ECM) determines the properties of a tissue such as its elasticity and strength. Collagen fibers give structural stability and form the skeletal framework onto which tissue is composed. Elastin provides elastic properties. Glycosaminoglycans (GAGs) are highly negatively charged macromolecules which “glue” the other matrix proteins together and imbibe water. It makes up a gel-like phase together with water and interstitial proteins. GAGs are commonly correlated to interstitial fluid transport resistance (Jackson *et al* 1991, Levick 1987, Granger 1981) and a disruption of normal GAG composition is ascribed to arthritis in articular cartilage (Mow 1984, Grodzinsky 1983) as well as loss of tissue elasticity associated with lymphedema (Negrini *et al* 1996). The composition and structure of the interstitium has been extensively reviewed by others (Jackson *et al* 1991, Levick 1987, Grodzinsky 1983, Granger 1981, Hargens 1981).

In skin, the random organization of collagen fibers and high GAG content govern its mechanical properties (Granger 1981, Markenscoff and Yannas 1979, Craik and McNeil 1965, Kenedi *et al* 1965). Skin typically contains approximately 20% collagen, 40% water, and 0.3% GAG (Aukland and Reed 1993), two-thirds of which is hyaluronic acid or hyaluronan (HA). HA is synthesized by fibroblasts (Prehm 1984) and has a molecular weight of several million (Preston *et al* 1984) but is routinely broken down with mechanical strain or age (Negrini *et al* 1996, Lebel *et al* 1989, Laurent and Granath 1983). Turnover of HA is on the order of one day (Laurent *et al* 1991, Reed *et al* 1990), and removed by the lymphatic system. Therefore HA is critical to tissue fluid balance and elasticity, and is of major importance in edema.

2.3 Edema

Edema is a condition of tissue fluid imbalance often resulting from infection, trauma (from burns or radiation), surgery, and tissue grafting and transplantation (Mortimer 1997). It can also be congenital as shown in Figure 2-3. Although edema affects millions of people, it is virtually untreatable. Attempts at treatment have included drug therapy, physical therapy, and surgical approaches; these have yielded little success, particularly in the long term (Mortimer 1997, Campisi *et al* 1995, Baumeister *et al* 1990, Savage 1984, Huang *et al* 1985).

The pathological basis of edema can be described by considering lymph formation as a passive process which is intrinsically linked to interstitial fluid movement and governed by mechanical forces. The first step in the development of edema is an offset in the mechanical equilibrium. This can occur by a blockage of the lymph node, buildup of osmotic forces within the interstitium, damage to the interstitial-lymphatic connections, or change in the mechanical properties or composition of the ECM.

The lymph nodes can typically become blocked by infection, tumor metastasis, or surgical removal. Post-mastectomy edema is a common ailment of breast cancer patients. This essentially severs the lymphatic network in the limb or region which led to that node with the systemic lymph flow. The initial lymphatics maintain their drainage capacity, but become “backed up” when lymph cannot drain from the deeper collecting vessels. As a result, there is no driving force for lymph formation and tissue swelling results.

A change in oncotic pressure can result from hyperpermeability of the blood microcirculation. This has been treated with some success using drugs of the benzopyrone family such as Coumarin (Casley-Smith *et al* 1993, Casley-Smith 1992). These drugs stimulate proteolysis by macrophages and thus effectively reduce oncotic pressure within the interstitium. However, sustained edema elicits ECM reorganization by fibroblasts, leading to an overall decrease in tissue elasticity. This can also cause protein accumulation, which exacerbates the problem (Negrini *et al* 1996, Casley-Smith and Gaffney 1981).

Thus, edema is a serious problem and its treatment has seen little progress. Surgical techniques have mostly failed (Mortimer 1997, Campisi *et al* 1995, Baumeister *et al* 1990, Savage 1984, Huang *et al* 1985) and the benzopyrone drugs are not approved for use in the United States. This lack of progress is mostly due to deficiencies in adequate models and in

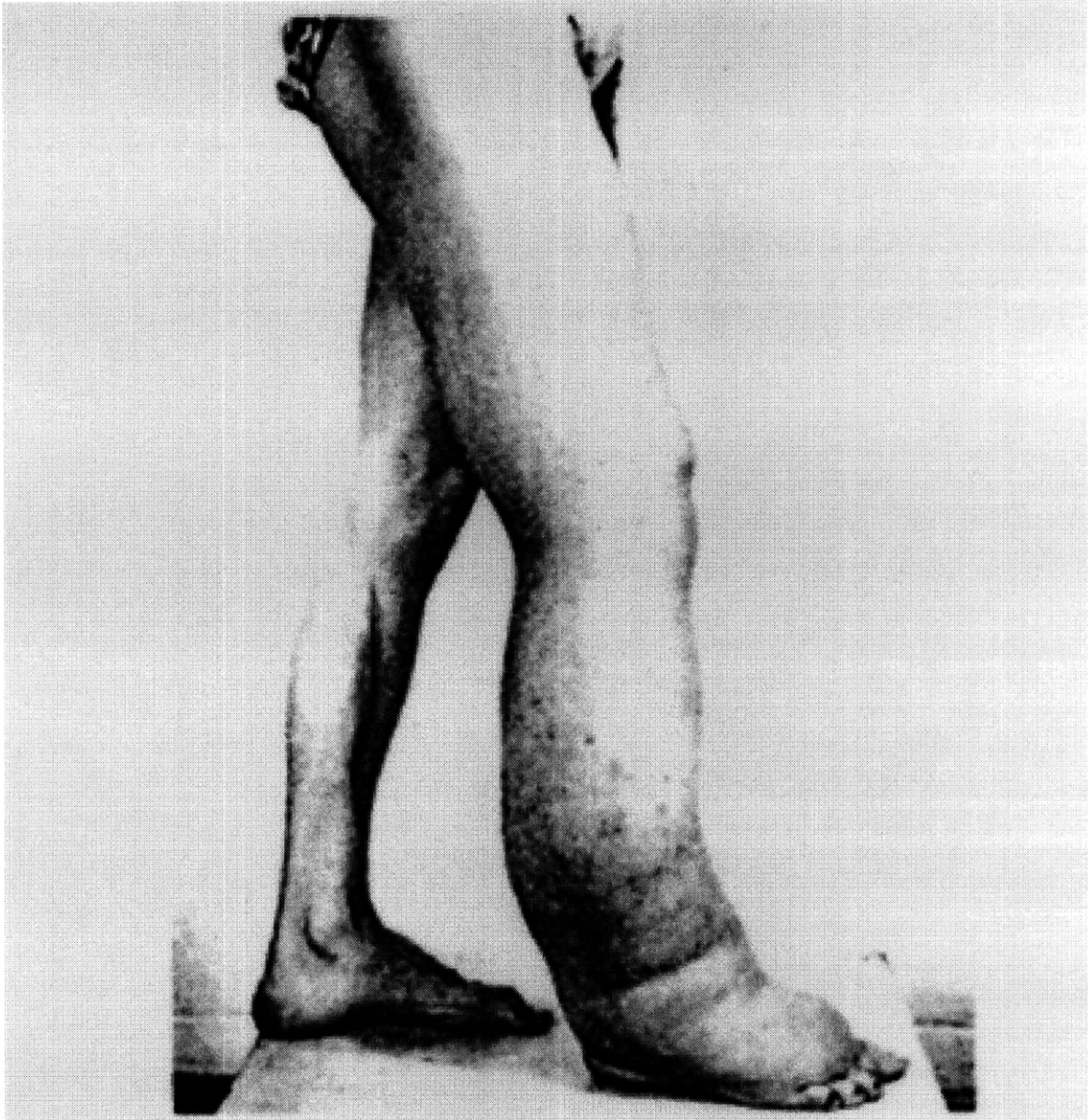


Figure 2-3. Congenital lymphedema of the leg.

our understanding of interstitial-lymphatic mechanics and lymphatic cell biology. Because of this, there is little basis for rational therapeutic approaches (Mortimer 1997).

2.4 Summary

The formation of lymph and the uptake of solute into the lymphatic system is not well understood, particularly in relation to the interstitium. This is evidenced by (1) the lack of treatment options for conditions like edema and diseases of the lymphatic system; (2) the poor level of understanding of lymphatic cell biology and its relation to tissue fluid balance on a macroscopic scale; (3) the fact that lymphatic drug delivery is not fully realized despite its great potential; and most of all, (4) the lack of experimental and theoretical models which can be used to study interstitial-lymphatic transport. As this thesis attempts to address these issues, the literature is reviewed and discussed in relation to the experimental and theoretical developments.

Chapter 3

Experimental Model and Methods

3.1 Introduction

The first step in this thesis work was to develop an experimental model which was well-defined and could yield quantitative and reproducible measurements of interstitial-lymphatic transport. This section describes the evolution of such a model, and introduces its uses and applications which ensued. As will be shown in subsequent chapters, the model surpassed expectation in its usefulness and diversity in elucidating function, mechanics, and gene expression simultaneously and *in situ*.

3.1.1 Lymphangiography and microlymphangiography

As described in Chapter 2, the technique of lymphangiography allows lymphatic vessels to be visualized by interstitial injections of an optical, radioactive, or fluorescent contrast agent. Microlymphangiography refers to the specific staining of lymphatic *capillaries* (or initial lymphatics) following an intradermal injection. This technique can readily give some qualitative information about the state of tissue fluid balance. Consider the following cases: (1) normal tissue, (2) tissue which has decreased elasticity, (3) tissue in which the initial lymphatics are not functioning properly, and (4) tissue in which the lymph nodes are blocked so that the collecting lymphatics are not draining properly.

In normal tissue, the injection of contrast agent creates a local, temporary perturbation in tissue stress. Tension on the anchoring filaments opens up the initial lymphatic vessels and facilitates local uptake of the contrast agent. In this way the initial lymphatics are rendered visible to the extent in which drainage to the deeper collecting vessels takes over.

For the second case, a decreased elasticity could be due to a number of reasons including chronic edema or some other mechanisms of extracellular matrix (ECM) degradation. With a “loose” or less structured ECM, local increases in tissue stress which would normally facilitate drainage are now greatly reduced and therefore the driving force for lymph formation is weak. Microlymphangiography would show slower network staining and a greater interstitial deposit of contrast agent.

The third case of abnormally functioning lymphatics is often seen in lymphangioma, where the endothelial cells of the initial lymphatics proliferate in an exaggerated manner and lose their sensitivity to tissue stress or swelling. In such distended vessels, small perturbations in tension do not appreciably “open up” the vessels to facilitate filling. They simply adjust their shape rather than increase their cross-sectional area. For this case, microlymphangiography would show little or no filling and only an interstitial deposit.

Finally, the blockage of lymph nodes are common as a side effect of cancer therapies such as radiation or surgery as well as a primary effect of lymph node tumors. When the lymph nodes are blocked, local vessels can still collect fluid in the normal manner but they cannot drain to deeper vessels which have nowhere to move fluid. In such a situation, microlymphangiography often results in the staining of a much more extensive superficial network (Bollinger and Fagrell, 1990). That is, since they cannot drain to the collecting lymphatics, they continue to travel through the capillary network and stain a much greater network portion than normal.

Therefore, with a simple observation of an interstitial injection, uptake efficiency and drainage to deeper vessels can be qualitatively estimated by the area and pattern of visible network. Fluorescence microlymphangiography is emerging as a clinical diagnostic tool to characterize edema and speculate cause (Bollinger and Fagrell 1990).

3.1.2 Mouse tail skin model

Microlymphangiography as described by Bollinger has a limitation, however, of quantification. First, a bolus injection is not perfectly reproducible, and the drainage to deeper vessels limits the extent of visible network in tissues such as the foot or hand (limbs are most commonly prone to edema). Therefore in order to develop this into a quantitative technique, an appropriate animal model was needed along with some control and reproducibility.

Dr. Anders Leu first discovered the lymphatic network of the mouse tail skin while looking for such a model. The technique of fluorescence microlymphangiography was

adapted to the tail skin of the mouse to visualize the lymphatic capillary network there (Leu *et al* 1994). The mouse tail exhibited a strikingly regular hexagonal network which, following injection into the tip of the tail, filled in an approximately one-dimensional manner as shown in Figure 3-1.

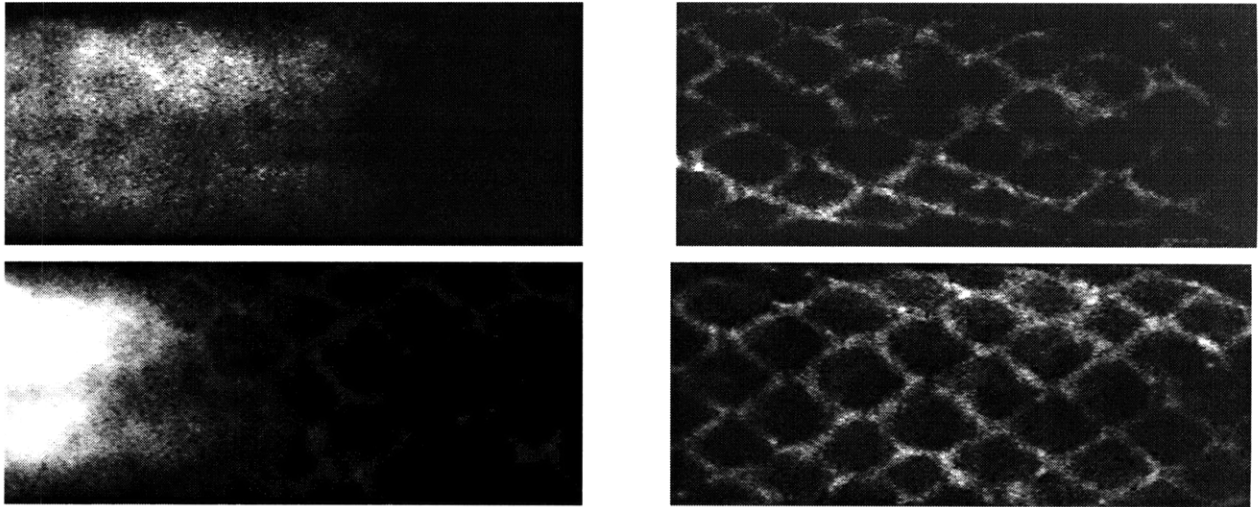


Figure 3-1. Microlymphangiography in the mouse tail. *Top left:* An injection of FITC-Dx 2M (0.0125 g/ml) at the tip of the tail fills the surrounding interstitial space according to the amount injected, rate of injection, fluid conductivity of the tissue, and functioning of the lymphatics. *Bottom left:* The capillaries become visible as the lymphatics drain and transport the fluid away from the injection deposit. *Top right:* Downstream from the injection, the network continues to appear in a dispersed manner according to the overall propulsion speed in the lymphatic capillary network. *Bottom right:* After approximately 30-60 min, the entire lymphatic network is visible for approximately two-thirds of the tail length. Mesh diameter is approximately 400 microns.

Model features

The mouse tail model exhibited several features which made it conducive to quantitative studies of interstitial-lymphatic transport phenomena. For example, an injection at the tail tip allowed transport only in the proximal direction (i.e. toward the animal), first within the tissue interstitium and then within the lymphatic network. This is a painless procedure which requires anesthesia only to immobilize the animal for observation; it is also relatively noninvasive and the animal can be observed repeatedly for several months. Furthermore, a cross-section of the mouse tail, shown in Figure 3-2, demonstrates that the

tail is essentially an annulus of dermal and subcutaneous tissue (skin) surrounding a core of bone and tendons . There are many other tissues seen in this cross-section, such as hair follicles, sebaceous glands, and the epidermis, but injected fluid is not likely to flow through these tissues since the dermis and subcutis have a much lower hydraulic conductivity (Levick 1987). As such, interstitial transport of the material which is injected intradermally occurs in a fairly homogeneous tissue and mostly in one direction. (This can also be shown by a simple scaling analysis; see Section 5.3 where radial gradients in pressure and stress are shown to be negligible compared to axial ones.)

Another favorable feature of tail skin lymphatics is shown in Figure 3-3. Using mercury injections, Engeset first demonstrated the lymphatic pathways in the rat tail (Engeset and Tjøtta, 1960). The superficial vessels (not visible here) drain to two deeper vessels which lead to the ischial lymph nodes near the base of the tail. In this way, the system is essentially contained and can become closed with the ligation or blockage of these lymph nodes. This is used to create edema in the tail and is examined in Chapter 7. These features, along with the variety of observation techniques which will be explored throughout this thesis, render the model unique both for quantitative physiological studies as well as theoretical modeling.

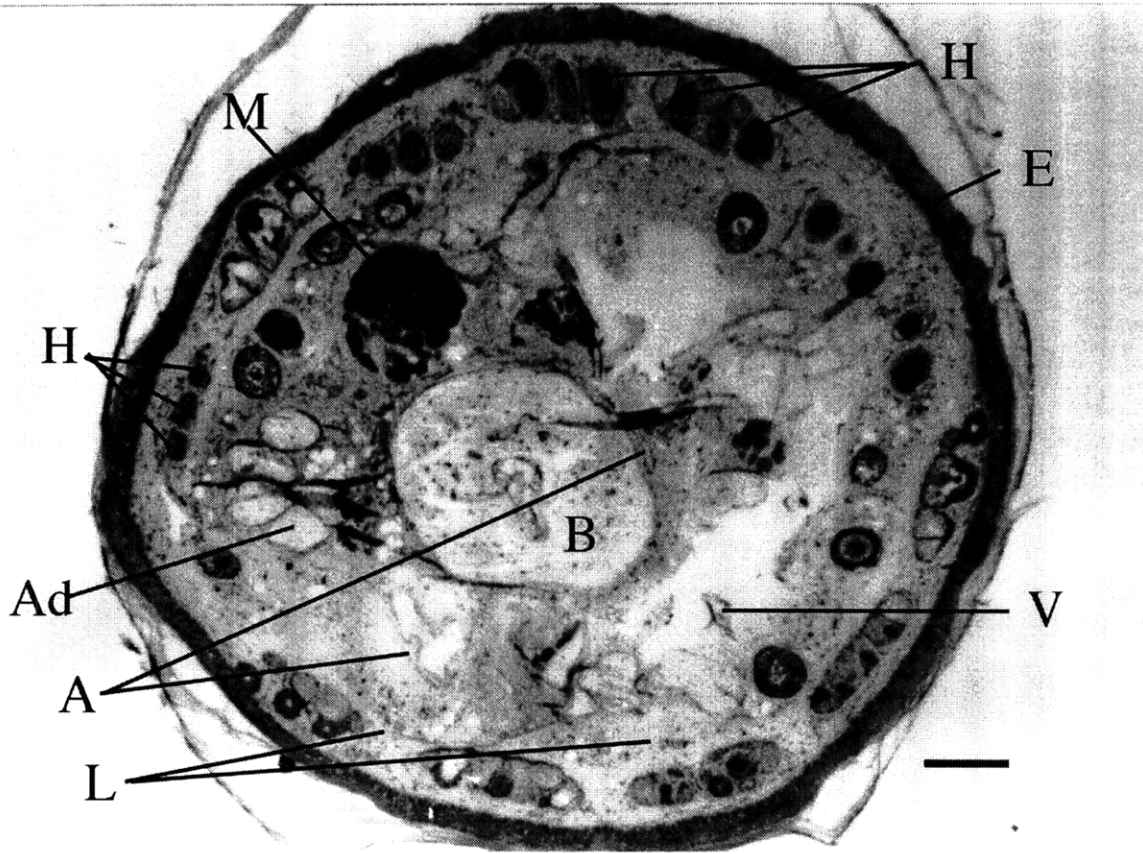


Figure 3-2 Cross section of a nude mouse tail used in these studies, approx. 10 mm from the tip, stained with Toluidine Blue. Scale bar: 100 microns. B = bone, V = venule, L = lymphatic capillary, A = arteriole, Ad = adipose tissue, H = hair follicle, M = skeletal muscle bundle, E = epidermis. Courtesy of Mit Endo.

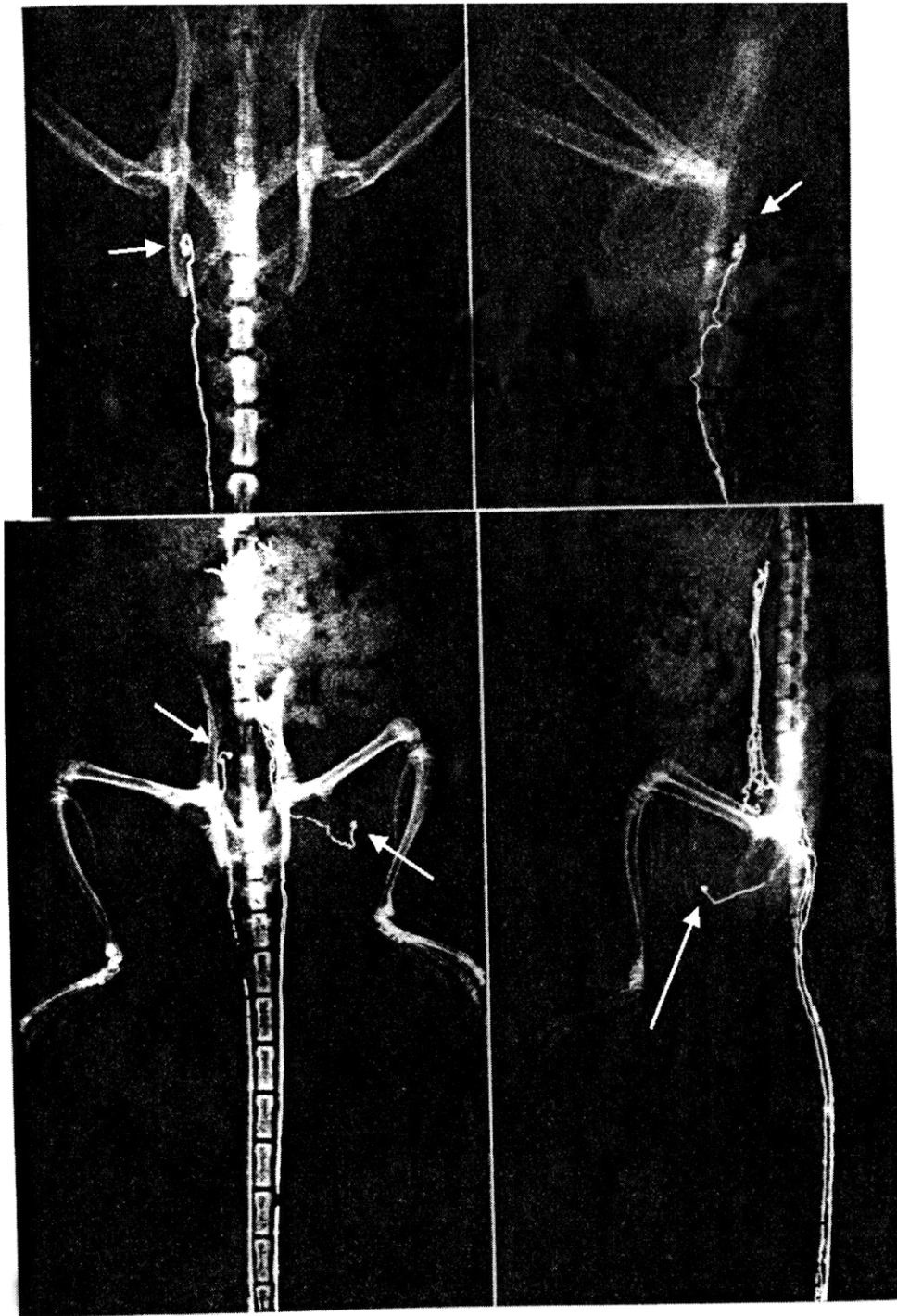


Figure 3-3. Roentgen-photograph of the lymphatic vessels of the rat tail. Because of the low resolution of this technique, only the deeper vessels and draining lymph nodes can be seen. Arrows indicate the ischial lymph nodes. Taken from *Lymphatic pathways from the tail in rats and mice* (Engeset and Tjøtta, 1960).

3.2 Experimental setup

3.2.1 Animals

All studies were carried out in female nude mice that weighed between 20-30 g. Nude mice were used because their qualities of hairlessness and non-scaly skin were ideally suited for *in vivo* fluorescence microscopy. All protocols were approved by the Subcommittee on Research Animal Care of the Massachusetts General Hospital (protocols #93-4147 and #96-4140). Anesthesia was s.c. injection of ketamine hydrochloride at 0.01 mg/g body weight (Ketalar, Parke-Davis, Morris Plains, NY) and xylazine at 0.001 mg/g (Rompun, Haver Mobay Corporation, Shawnee, KS). Before any procedure, the tail was gently washed with soap and water to remove particulates that might interfere with fluorescence measurements and then wiped with an ethanol-soaked gauze pad. The mouse was placed on a small plate (12x5") in the supine position and its tail immobilized from underneath with double-stick tape to avoid imposing pressure on the skin. This plate was placed above a heating pad (Model HP20, Pollenex, Chicago, IL). A rectal probe (Digi-sense, Model 8528-10, Cole Parmer, Chicago, IL) was used to monitor body temperature, which was maintained between 36 and 38 °C throughout all experiments.

3.2.2 Step increase in IFP

Fluorescent dye was administered to the mouse tail at constant pressure using the following scheme, illustrated in Figure 3-4. A calibrated 3-foot long (3/4" diameter) glass cylinder was connected to two feet of flexible tubing, which in turn was connected to PE-20 tubing (i.d. = 0.38 mm, Intramedics, Parsippany, NJ) with a 3-way stopcock (Baxter, Irving, CA). To the open end of this stopcock was attached a 60 ml syringe (Becton-Dickinson, Franklin Lakes, NJ) which facilitated pressure adjustments and tube filling. The narrow tubing ended with a 26 G 1/2" needle (Becton-Dickinson) for inserting into the tip of the mouse tail with the stopcock closed. At the beginning of any experiment, the stopcock was opened and a constant pressure injection thus administered at the tip of the needle.

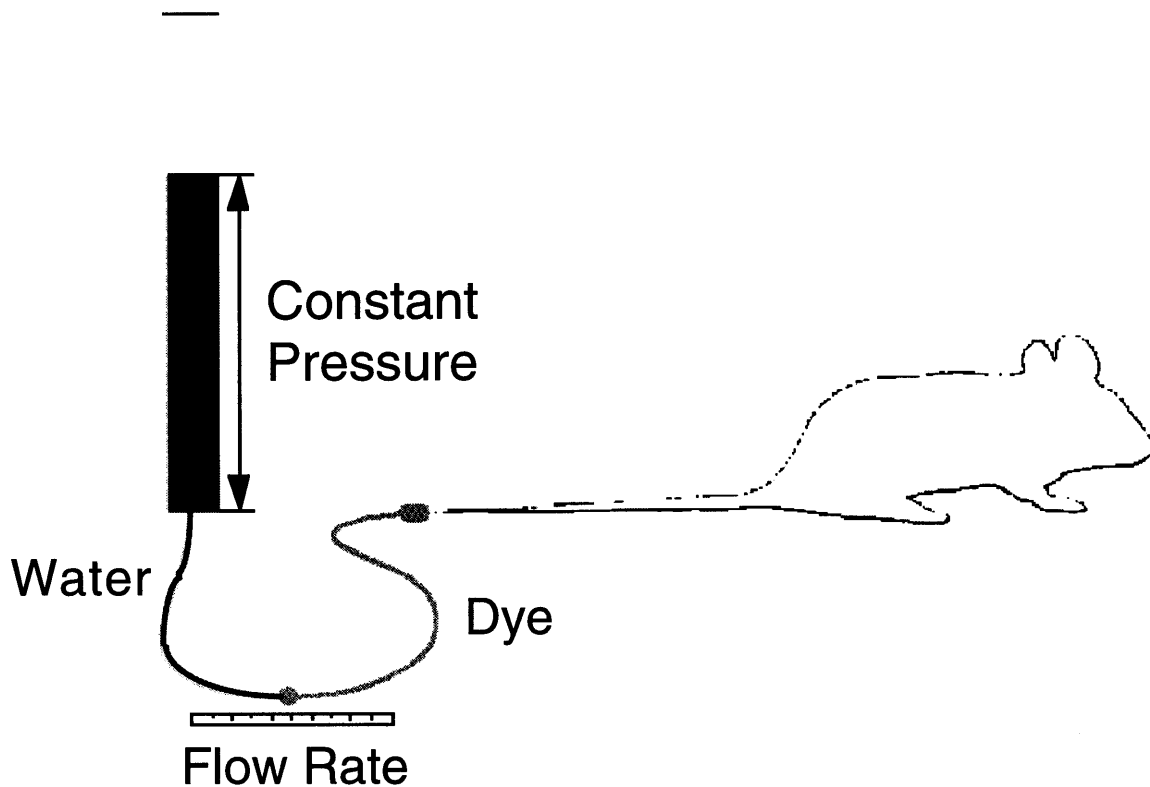


Figure 3-4. Experimental setup for a step-wise, constant pressure infusion into the mouse tail skin.

The glass cylinder was filled with water to the desired pressure (10 to 60 cm water) and the tubing filled with the dye solution from the needle. Except for the experiments described in Chapter 5, and unless otherwise stated, the dye was a 1% (w/v) solution of a fluorescently tagged molecule or particle in 0.9% saline (Abbott Labs, North Chicago, IL). These included dextran labeled with fluorescein isothiocyanate (FITC-Dx) of molecular weight 2M, 400K, 70K, 40K, and 4K; dextran labeled with rhodamine-B isothiocyanate (RITC-Dx) of molecular weights 4K and 73K (Sigma), FITC-labeled anionic dextran 4K (Molecular Probes, Eugene, OR), FITC-BSA (Sigma), and fluorescent microspheres (Molecular Probes) with various diameters ranging from 0.01-1.0 μm . Each appropriate molecule or particle is specified in individual experimental descriptions in later chapters. A

small bubble, far upstream from the needle, permitted the injected volume to be monitored over time (see Section 3.4).

For all experiments, the infusion needle was inserted intradermally (or subcutaneously, since we did not make a distinction between these two tissue types at the tail tip - see Figure 3-9), in a proximal direction parallel to the tail axis, approximately 2 mm into the tip of the tail. At the beginning of an experiment ($t=0$), the stopcock was opened, creating a step change in pressure at the tip from physiological baseline IFP (normally around 9 mm Hg) to the reservoir pressure and thereby injecting the fluorescent solution into the tail. The total length of any experiment varied from 1 to 3 hours. The rate of fluid introduced ranged from 0 to 0.2 $\mu\text{l}/\text{min}$ into approximately 20 to 30 mm^3 of tissue in normal mice, or up to approximately 10 $\mu\text{l}/\text{g}/\text{min}$. This flow rate was an order of magnitude larger in edematous tails, which is addressed in Chapter 7. In all cases, the tail circumference or diameter at the injection site remained constant throughout the experiment as measured by a suture thread or caliper.

3.3 Intensity measurements

Fluorescent images of the tail skin interstitium and lymphatics were visualized with an epifluorescence microscope (Zeiss, Germany). A 100-Watt mercury lamp (Osram, Germany), using a stabilized power supply (Oriol, Stratford, CT), passes first through a heat filter (Zeiss Califlex) before illuminating the mouse tail. Images were collected with a CCD video camera (Hamamatsu Photonics model XC-77, Hamamatsu, Japan) processed through an image processing board. In all studies with one fluorescent probe, a fluorescein label was used and a fluorescein (485 nm) excitation filter was used (Zeiss). For the particle size study of Chapter 4 and the experiments in Chapter 6, two fluorescence channels (Omega Optical, Brattleboro, VT) were used. The first had a fluorescein excitation filter, a 505 nm dichroic mirror, and a 535 nm bandpass emission filter to measure fluorescence from the fluorescein-labeled molecules or green fluorescent microspheres. The second had a 540 nm excitation filter, a 565 nm dichroic mirror, and a 590 nm emission filter to measure fluorescence from the rhodamine-labeled molecules or red microspheres. With these two filter sets, no signal overlap was detected between the two fluorophores.

Flow was categorized in two regions of the tail. The injection site refers to the characteristic length of the injection; that is, where IFP decayed from the injection pressure to near the baseline pressure (a few millimeters in most cases). This was also where most of the interstitial fluorescence was seen, assuming sufficient time for the injection region to

become saturated with the injectate. Within this region, gradients in intensity were recorded for the interstitial transport studies in Chapters 6-7, and IFP was measured in Chapter 5. Downstream from the injection site, the lymphatic capillaries were visible as shown in Figure 3-1. This is referred to as the downstream region and it is the focus of Chapter 4.

To provide markers for viewing different sections of the tail by intravital microscopy, short pieces of suture were placed loosely across the tail at various distances from where the needle tip would be positioned. For the RTD experiments of Chapter 4, where the downstream region was of interest, these sutures were placed 9, 15, 21, and 27 mm from the needle tip. For the transport studies of Chapters 6-7, where interstitial transport was measured in the injection region, two sutures were placed 4 and 10 mm from the needle tip.

The first data point was taken just before beginning the infusion for a background intensity. At each time point, the first window was illuminated and an image acquired either into the image processing board for on-line analysis (Chapters 4 and 7) or saved directly as pixel data for later analysis (Chapter 6). Different cameras, image processing boards and software were used for different studies. A Hamamatsu charge-coupled device (CCD) camera (Hamamatsu, Japan) was used for all image acquisition except the studies described in Chapter 6. For these macromolecular transport studies, greater resolution was desired and so a high-performance camera system (SenSys, Photometrics, Tuscon, AZ) with a CCD chip (Kodak KAF0400), was used to acquire images over longer periods of time (which integrated the images and improved signal-to-noise ratio). Images were analyzed either on-line or off-line. For the RTD studies of Chapter 4, a DT-Iris processing board was used (Data Translation, Marlboro, MA) with a PC interface (IBM) to acquire intensity histograms and extract average values at each timepoint. For the studies in Chapter 6, however, each image was acquired as one file and then analyzed later by NIH Image software (NIH, Bethesda, MD). Time points were taken every 5-10 minutes. More details will be given in each section.

From the intensity histograms of each subregion, mean intensities were recorded so that each subregion then had its own intensity - time curve. The intensity was normalized as

$$\theta = \frac{I - I_{\min}}{I_{\max} - I_{\min}} \quad (3.1)$$

where I is the intensity, I_{\min} is the initial background intensity, and I_{\max} is the steady-state intensity. This normalized intensity was assumed to be equivalent to the normalized concentration profile in the tissue, although it was not possible to calibrate tissue

concentration with intensity. The intensities of all injected solutions were small enough to yield linear concentration-intensity relationships in flat glass capillary tubes (1 mm depth) for concentrations of the injectate, and intensity within the tissue was always less than that of the injectate (as measured in the 1 mm flat capillary tube).

3.4 Flow measurements

To measure the infusion flow rate, a bubble is introduced into the tubing and its position monitored. Calibrations were made using a syringe pump (Harvard Apparatus Model 55-2226, South Natick, MA) in a range of 0.05 to 5.0 $\mu\text{l}/\text{min}$ and are shown in Figure 3-5. Using only saline in the line, inaccuracies in this flow meter were revealed; bubble velocity often lagged behind the imposed velocity in the tubing. Therefore, to maintain surface tension and prevent bubble slippage so that it moved reliably with the fluid velocity, a solution containing 4% (w/v) bovine serum albumin (Sigma) - with 0.5% Evans Blue (Sigma) to aid in visualization - was added to the system in the following way. First, the blue albumin solution was drawn into the PE-20 tubing. Then a small bubble, approximately 1 mm long, was introduced, followed by approximately 1 ml albumin solution. Finally, the fluorescent solution was drawn to 2-3 times the required length; in this way the mixing that occurred at the albumin-dextran interface would not affect the infusate.

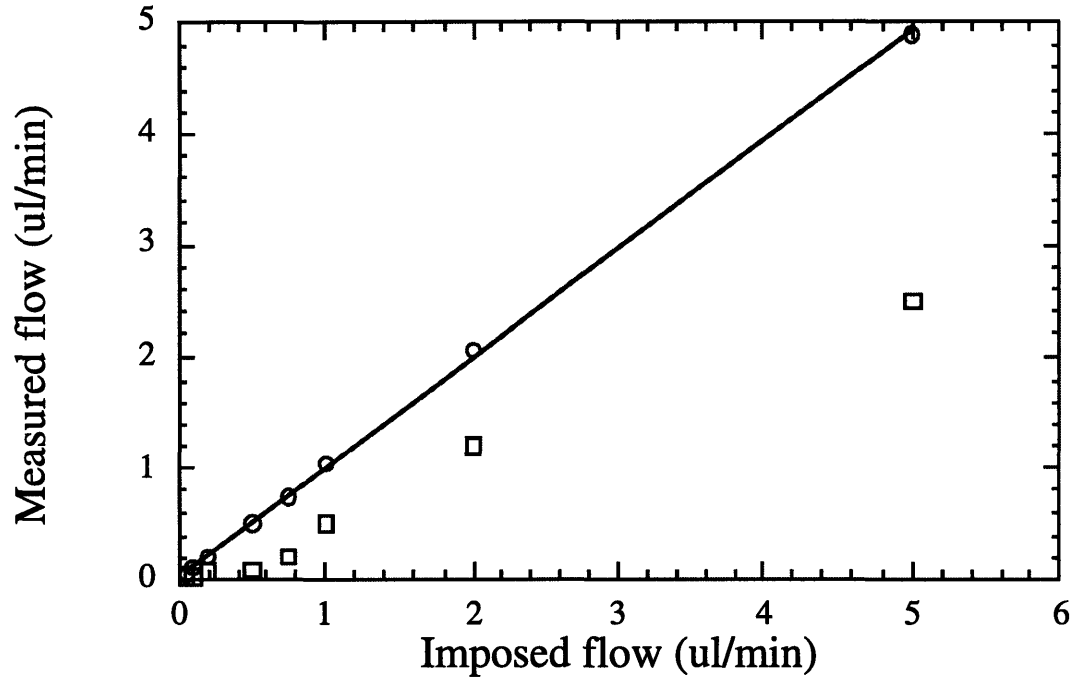


Figure 3-5. Imposed fluid velocity vs. measured bubble velocity in the bubble flow meter. The open squares show the original system (saline-(bubble)-FITC Dx 2M) while the circles and linear fit show the modified system with increased surface tension (4% albumin-(bubble)-albumin-FITC Dx 2M).

3.5 Pressure measurements

Two techniques for measuring interstitial fluid pressure (IFP) are described below. The wick-in-needle method allows IFP to be estimated within 1-2 mm Hg but without optimal spatial resolution. The micropipette or servo-null method gives much better spatial resolution and a more precise measurement, but is technically very difficult and therefore not suitable for routine pressure monitoring. Micropipettes were therefore used to record transient and spatial pressure changes in the tip of the tail following an intradermal infusion. This is explored in Chapter 5, where such precision is necessary to support a theoretical model of tissue fluid balance. The wick-in-needle is utilized in Chapter 7 for daily measurements to detect gross changes in IFP, which were uniform spatially throughout the tail, in experimentally created lymphedema.

3.5.1 Wick-in-needle

In this method, a wick-in-needle was prepared with a 26-gauge needle and four nylon 6-0 sutures (Ethicon, Somerville, NJ). A small hole (approximately 1 mm diameter) was created on the side of the needle, as depicted in Figure 3-6, using a small cylindrical file. Pressure equilibrates at the hole made near the tip of the needle rather than the needle opening itself to avoid artifacts due to needle clogging during insertion (Wiig *et al* 1986). The needle was attached to PE-20 tubing filled with saline and connected to a pressure transducer (Spectramed Model P23XL, Oxnard, CA). MacLab hardware and software (ADInstruments, Australia) were used to output the readings from the pressure transducer at a rate of 100 Hz. Body temperature of the anesthetized mouse was maintained with a thermal pad (Shor-line #712, Kansas City, MO).



Figure 3-6. Wick-in-needle setup to measure IFP.

The wick-in-needle was inserted intradermally, nearly parallel to the tail, until the side hole was completely immersed in the tissue. When the pressure reading stabilized, fluid communication between the transducer and the interstitium was verified in the following way. First, the tubing is squeezed slightly so that a minimal amount of fluid was pushed into the tissue. If fluid communication is good, this causes a rapid increase in pressure followed by an exponential decay back to the original pressure. Then the tubing is released, instantly creating a drop in pressure which again returns exponentially to the true pressure. Failure to return to the original pressure indicates poor fluid communication and an unusable measurement; in this case the needle would be withdrawn, wicks changed, and reinserted into another nearby location. Typical pressure readings from both good and bad fluid communication tests are given below in Figure 3-7.

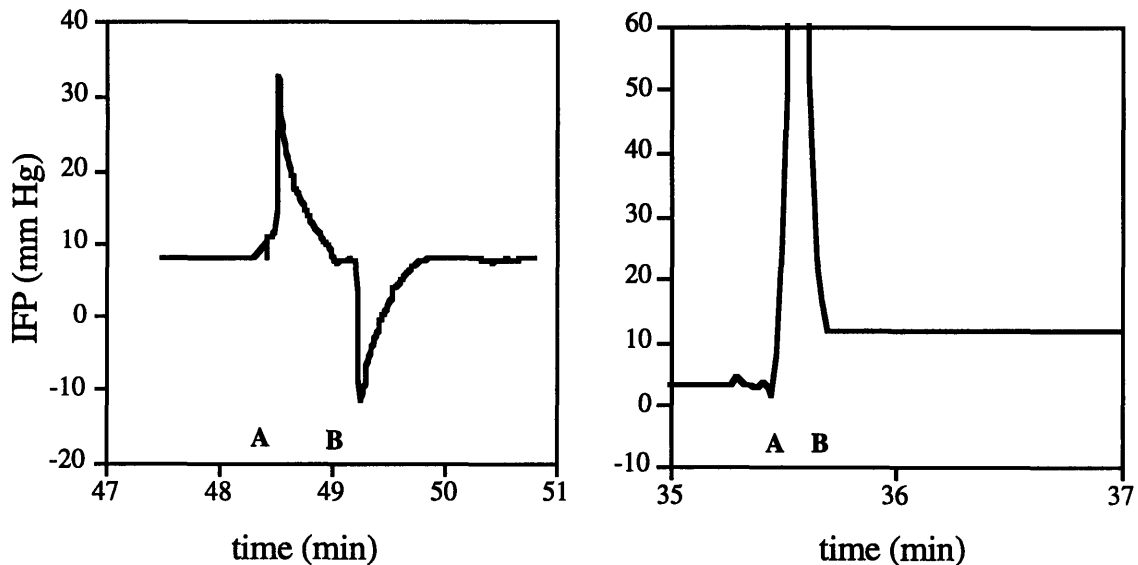


Figure 3-7. Pressure recordings following the depression (A) and release (B) of the catheter tubing to test fluid communication in the wick-and-needle setup in normal mouse tail skin. *Left:* Good fluid communication is seen as the pressure returns to its original position after both depression and release of the tubing. *Right:* When the tubing is depressed, the recorded pressure changes as a step (in this case, it increased to over 300 mm Hg) and returns to an elevated pressure when released, indicating poor fluid communication.

3.5.2 Micropipette

For more precise measurements of IFP, the mouse was placed on a thermal pad under a stereo microscope (model SMZ-U, Nikon, Japan). A glass micropipette of approximately 3-5 μm diameter, connected to a servo-nulling pressure system (IPM model 5D, San Diego, CA) described previously (Boucher and Jain 1992), was introduced into the skin approximately 2-3 mm from the needle tip and 300-400 microns deep. Once fluid communication was achieved (in an analogous manner to that of the wick-in-needle) and an initial baseline pressure recorded, the stopcock was opened to begin the infusion at a pressure of 50 cm water. IFP was continuously recorded in the micropipette until a steady state was achieved (i.e. pressure was constant within 2 mm Hg for at least 5 minutes), resulting in a transient pressure curve. At this time the pipette was withdrawn and placed approximately 1 mm further downstream from the infusion site for measurement of steady-state pressure, and so on until at least 6 steady-state pressure values were recorded. The relative position of the glass micropipette was accurately recorded using a micromanipulator (IPM). Therefore, for each experiment both transient as well as steady-state spatial pressure profiles were recorded.

3.6 Tissue area determination

The cross-sectional area of the tail, near the tip, was estimated histologically. Sections from three mice were fixed, cut, and stained with 0.1% Toluidine Blue (Sigma). A representative section was shown earlier in Figure 3-3. Each photograph was digitally scanned and processed using NIH Image (NIH, Bethesda, MD). The total area was measured along with that of the epidermis, bone, muscle bundles, and any blood vessels. The dermal / subcutaneous fraction of total tissue area was thus calculated by subtracting the other constituents from the total area. Therefore, to grossly estimate the cross-sectional area for fluid flow in each experiment, the tail diameter was measured and multiplied by this fraction.

The theoretical frameworks presented in the succeeding chapters relies on the assumption that all fluid flow following an interstitial injection occurs in the dermal and subcutaneous tissues. To support this assumption, tail cross-sections were stained for collagen using a Masson stain and hyaluronic acid using a Periodic Acid-Schiff stain (Bancroft and Stevens, 1982). These matrix proteins are primarily responsible for the transport properties of the tissue, and in particular, glycosaminoglycan density (of which hyaluronic acid is the predominant constituent) has been most closely correlated (inversely)

with hydraulic conductivity (Aukland and Reed 1993, Levick 1987, Grodzinsky 1983). As shown in Figures 3-8 (a) and (b), the subcutis contains less collagen and hyaluronic acid than the dermis, suggesting a higher hydraulic conductivity and lower elasticity in this region. We therefore assume that most of the fluid flow following an interstitial injection occurs in the subcutaneous space. However, there is no clear boundary between these two tissue types, and they cannot be distinguished experimentally. Therefore the dermis and subcutis will be treated as one composite tissue throughout this thesis, and transport parameters will be considered as bulk-averaged parameters for mouse tail skin in a general sense.

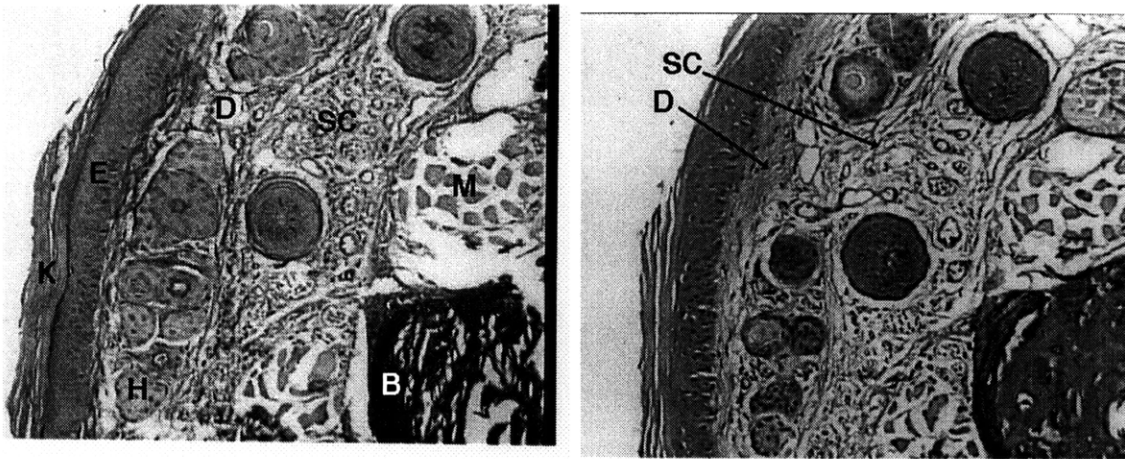


Figure 3-8 Matrix protein density in the mouse tail. B = bone, H = hair follicle, K = keratin, E = epidermis, D = dermis, SC = subcutis, M = muscle. *Left (a)*: Masson stain for collagen. Other than bone, the dermis shows a higher collagen density than the subcutaneous space. *(b)* Periodic Acid-Schiff stain for hyaluronic acid, which again shows a higher density in the dermal layer, particularly close to the epidermis.

3.7 *In vitro* mechanical tests

For comparison with the *in situ* data of Chapter 5, *in vitro* stress-strain tests were performed by confined compression using a Dynastat apparatus as previously described (Frank and Grodzinsky, 1987) to estimate the elasticity of mouse tail skin under compression. Tail skin was excised immediately after sacrifice by making two circumferential incisions approximately 1 cm apart, joining them with a third axial incision, and carefully ‘peeling’ the skin from the bone-tendon core using a hemostat and scalpel. From this, a 3-mm disk was bored and placed in a confined compression chamber. Placement was specifically epidermal-side down, with the assumption that the epidermis has a higher elastic modulus than the dermis and subcutis so that the epidermal strain was zero and stress (measured from the top) resulted from the relaxation of the dermal and subcutaneous tissues only. Displacements of 25 μm were imposed and the resulting stress measured for a total of 6 cycles each.

3.8 Model applications

In the following chapters, various aspects of the mouse model will be explored and modified. First, flow within the lymphatic system is studied in Chapter 4, where fluid pathlines and streamlines as well as net average flow are observed with different techniques. Chapter 5 investigates the mechanical aspects of interstitial-lymphatic fluid balance with a theoretical model and interstitial pressure measurements. Macromolecular transport is explored in Chapter 6, where the tail is considered theoretically similar to a chromatography column in order to estimate key transport parameters from observed concentration profiles. Finally, Chapter 7 highlights other applications which are used to elucidate the biology and pathophysiology of interstitial fluid balance and lymphatic function, as well as assess a potential surgical procedure to relieve edema. The experimental details of those studies will be described in each section of Chapter 7.

Chapter 4

Measurements of Flow Velocity¹

4.1 Introduction

As seen in Figure 3-2, the lymphatic network of the mouse tail can be stained progressively following an intradermal injection of fluorescently labeled tracer into the tail tip. This chapter describes the initial development and characterization of this phenomena and establishes the mouse tail skin model for quantitative investigations of interstitial-lymphatic transport phenomena. Specifically, flow within the lymphatics was examined both macroscopically and microscopically, and uptake was evaluated in a semi-quantitative manner. Because of its regularity, apparent unidimensionality, and minimally invasive nature, this model presented excellent potential for a variety of other applications, and is continually modified and refined in succeeding chapters.

Consider the images in Figure 3-4. The staining of the lymphatic network is dispersive and approximately one-dimensional, similar to flow phenomena in packed beds. For these reasons, residence time distribution theory was utilized to evaluate macroscale velocity and uptake. This analysis was then used to evaluate the roles of molecular weight and injection pressure in lymphatic transport. In addition, a microscopic approach utilized the technique of fluorescence recovery after photobleaching (FRAP) to establish local instantaneous velocity and observe, on short time scales, streamlines of fluid movement in individual vessels. Finally, 1- μm latex microspheres were used to visualize local flow patterns (pathlines). Thus the process of lymph formation following an interstitial injection was characterized on both macroscopic and microscopic scales so that local changes in flow behavior could be correlated with overall net effects and a better understanding of transport behavior within the lymphatic capillaries could be attained. This work established the

¹ This work is published in the companion papers Swartz *et al* 1996 and Berk *et al* 1996.

mouse tail skin model as a quantitative tool for studying initial lymphatic function and interstitial-lymphatic phenomena. It was done in collaboration with Dr. David Berk.

4.2 Theory

4.2.1 Macroscale (average) velocity

The lymphatic filling patterns of Figure 3-4 suggests that the velocity of lymph propulsion can be estimated by tracking the “moving front” of fluorescent tracer. However, the front is not clearly defined due to dispersive effects as molecules enter the lymphatics and travel through multiple pathways of the network. A plot of intensity vs. time for a given small section of the network would result in an S-shaped curve as the intensity rises from a minimum (background) to its asymptotic maximum; a typical plot is shown in Figure 4-1. Both the extent of mixing within the network and the time required to establish a steady state uptake rate of fluorescently tagged particles will determine the spread of this curve.

The residence time distribution (RTD) theory of Danckwerts (1953) can be used to analyze these transient intensity profiles and macroscopically evaluate the transient uptake phase as well as the dispersion and mixing that the dye molecules experience as they travel through the lymphatic network. The average time it takes a particle to reach a certain distance from the point it was injected is referred to as the mean residence time (MRT). If the dye were injected directly into the lymphatic vasculature, the slope of MRT vs. distance would indicate the average velocity in the axial direction. If the dye were instead injected into the interstitium, the MRT would include both the average time for a particle to enter the lymphatics from the interstitium (i.e., uptake) in addition to the time to travel through the network. Therefore, by examining the relationship between MRT and distance, the behavior of the average axial velocity in the superficial lymphatics as a function of distance can be observed, and a relative measure of uptake time can be obtained by extrapolating the curve back to the injection site. This site is actually a region whose boundaries may change throughout the experiment. Because it never extended more than 1 cm from the tip of the tail using the experimental conditions described below, this distance was chosen to encompass and define the injection site. The MRT at this intercept was then taken as a semi-quantitative measure of the initial uptake rate. Its rigorous definition will be explored in Chapter 5.

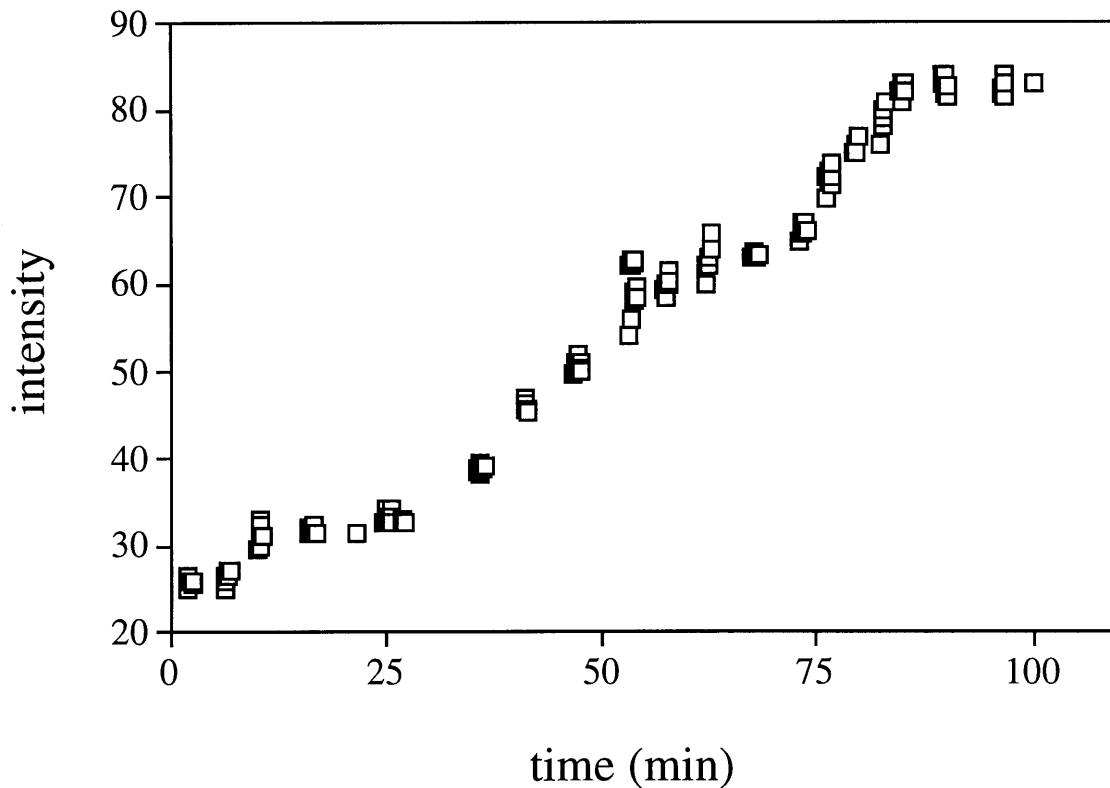


Figure 4-1. Staining of the lymphatic network following intradermal injection of FITC-Dextran 2M as measured by fluorescence intensity approximately 1 cm downstream from injection.

The fluorescence measurements obtained in this way arise primarily from the superficial capillary network; thus, the deeper unseen layer of collecting lymphatics is a matter of concern. If the two parallel networks are completely uncoupled (except at injection site), then the RTD analysis reveals nothing about the deeper lymphatics. However, if a significant amount of flow occurs at the regular connections, it is likely that the superficial network mirrors the same time course of lymph staining that occurs in the deeper level.

If θ is the normalized concentration, assumed to be equivalent to the normalized intensity (see Section 3.4), the MRT is given by (Danckwerts):

$$MRT = \frac{\int_0^{\infty} \theta t dt}{\int_0^{\infty} \theta dt} \quad (4.1)$$

This is equivalent to the area above the normalized concentration vs. time curve:

$$MRT = \int_0^{\infty} \frac{d\theta}{dt} t dt = \int_0^{\infty} (1 - \theta) dt \cong \sum_{i=1}^n (1 - \theta) \Delta t \quad (4.2)$$

The MRT was calculated in this way for each distance.

4.2.2 Microscale (local) velocity

Lymph flow velocities in individual capillaries were measured by the method of fluorescence recovery or redistribution after photobleaching (FRAP). A region of fluorescent lymph was photobleached by brief exposure to focused laser illumination, and the movement of the resulting darkened photobleached material was recorded in a series of images immediately following. The monitoring of the photobleached spot (complicated by light scattering in tissue) and determination of its center is previously described (Berk et al 1996).

4.3 Methods

Forty-four mice were used for these experiments: 10 for the determination of network velocity, 8 for the size-dependence studies, 5 for the FRAP experiments, and 8 for the microsphere injections. The basics of the experimental setup, including animal preparation and intensity and flow measurements, are detailed in Chapter 3.

4.3.1 Macroscopic data acquisition and analysis

For the macroscopic examination of flow phenomena in the superficial lymphatics, a 2.5X objective with a 1.25X eyepiece lens was used, resulting in field dimensions of 3

mm x 2.5 mm. Short pieces of suture were placed loosely across the tail at 1.0, 1.6, 2.2, and 2.8 cm from where the needle tip would be positioned to provide markers for viewing different sections of the tail. Each thin suture could then mark one side of a “window” (3 mm wide) along the tail so that eight consecutive windows could be accurately positioned and analyzed at each timepoint. The first data point was taken just prior to beginning the infusion for a background value. The light source was masked in the filter housing to prevent unnecessary exposure and possible photobleaching. At each timepoint, the mask was removed, illuminating the first segment or window (0.6 cm from the injection site). The image was acquired into an image processing board (DT-IRIS, Data Translation, Marlboro, MA), where the screen was divided into five vertical rectangles (2 mm x 0.6 mm) and intensity histograms were recorded for each. This was repeated for all 8 regions. Thus, at each timepoint, the average intensity was measured in each of 40 consecutive windows along the tail, spanning a length of 2.4 cm. These timepoints were taken every ten minutes until the intensity change was less than 5% from the previous value (typical time for the most proximal window was 3 hours).

From each histogram, the intensities from the brightest 5-15% of the pixels were averaged. This is because the scattered light increases the “background” intensity (regions between vessels) as the network fills with fluorescent material. By averaging only the brighter pixels, intensity changes in the vessels alone can be averaged against an “initial condition” background. Furthermore, because of occasional fluorescent particulate debris, the brightest 5% of pixels were omitted from the average; however, it should be noted that the results were not sensitive to the exact choice of these cutoff fractions.

To further characterize the model, the effects of particle size and injection pressure on both uptake and network velocity were examined in separate studies. One study involved the coinjection of two different dextrans, each with a different fluorescent label - fluorescein- or rhodamine B-isothiocyanate (FITC or RITC) - so that size effects could be directly compared in each mouse. Two groups of four mice were compared: group A was injected with a solution of FITC-Dx 71K and RITC-Dx 73K, and group B with a solution of FITC-Dx 2M and RITC-Dx 73K. Both solutions contained 0.0125 g/ml of each dextran in 0.9% saline. *In vitro* studies estimated the hydrodynamic radius of FITC-Dx 2M to be 18 nm and that of FITC-Dx 71K to be 6 nm, a threefold size difference. These are only gross estimates which were obtained from FRAP measurements of the diffusion coefficient (Berk et al) by assuming a Stokes-Einstein relationship between D and radius².

² The FRAP technique is described below in the next section, where it is used to calculate local convective velocities in single lymphatic vessels. Here it is used to estimate diffusion coefficients in dilute, stagnant

The other study compared the effects of injection pressure on lymphatic uptake and lymph propulsion velocity. Two different injection pressures were compared in five mice each: 10 or 40 cm water (7.4 or 29.4 mm Hg). FITC-Dx 2M was used for this set of experiments.

4.3.2 Microscopic data acquisition and analysis

To observe flow phenomena in individual capillaries, a 10X, 0.35 NA objective with a 1.25X eyepiece was used. Two series of experiments were performed: visualization of flow patterns with fluorescent microspheres and measurement of velocity using FRAP.

For direct visualization of flow in individual capillaries, microspheres of 1 μ m diameter were injected using relatively high pressure (approximately 5 ml in one second) using a 25- μ l microsyringe (Hamilton, Reno, NV). Because particles of this size cannot freely move through the interstitial space, only a sudden and large local edema resulted in uptake, so such injection conditions were necessary to observe spheres in the lymphatic capillaries. Their movements were recorded on videotape 30 minutes after injection and their oscillation frequency was counted by real-time observation. One mouse in this study was tracheotomized and artificially ventilated³ (Harvard Apparatus Rodent Ventilator, model 683, S. Natick, MA) at either 120 or 140 breaths per minute at a tidal volume of 0.15 ml/breath (Kleinman & Radford, 1964, Roscoe 1966) to examine the effects of respiration on lymph flow.

The injection procedure for the FRAP experiments was identical to the less disruptive method used in the RTD experiments described above (FITC-Dx 2M, injected at a pressure of 40 cm water). FRAP measurements were initiated after sufficient fluorescent

fluorescent solutions in flat glass capillary tubes as described by Berk *et al* (1993). Then, the hydrodynamic radius is estimated by the Stokes-Einstein relation; i.e. $r = \frac{kT}{6\pi\mu D}$.

³ The mouse tracheotomy was based on a similar procedure performed in rabbits (Eckmann *et al*, 1997). First, the throat tissue was dissected to the trachea. A curved hemostat was placed underneath to allow control and manipulation of the trachea, and suture was drawn underneath with the hemostat. A hemispherical cut was made perpendicular to the axis of the trachea using a size-15 scalpel. Using the hemostat, a 3-cm length of sterile PE-20 tubing was inserted approximately 5 mm into the trachea, where it was quickly and tightly tied with the suture. The PE-20 tubing was connected to a Y connector, which in turn was connected via PE-50 tubing to the ventilator (one for inhalation and the other for exhalation). The entire tracheotomy procedure lasted approximately 5 minutes, and the mouse was ventilated immediately upon tracheal insertion of the tubing.

material appeared in the lymphatic capillaries (within 10 minutes). The FRAP apparatus and details of the Fourier analysis of the images are described previously (Berk et al 1996).

The tail was positioned under the objective, and vessels were randomly selected in the region 1 to 3 cm from the injection site. A capillary segment was positioned within the microscope field of view so that its (radial) center fell within the previously determined path of the laser beam. Regions near the intersection of several capillaries were avoided because of anticipated complexities in flow patterns there. Within the 512 x 480 pixel video image, a smaller rectangular region (10% to 25% of the total field) was defined to encompass the capillary segment. An image of this region was digitized and stored, and then the laser shutter was opened for a duration of 0.02 sec. Images of the photobleached spot were then acquired at a rate of 6 images per second for approximately 4 seconds, followed by a rate of one image per second for a total elapsed time of approximately 15 seconds. The distance of the measurement site from the injection site were stored for later analysis. For each mouse, approximately 20 to 30 of these photobleaching sequences were obtained over the course of 90 minutes.

4.4 Results

4.4.1 Macroscopic (network) velocity and the effects of injection pressure

Representative MRT vs. distance plots for two mice, one characteristic data set for each injection pressure, are shown in Figure 4-2. The MRT increased linearly with distance in all cases for distances greater than 1 cm from the injection site, so linear regression was used. The net velocity could not be measured in this way for distances greater than 3 cm from injection because the concentration profiles become too diffuse to define a MRT.

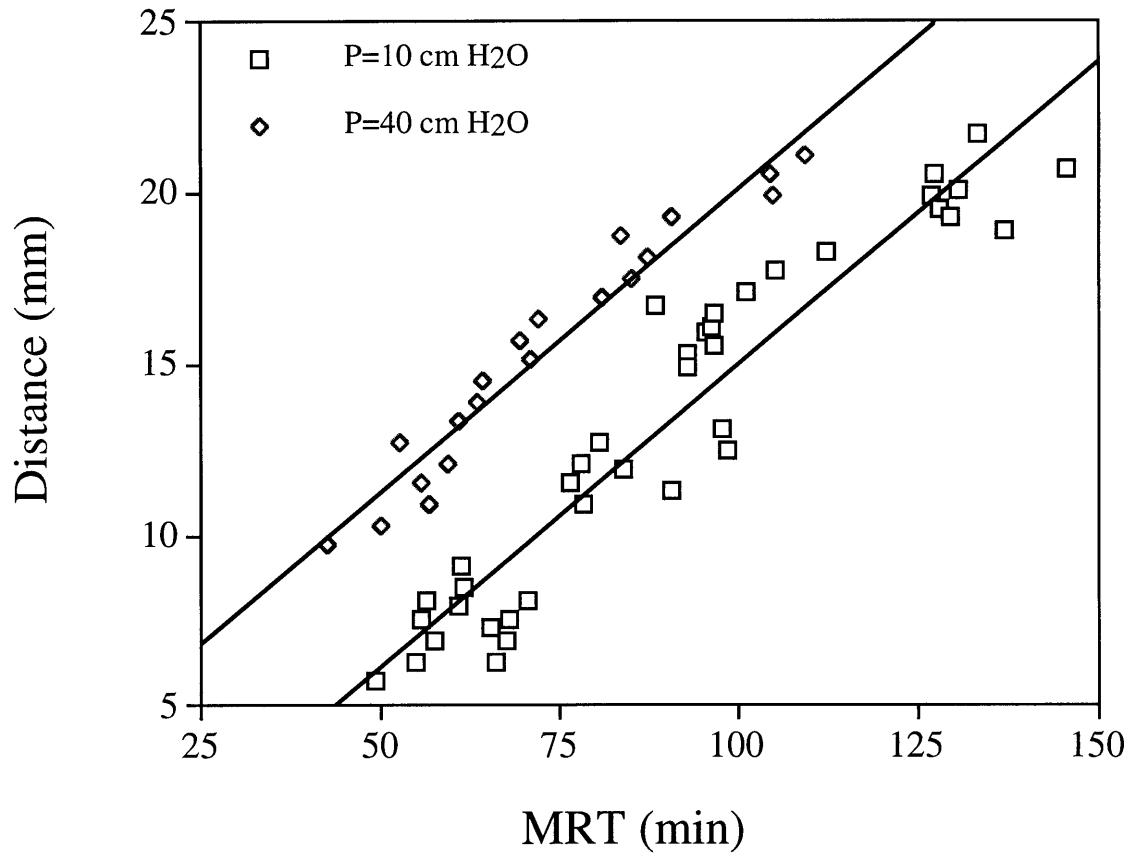


Figure 4-2. Representative MRT vs. distance data for each injection pressure. Here, the velocity (slope) for the low injection pressure ($P=10 \text{ cm H}_2\text{O}$) is $3.18 \mu\text{m/s}$ and intercept (MRT at 1 cm, shown by the dotted line) is 74.3 min ($r^2=0.906$). For the high injection pressure ($P=40 \text{ cm H}_2\text{O}$), the velocity was $2.97 \mu\text{m/s}$ while the intercept was 39.6 min ($r^2=0.944$).

Results comparing the two injection pressures are summarized in Table 4.1. Each value represents the average of five mice. Not only was the slope (velocity) constant in both cases, but there was no significant difference in velocities between the two injection pressure groups (P=0.629 using Student's t-test). However, the relative uptake rates, represented by the intercept (MRT at 1.0 cm), varied greatly between the two groups (P=0.017). In addition, the average injection flow rates were significantly different (P=0.0015): for the lower injection pressure, the mean injection flow rate was 15 ± 4 nl/min, and for the higher injection pressure it was 41 ± 11 nl/min.

	Velocity (microns/s)		MRT (min) @ 1 cm	
	10 cm H ₂ O	40 cm H ₂ O	10 cm H ₂ O	40 cm H ₂ O
minimum	1.36	2.77	66.6	33.7
maximum	6.13	5.27	149.0	52.1
mean	3.34	3.80	90.0	44.1
median	3.18	3.73	74.3	46.4
standard deviation	0.80	1.02	15.14	7.4

Table 4.1. Network velocity analysis data for injection pressures of 10 and 40 cm H₂O (n=5 for each group).

4.4.2 Effects of particle size

To evaluate the effects of particle size, the difference in MRT between the two coinjected particles (RITC-Dx - FITC-Dx) was computed for each subregion. Assuming the particles move with the same average velocity as the fluid, there should be no difference between slopes of MRT vs. distance for each particle, and the differences in MRT would be solely due to differences in uptake. Therefore, these differences at each subregion were averaged for each mouse. The mean difference for group A, which consisted of two dextrans of 71 / 73 kDa each (approx. 6 nm radius), was 1.6 ± 3.0 min. For group B, which used different size dextrans of 73 and 2,000 kDa (6 and 18 nm), it was 2.4 ± 4.7 min. Neither of these were significantly different from zero according to a student's t-test ($P=0.24$ and 0.28 , respectively), nor from each other ($P=0.81$).

4.4.3 Microscale velocity in individual capillaries using FRAP

FRAP measurements were performed in five animals. A total of 130 velocity determinations were made, of which 110 were judged valid based on the agreement between the calculated spot path and the orientation of the lymphatic capillary. Figure 4-3 shows selected images from a typical photobleaching experiment, while Figure 4-4 illustrates the data obtained by spatial Fourier analysis of these images, with the calculated path of the spot superimposed over the outline of the lymphatic vessel.

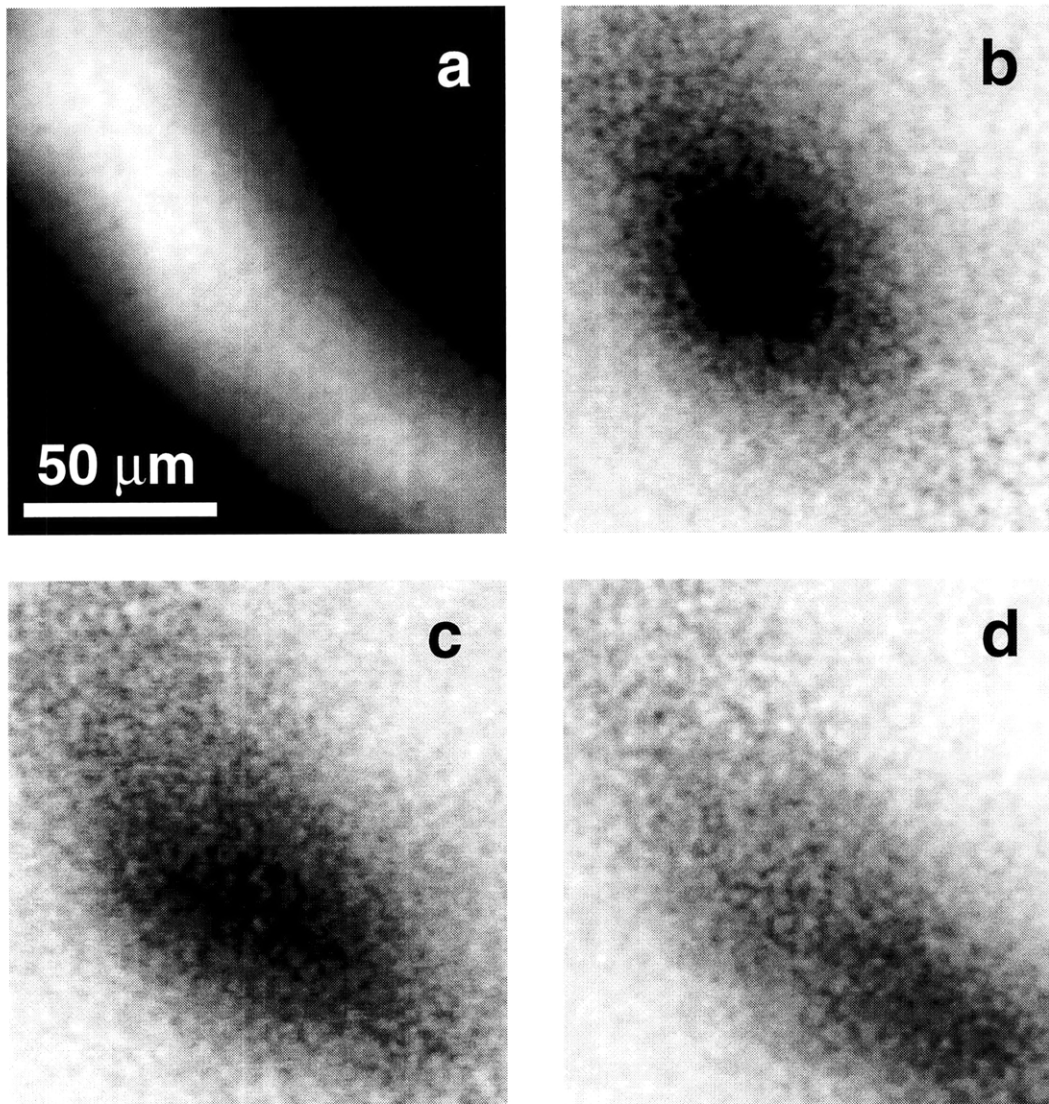


Figure 4-3. The photobleaching and subsequent recovery of fluorescent material in a lymphatic vessel. a) FITC-Dx loaded capillary prior to photobleaching. b) Differential image at $t = 0.2$ s after laser exposure. The photobleached region appears dark. c) Differential image at $t = 4$ s. d) Differential image at $t = 9$ s. In b through d, the spot moves to the bottom right corner of the image while it also dissipates. All figures are the same size scale.

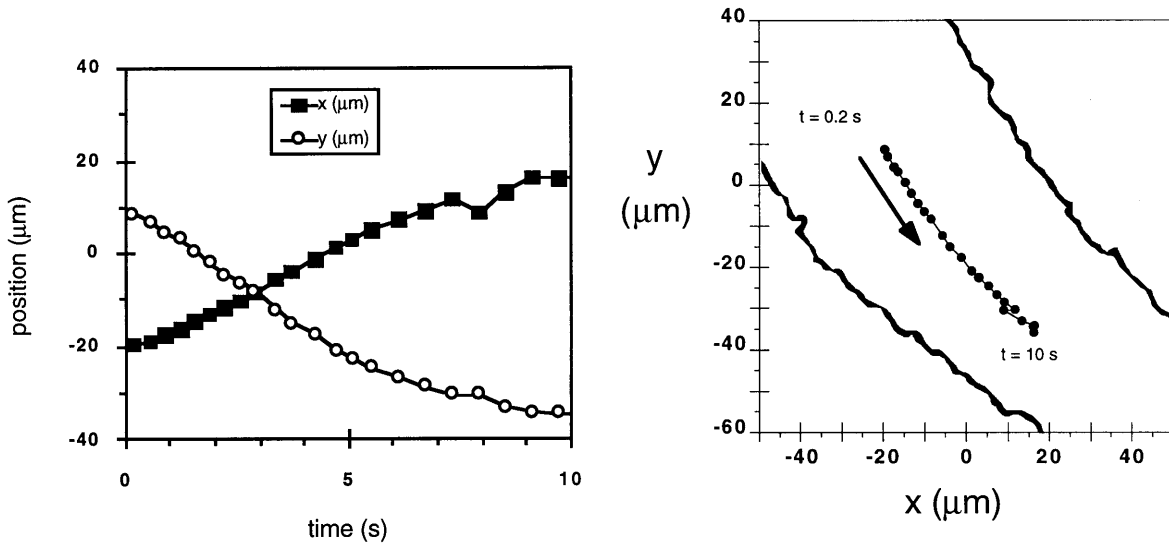


Figure 4-4. Spatial Fourier analysis of FRAP images. *Left* (a): The x and y coordinates of the spot, calculated as described in the text, are plotted versus time to show the velocity. *Right* (b): The path of the spot (symbols) is superimposed over the outlines of the lymphatic vessel. In both figures, the origin refers to the centerpoint of the image.

The use of FRAP allows the fluid velocity in a single capillary to be measured at different timepoints. In this series of experiments, it was difficult to discern a consistent pattern that described the time dependence of velocity in individual capillaries. Figure 4-5 displays the behavior of 2 separate vessels. In one vessel which was perpendicular to the tail axis or direction of net flow, the velocity is as rapid as $8 \mu\text{m/s}$ within the first 20 minutes of injection, falling to zero or slightly negative after one hour. In another vessel, the velocity is consistently around $5 \mu\text{m/s}$, except for a brief peak of $17 \mu\text{m/s}$ one hour after injection was begun.

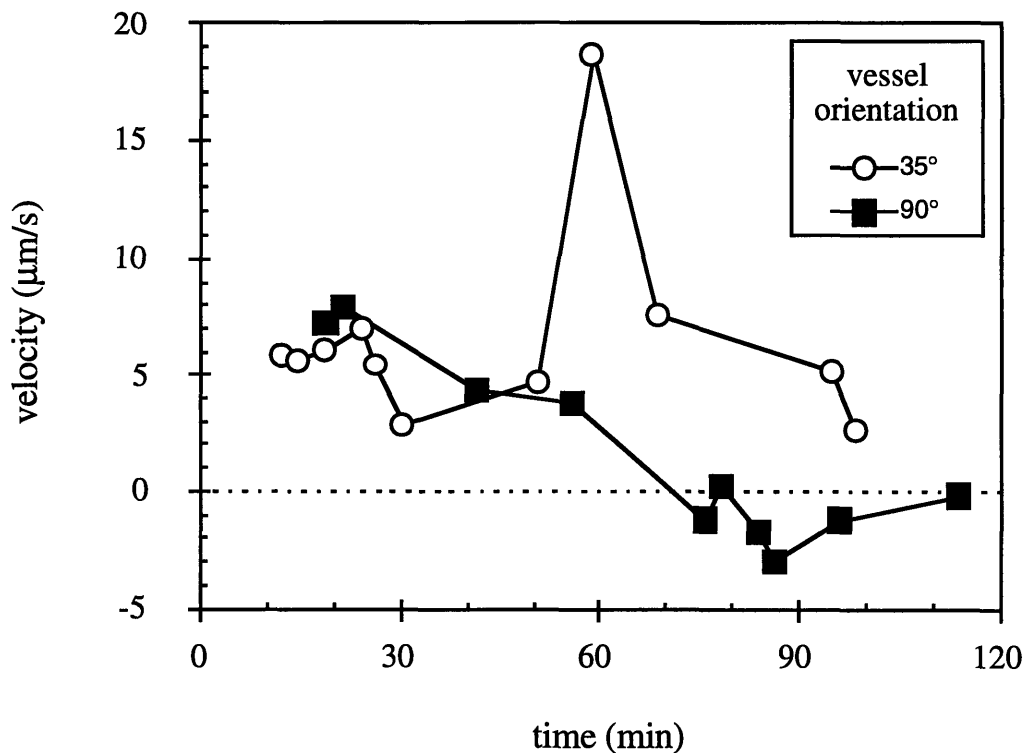


Figure. 4-5. Instantaneous velocity within two individual capillaries as a function of time during constant-pressure dye injection into the tail skin. One vessel was oriented perpendicular to the tail axis and the other formed an acute angle with the tail axis.

A wide range of velocities were observed, from -19.46 to 28.96 $\mu\text{m/sec}$, with a median of 3.43 $\mu\text{m/s}$ and an interquartile range of -0.45 to 7.45 $\mu\text{m/s}$. Figure 4-6A shows a plot of all velocity measurements in three different vessels of one particular mouse as a function of time (from the beginning of the injection). The plot shows that at all times, flow velocity is not uniform but spans a range that includes zero and negative (flow in the distal direction) values. The plot also suggests that the absolute value of velocity is generally greater in the initial phase of the experiment. Compiling all the experiments, an analysis of variance test was used to compare measurements made in each of four half-hour time segments. The decay of velocity magnitude was significant ($p < 0.0001$), but appeared to

reach a plateau in the second hour, as illustrated in Figure 4-6B. A similar analysis of the correlation between velocity and distance from the injection site revealed no obvious dependence.

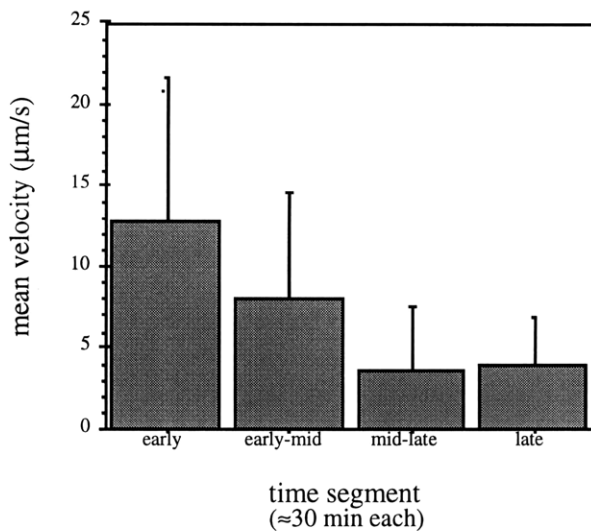
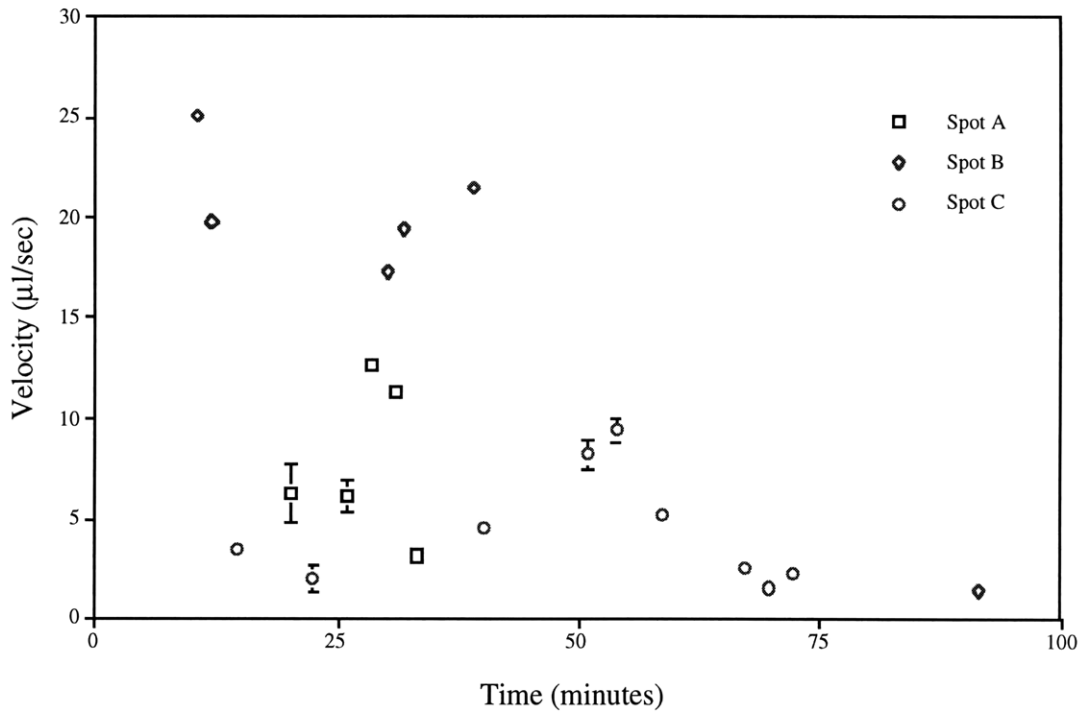


Figure 4.6. Relation between velocity magnitude and time of dye infusion. *Top* (a): Compilation of velocity magnitudes collected in one mouse. Each symbol denotes the measurements from one of three vessels. *Left* (b): Mean and standard deviation of values from all velocity magnitudes collected ($n=111$), grouped into 30 minute time segments. The decay is significant (analysis of variance test, $p<0.0001$) and appears to stabilize in the final hour.

4.4.4 Flow visualization using microspheres

By injecting 1- μm latex spheres, flow patterns could be directly visualized in five of either mice simply by following the motion of individual spheres (Figure 4-7). In all five cases, the spheres were observed to oscillate at an average frequency of 125 per minute. This frequency which correlated closely with respiration rate (115-145 per minute) rather than heart beat (over 200 per minute) or vasomotion (2-10 per minute). Because of this, one mouse was ventilated artificially so that its respiration rate could be controlled and altered. The oscillations of the spheres correlated exactly with a ventilation rate of 120 per minute, and when this frequency was increased to 140 per minute, oscillation frequency also increased to 140 per minute.

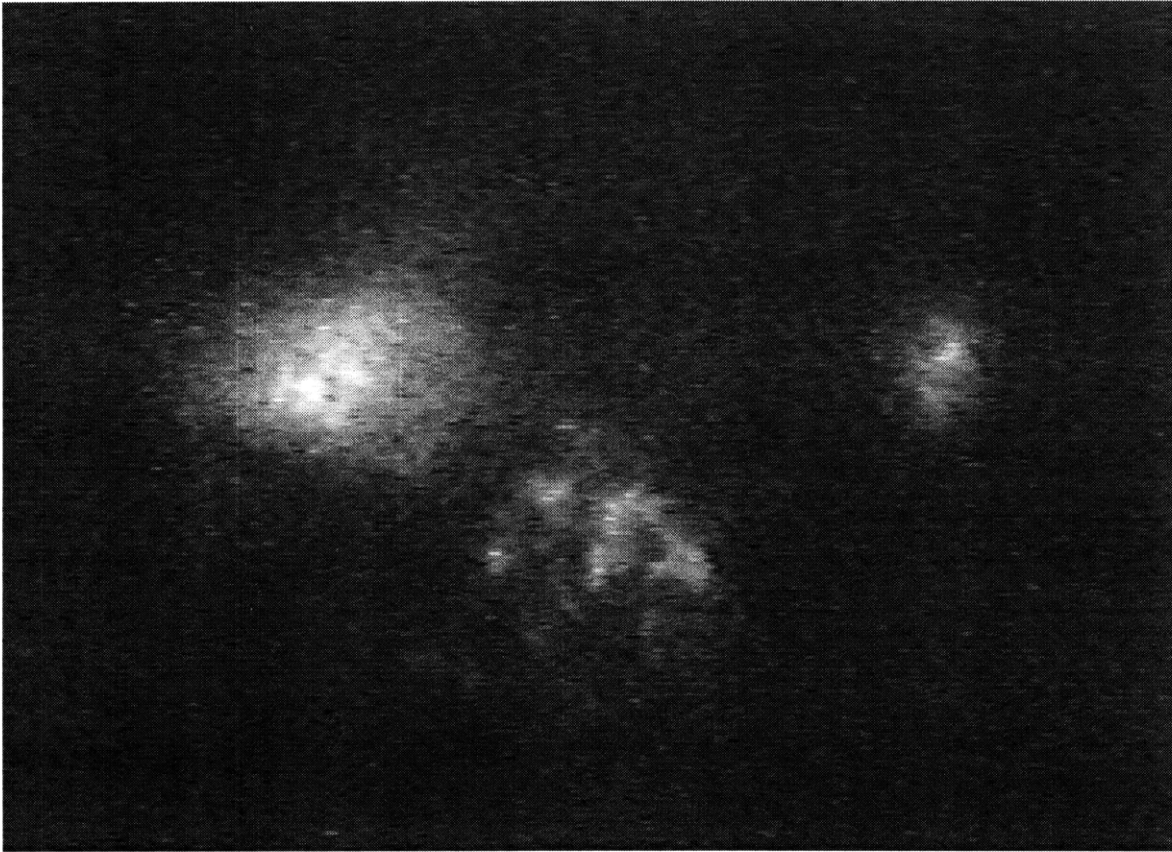


Figure 4-7. Images of fluorescent microspheres in the superficial lymphatic capillaries of the mouse tail skin. Their non-optimal focus is the result of light scattering from a depth of approximately 100-200 μm below the surface. Total width of the image is 375 μm .

4.5 Discussion

Unlike blood vessels, in which net flow velocity can be measured as well as streamlines and pathlines observed simultaneously with the red blood cells, the lymph has no such natural markers for fluid movement. In this chapter, novel fluorescent techniques were developed for examining lymph flow both on macroscopic and microscopic scales. Uptake and net axial flow velocity were characterized using RTD theory by following the dispersion of an injected tracer. Local details of flow in individual capillaries were evaluated using FRAP and microsphere injections. These techniques not only allow new types of investigations into lymphatic physiology, but they are also useful tools for cell trafficking studies. For example, FRAP can be used to estimate shear stresses in lymphatic capillaries and thus evaluate cell adhesion.

RTD theory proved to be accurate and appropriate for a first-order characterization of the net velocity and uptake; by integrating a dispersed intensity curve over time, the average time for a particle to enter the initial lymphatics and travel a given distance within that network can be calculated. Uptake and flow times can be resolved, and a net velocity can be determined by comparing this average time with distance. The underlying assumption that the velocity of a tracer molecule represents the fluid velocity within the lymphatic capillaries (but not within the interstitium) is supported by the fact that a linear relationship exists between MRT and distance. The assumption is further supported by the FRAP studies, which accounted for dispersive effects independent of velocity. This simple analysis permits investigations of the effects of various physiological factors on lymphatic function, and we have shown here examples of particle size and injection pressure.

Pilot studies showed that initial uptake is independent of injection concentration at injection pressures of 10-40 cm H₂O. This was done as an experimental control to ensure that fluid uptake was convection-dominated and that the interstitial concentration imposed by the injection did not affect the uptake rate of fluid in the range of experimental conditions used. Furthermore, the results from the size study indicate that, in such convective uptake, the lymphatic endothelium did not pose a size barrier to the macromolecules in an approximate range of 6-18 nm radius. Since the uptake time also reflects the interstitial transport time, and since such a size difference is unlikely to travel through the interstitium in the same way, the limitations of the technique are exposed. In other words, while the technique is good at quantifying intralymphatic flow phenomena, it shows little sensitivity in distinguishing interstitial transport phenomena such as size partitioning. A more refined approach to interstitial macromolecular transport is addressed in Chapter 6.

The technique can give valuable insight into the physiology of lymph propulsion, however. Results comparing injection pressures suggest that while uptake and infusion

flow rates depend on local tissue pressure, the net velocity of lymph (at least at the capillary level) does not. Unlike blood vessels, lymphatic capillaries have no smooth muscle and rely on elastic fibers which anchor their endothelial cells to the extracellular matrix to prevent collapse. As tissue swells, lymphatics are pulled open to create spaces for drainage. Furthermore, the capillaries drain to deeper vessels which have valves and smooth muscle but are nonetheless noncylindrical and easily distensible. Because of these features, it has been suggested that the lymphatics have an enormous capacity for drainage which is far beyond normal physiological requirements and that drainage rate depends linearly on IFP for up to at least ten times normal rates (ref). Our observations that interstitial fluid pressure and infusion flow rate do not affect lymph propulsion velocity support the idea that systemic rather than local forces govern lymph propulsion, and that velocity is independent of volumetric flow rate.

If net velocity is indeed independent of net flow, a simple mass balance might imply that the cross-sectional vessel area must change, possibly by vessel recruitment or diameter adjustments. This hypothesis is supported by our observations that the vessels appear larger, or more swollen, with higher injection pressures. However, only the net velocity in the superficial vessels has been measured in this study. Since the larger vessels may offer less resistance to flow than capillaries, velocities in these vessels may depend on uptake rate; such a theory cannot be postulated based on this experiment alone.

The microsphere studies, however, support the above hypothesis by showing that pressure changes due to expansion and contraction of the chest cavity are transmitted to lymphatic capillaries, possibly by creating a slight pump in the thoracic duct. For decades it has been observed that respiration affects lymphatic flow near the heart: it was observed as early as 1939 that forced expiration increases lymphatic pressures while inspiration causes a fall in pressure (Cressman and Blalock 1939); it was also shown that the highest lymph flow rates in the thoracic duct occurred at the end of inspiration (Browse *et al* 1974). The fact that these effects are seen in the tail, immobilized and isolated from the chest wall, suggests that respiration may induce a pressure drop in the major lymph vessels and create a pump throughout the entire lymphatic system.

FRAP measurements reveal a number of complexities of lymph flow that were not apparent with the integrative approaches of residence time analysis presented here. The broad range of velocities detected by FRAP shows that a large number of individual measurements must be made in order to characterize the lymphatic capillary network as a whole, and even so, sampling of the network is limited to geometrically and optically advantageous regions and cannot be completely random. However, the FRAP measurements display two important facts. First they show that despite the net flow in the

proximal direction, individual capillaries may exhibit retroflow or stagnation. Second, the mean magnitude of velocity decays with time, but the rapid flow is not necessarily proximally-directed.

One interpretation of these observations is that the injection causes large local pressure gradients and filling of portions of the network along preferential pathways, followed by the lateral or even retro filling of the more flattened or obstructed vessels so that complex flow patterns develop. At later times, the capillaries are more uniformly dilated and more vessels are involved in transport, so the average velocity is lower. The record of velocities in two individual capillaries shown in Figure 4-4 supports this hypothesis. One vessel, oriented normal to the tail axis, has a large initial velocity that declines to near zero. This may reflect lateral filling of the network due to the effects of local injection. The other vessel shown in the figure is more nearly parallel to the tail axis, and it maintains a more uniform velocity throughout the experiment. The velocity in this case is more clearly related to the transport of lymph away from the injection site, and therefore it suggests that flow is driven by a more constant systemic force.

The RTD analysis allows calculations of net velocity averaged over space and time. For comparison, therefore, FRAP velocities were averaged in each mouse. The mean average of local velocities was found to be $4.7 \mu\text{m/s}$. Since the RTD method measures a net velocity parallel to the tail axis, tortuosity needs to be accounted for when comparing the averages of each method. By considering the capillary network as a regular hexagonal mesh, the tortuosity factor was estimated to be 1.17; with this correction the average vessel velocity parallel to the tail axis is $4.0 \mu\text{m/s}$. This correlates well with the observed macroscopic or net velocity of $3.8 \pm 1.0 \mu\text{m/s}$, especially considering that velocities were only measured in vessels and not vessel intersections (which would further reduce the true FRAP average). Because the macroscopic velocity is the net sum of all the individual capillary velocities, the two independent characterization methods support each other. Note that since the FRAP measurement takes place over a much longer time scale than the oscillation frequency (approximately 40 breaths over the measurement), oscillation effects cannot be detected by FRAP.

While these two methods are in agreement, the information each gives is complementary to the other. The RTD method allows us to examine a net steady-state velocity, which has relatively little variation because it is measured over a long distance; this is useful in considering net physiological aspects of lymphatic transport. FRAP, on the other hand, accurately measures velocity in single capillaries, which varies greatly between vessels. While the RTD velocity is useful for revealing relationships between pressure,

flow, and uptake, FRAP is more appropriate for observing changes in local flow behavior or for studies in which a local velocity is necessary. Furthermore, the microspheres allow long-term flow visualization and fluid pathlines to be observed. In contrast, FRAP creates a transient tracer population that dissipates with time.

Chapter 5

Interstitial-lymphatic fluid balance¹

5.1 Introduction

In chapter 4, a quantitative model was established for investigating interstitial-lymphatic transport phenomena. RTD theory was used to follow fluorescent tracer movement, assumed to be related to fluid movement, and revealed a characteristic time associated with lymphatic uptake which depended on infusion pressure. Now that the experimental model had been established, the next step was to investigate more closely the mechanics of fluid balance.

Interstitial-lymphatic fluid movement is complex and poorly understood. Previous works constitute an incomplete picture, but provide enough evidence to postulate a theoretical basis for mechanical interactions within the tail skin model. We therefore attempted to incorporate known anatomical and physiological features of the lymphatic system into a mechanical framework of tissue fluid balance so that simple experiments in the mouse tail skin model could be used to quantify tissue transport parameters. Such a model would potentially be of key importance in exploring changes associated with lymphedema, for example, as well as any other alteration in tissue fluid balance which can be experimentally created in the mouse tail.

It has been established that interstitial fluid volume (IFV) and interstitial fluid pressure (IFP) both affect lymphatic flow (Hogan and Unthank 1986, Mortimer *et al* 1990, Aukland and Reed 1993, Granger 1979), and depending on the compliance and state of hydration of the tissue, IFP usually determines IFV. A swelling tissue may exert tensile stresses on the lymphatic endothelia via anchoring filaments (Leak 1976, Ryan 1989, Castenholz *et al* 1991a, Schmid-Schönbein 1990) to locally increase drainage during acute

¹ Part of this work is included in Swartz, MA, PA Netti, C Brekken, Y Boucher, and RK Jain. Mechanics of interstitial-lymphatic fluid transport: theoretical foundation and experimental validation. (In press)

swelling. Furthermore, the anchoring filaments are structurally and molecularly similar to the elastic fibers of the extracellular matrix, suggesting functional continuity with the interstitium (Gerli *et al* 1991). External stresses such as massage can temporarily increase local drainage as well as internal factors which transmit mechanical signals through the tissue (such as vasomotion, muscular activity, and respiration) to influence lymphatic clearance (Negrini *et al* 1994, Aukland and Reed 1993, Schmid-Schönbein 1990). Clearly, lymphatic function is intrinsically and dynamically coupled to the interstitium. Previous evaluations of lymphatic function, however, have largely neglected the dynamics of the interstitium. Furthermore, most biphasic models of tissue mechanics (Mow *et al* 1984, Grodzinsky 1983, Barry and Aldis 1990, Holmes 1986, Jönsson and Jönsson 1992, Blake 1989) typically describe cases in which lymphatic drainage does not play a key role in fluid-solid tissue equilibrium.

In this chapter, the relationship between tissue fluid balance and lymphatic function is explored by incorporating a relevant theoretical framework with the mouse tail skin model (for experimental details, see Chapter 3). The continuous interstitial infusion into the tip of the tail creates gradients in pressure and stress within the interstitium. The spatial profiles of these gradients depend on the hydraulic conductivity of the tissue as well as the overall drainage capacity of the lymphatics. Temporal gradients depend additionally on the tissue elasticity. This relationship is depicted in Figure 5-1. A poroelastic description of interstitial-lymphatic fluid convection was developed to predict the hydrostatic pressure distribution within the tissue according to its elastic properties and the overall functioning of the lymphatic system. The theory is substantiated with measurements of pressure in the mouse tail following an infusion of saline. Also, *in vitro* measurements of the elastic modulus are used to support the *in vivo* data. Confined compression tests were performed in the laboratory of Dr. Alan Grodzinsky and are described in Section 3.7. This framework allows us to evaluate the relative resistances to fluid transport as well as to estimate *in situ* the hydraulic conductivity of the tissue, its elastic modulus, and an effective resistance to lymphatic uptake. More importantly, it provides a tool in which the mechanisms of interstitial-lymphatic fluid transport can be distinguished and evaluated quantitatively. Finally, it forms the necessary foundation for analogous studies of interstitial-lymphatic molecular transport.

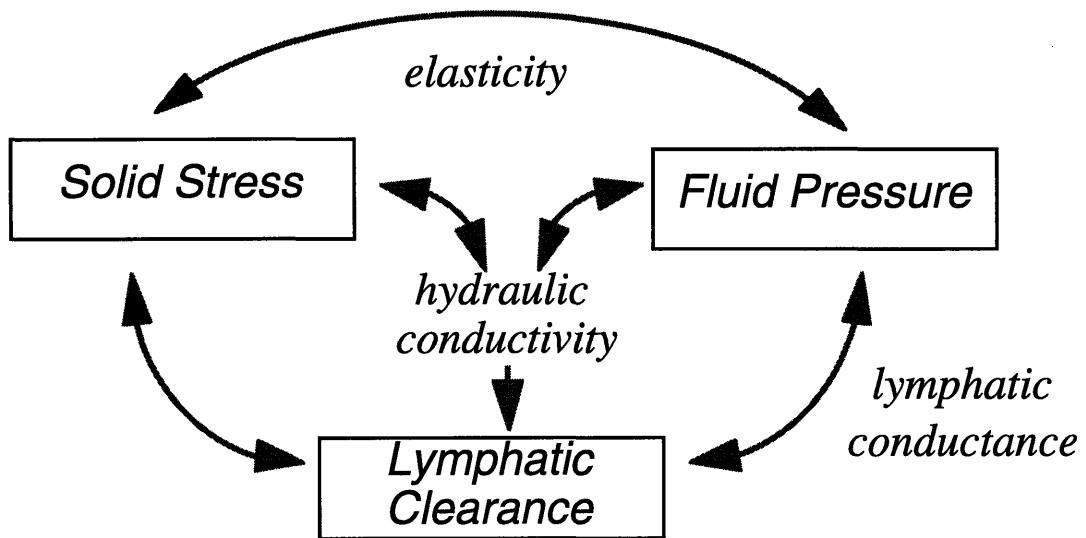


Figure 5-1. Mechanical aspects of tissue fluid balance.

Modeling foundation

A step increase in IFP at the tip of the tail results in a transient response 3.2 mm downstream which is shown in Figure 5-2. In a rigid porous matrix, we would expect a pressure wave to travel at the speed of sound in water. In the tissue, however, the characteristic time for mechanical equilibration is shown below to be on the order of 8 minutes. In order to describe this transient response, therefore, the tissue cannot be treated as a rigid porous matrix and the elastic component of the interstitium must be accounted for which responds to stress (pressure) with a resulting strain (swelling). It is the elasticity of the tissue which determines this stress-strain relationship, and the speed of propagation of stress or strain depends on the tissue's elastic modulus.

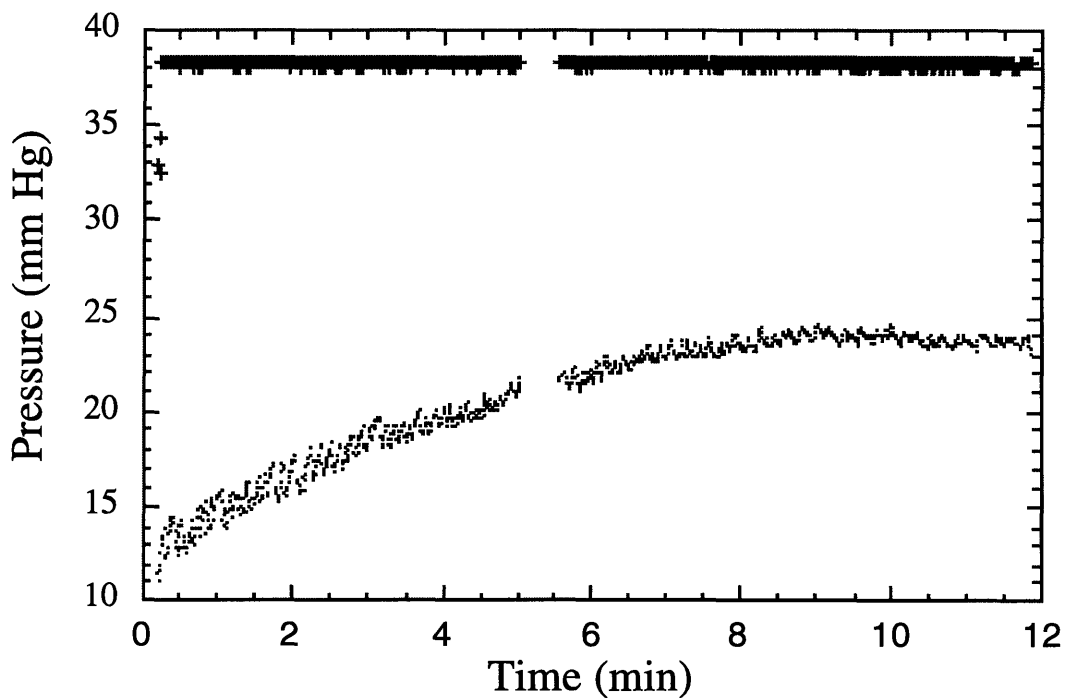


Figure 5-2. Interstitial fluid pressure (dots) measured approximately 3.2 mm downstream following a step infusion of saline at 52 cm water (38.5 mm Hg). Plus symbols show the infusion pressure measured in the infusion line.

5.2 Theory

5.2.1 General

In the following analysis, gradients in tissue stress resulting from an interstitial injection are described by a balance between interstitial flow and lymphatic function. A poroelastic framework is based on a previously developed model to describe fluid movement in solid tumors with capillary reabsorption (Netti *et al* 1997); here the focus is on the role of the lymphatics in controlling this mechanical relationship.

The tissue is regarded as a fluid-filled, porous elastic solid matrix. The fluid and solid phases are each inherently incompressible and tissue deformation is described as a change in fluid volume fraction ε . The two phases are thus assumed to exist in mechanical equilibrium. Considering the tissue continuum, a quasi-static stress balance is assumed:

$$\nabla \cdot \underline{\underline{\boldsymbol{\tau}}} = 0 \quad (5.1)$$

where $\underline{\underline{\boldsymbol{\tau}}}$ is the tissue stress tensor.

A constitutive law is needed to define the stress tensor and approximate the elastic behavior of the solid matrix. For fast deformation, the stress-strain relationship may show time-dependent behavior and thus require a viscous component in the constitutive law. However, if the deformation is slow enough, quasi-static stress-strain relationship may be assumed. This infinitesimal strain approximation results in linear elastic behavior:

$$\underline{\underline{\boldsymbol{\tau}}} = -P\underline{\underline{\boldsymbol{I}}} + \lambda e\underline{\underline{\boldsymbol{I}}} + 2\mu\underline{\underline{\boldsymbol{\mathcal{E}}}} \quad (5.2)$$

where P is hydrostatic (thermodynamic) pressure, $\underline{\underline{\boldsymbol{I}}}$ is the identity tensor, e is the dilatation of the solid phase, $\underline{\underline{\boldsymbol{\mathcal{E}}}}$ is its strain tensor (Cauchy infinitesimal strain, not to be confused with the fluid volume fraction ε), and λ and μ its intrinsic elastic (Lamé) constants. If \boldsymbol{u} is defined as the solid displacement vector, then the dilatation is given as

$$e = \nabla \cdot \boldsymbol{u} \quad (5.3)$$

and the strain tensor is

$$\underline{\underline{\epsilon}} = 1/2 (\nabla \underline{\underline{u}} + \nabla \underline{\underline{u}}^T). \quad (5.4)$$

Therefore, $e = \text{Tr}(\underline{\underline{\epsilon}})$ and is dimensionless. Since the experimental model utilizes a slow interstitial infusion (on the order of 0.1 $\mu\text{l}/\text{min}$, or 1% tissue volume comprising the characteristic length per min) into a low-compliant tissue, small gradients in hydration and thus small strains of the interstitial matrix are inferred. This is verified *a posteriori*.

For a symmetric system, the isotropic normal stress (i.e., pressure) can be related to the dilation of the solid matrix:

$$\begin{aligned} 0 &= \nabla \cdot \underline{\underline{\tau}} \\ &= \nabla \cdot (-P \underline{\underline{I}} + \lambda e \underline{\underline{I}} + 2\mu \underline{\underline{\epsilon}}) \\ &= \nabla \cdot (-P \underline{\underline{I}} + \lambda (\nabla \cdot \underline{\underline{u}}) \underline{\underline{I}} + \mu (\nabla \underline{\underline{u}} + \nabla \underline{\underline{u}}^T)) \\ &= -\nabla P + \nabla e (2\mu + \lambda) \end{aligned}$$

Thus,

$$\nabla P = (2\mu + \lambda) \nabla e. \quad (5.5)$$

Therefore, the parameter $(2\mu + \lambda)$ represents the effective bulk elastic modulus and is usually denoted as H in the literature (Fung 1981). Assuming the mutual drag forces between fluid and solid phases are linearly proportional to the relative velocity through the matrix, a generalized Darcy's Law is used to describe the bulk interstitial fluid movement:

$$\epsilon \left(\bar{\underline{\underline{v}}} - \frac{\partial \bar{\underline{\underline{u}}}}{\partial t} \right) = -K \nabla P \quad (5.6)$$

where $\bar{\underline{\underline{v}}}$ is the average pore fluid velocity, $\bar{\underline{\underline{u}}}$ the average solid displacement, ϵ is the fluid volume fraction (not to be confused with the strain tensor $\underline{\underline{\epsilon}}$) and K the intrinsic permeability or hydraulic conductivity of the tissue matrix (per gram of tissue). In other words, K relates the *relative* bulk fluid velocity (relative to the solid) to the pressure gradient. In this form, K represents an *intrinsic* tissue conductivity, independent of the cross-sectional area.

In the following analysis, K is assumed constant because within the characteristic length of the infusion, swelling should be maximal and therefore changes in the parameters small compared to their values. In this way they represented bulk-averaged parameters in the infusion region, where all of the measurements were made. As seen from the results, these assumptions proved relevant and valid for the experimental model used and the conditions imposed. For other purposes, e.g. smaller pressure gradients or more compliant tissues, modifications to the theoretical framework may be necessary. In fact, a functional form for K does not need to be specified until a solution is desired (Equation 5.16). For example; if changes in hydration are significant, K may be written as a function of ε :

$$K = K_o \left(\frac{\varepsilon}{1 - \varepsilon} \right)^b \quad (5.7)$$

as observed *in vitro* (Bert and Fatt 1970, Levick 1987, Mow *et al* 1986)

Continuity equations for the fluid and solid phases complete the description. Let ρ_f and ρ_s denote the fluid and solid fractions, respectively. If fluid mass is conserved except for that which is drained by the lymphatics, and solid mass is conserved, we have

$$\frac{\partial \rho_f}{\partial t} + \nabla \cdot (\rho_f \bar{v}) = -J_v \rho_{tissue}$$

and

$$\frac{\partial \rho_s}{\partial t} + \nabla \cdot \left(\rho_s \frac{\partial \bar{u}}{\partial t} \right) = 0,$$

where J_v is the net lymphatic drainage or volumetric flux (i.e. J_v [=] vol. lymph formed per unit tissue volume per time). Since $\rho_f = \varepsilon \rho_{tissue}$, and $\rho_s = (1 - \varepsilon) \rho_{tissue}$, these become

$$\frac{\partial \varepsilon}{\partial t} + \nabla \cdot (\varepsilon \bar{v}) = -J_v \quad (5.8)$$

and

$$-\frac{\partial \varepsilon}{\partial t} + \nabla \cdot \left((1 - \varepsilon) \frac{\partial \bar{u}}{\partial t} \right) = 0. \quad (5.9)$$

These are then combined to give a total continuity law

$$\nabla \cdot \left((1 - \varepsilon) \frac{\partial \bar{u}}{\partial t} + \varepsilon \bar{v} \right) = -J_v. \quad (5.10)$$

Regardless of its physiological mechanism, the flux J_v represents a sink for convecting fluid and would require a relative density of lymphatic capillaries large enough to maintain the tissue continuum approximation. Although the lymphatics are primarily responsible for the fluid uptake following an intradermal injection, the flux term must incorporate all mechanisms of fluid drainage such as capillary reabsorption. Furthermore, the representation of lymphatic drainage as a disappearance of fluid pressure implies that although the lymphatic vessels themselves may occupy space in the tissue continuum, any changes in their volume are negligible. In other words, the rate of fluid entry into the lymphatics is assumed to equal the volumetric fluid flux within the lymphatics at any given cross-section of tail.

In defining the lymphatic flux, the local and systemic mechanisms are combined in series. Because of the high permeability of the lymphatics and isotonicity of the infused solution, it is assumed that hydrostatic pressure differences dominate the Starling fluid flux across the lymphatic capillary wall:

$$J_v(\text{Starling}) = L_p S/V (P_i - P_l) \quad (5.11)$$

where L_p is the average permeability of the lymphatic capillaries ($\text{vol} \cdot \text{area}^{-1} \cdot \text{time}^{-1} \cdot \text{mmHg}^{-1}$), S/V is their average density (ratio of surface area to tissue volume), and P_i and P_l are interstitial and lymphatic pressures, respectively. We assume that the interstitial pressure imposed by the infusion is much larger than normal IFP in the anesthetized animal (Aukland *et al* 1984, Aukland and Reed 1993, Schmid-Schönbein 1990, Zaugg-Vesti *et al* 1993) and thus dominates the forces which drive lymphatic uptake. Finally, we represent fluid drainage from the capillaries into the deeper lymphatics as driven by a pressure difference $P_i - P_b$, where P_b is a hypothetical baseline pressure resulting from the various factors which collectively contribute to the systemic lymph pump. These factors include myogenic activity of the collecting lymphatic vessels, muscular movements, and respiratory oscillations (Granger 1979, Aukland and Reed 1993, Schmid-Schönbein 1990, Negrini *et al* 1994). This baseline “pressure” maintains the driving force for systemic lymph circulation and will be considered constant (i.e. systemic lymph flow is unaffected by the

perturbation at the tail tip). If the drainage rate of a lymphatic capillary is much slower than its filling rate, P_l will be close to P_i and flux will be limited by the capability of the deeper lymphatics to pump and drain lymph rather than local Starling forces. By lumping these together into a total resistance term R_t , the local lymphatic uptake rate can be considered proportional to $P_i - P_b$, or P^* , accordingly:

$$J_v = \beta(P_i - P_b) = \beta P^* \quad (5.12)$$

where β represents the effective “conductance” for lymphatic uptake (vol. lymph·vol. tissue⁻¹·time⁻¹·mmHg⁻¹). Considering an overall resistance to uptake, R_t or $1/\beta$ is then the sum of the resistance to lymphatic drainage in series with the net systemic resistance R_s :

$$\frac{1}{\beta} = R_t = \left(\frac{1}{L_p S/V} + R_s \right) \quad (5.13)$$

Thus, the major assumption here is not that intralymphatic pressure is constant but rather that systemic forces maintain an overall constant resistance to flow.

Coupling Equations 5.10 and 5.12, the continuity equation for the tissue can be expressed as:

$$\begin{aligned} \beta P^* &= \nabla \cdot \left[\frac{\partial \bar{u}}{\partial t} (\varepsilon - 1) - \varepsilon \bar{v} \right] \\ &= \frac{\partial}{\partial t} (\nabla \cdot \bar{u}) (\varepsilon - 1) - \varepsilon (\nabla \cdot \bar{v}) \\ &= (\varepsilon - 1) \frac{\partial e}{\partial t} - \varepsilon (\nabla \cdot \bar{v}) \end{aligned} \quad (5.14)$$

where P^* is the difference ($P_i - P_b$).

Returning to fluid momentum, the divergence of Eq. 5.6 yields:

$$\varepsilon \left(\nabla \cdot \bar{v} - \frac{\partial}{\partial t} (\nabla \cdot \bar{u}) \right) = -\nabla \cdot (K \nabla P^*)$$

or

$$\left(\varepsilon \nabla \cdot \bar{v} - \varepsilon \frac{\partial e}{\partial t} \right) = -K \nabla^2 P^* - \nabla K \cdot \nabla P^* \quad (5.15)$$

Note that the functionality of K has not been specified and thus the possibility to include specific cases of variable K is maintained. However, if we assume that $K \nabla^2 P^* \gg \nabla K \cdot \nabla P^*$, which would be a reasonable assumption for normal skin with moderate values of elasticity, then the last term on the right-hand side of Eq. 5.15 can be neglected. Hydration, or isotropic strain, is related to interstitial pressure by the elastic modulus $(2\mu + \lambda)$; *i.e.* $\frac{\partial e}{\partial t} = (2\mu + \lambda)^{-1}$. If K is related to strain by Eq. 5.7, then

$$\frac{\partial K}{\partial P^*} = K_o b \left(\frac{\varepsilon}{1 - \varepsilon} \right)^{b-1} (1 - \varepsilon)^{-2} \left(\frac{\partial \varepsilon}{\partial P^*} \right) = \frac{Kb}{\varepsilon(1 - \varepsilon)(2\mu + \lambda)}.$$

For the condition $K \nabla^2 P^* \gg \nabla K \cdot \nabla P^*$ to hold in 1-D space, it must be true that

$$K \frac{\partial^2 P^*}{\partial x^2} \gg \frac{\partial K}{\partial P^*} \left(\frac{\partial P^*}{\partial x} \right)^2.$$

This is approximately equivalent to

$$K \frac{P^*}{x^2} \gg \frac{Kb}{\varepsilon(1 - \varepsilon)(2\mu + \lambda)} \frac{P^{*2}}{x^2}$$

or, simply, $\varepsilon(1 - \varepsilon)(2\mu + \lambda) \gg \beta P^*$. For illustration, let us take approximate values which were found for normal mouse tail skin (see Section 5.3): for an applied P^* of approximately 10 mm Hg, $(2\mu + \lambda)$ was on the order of 10^2 mm Hg. A typical value for b is 0.5 (Bert and Reed 1995), and ε is on the order of 0.5. With these values, the inequality holds. However, for edematous tissues, ε and b increase while $(2\mu + \lambda)$ decreases, disputing the validity of this simplification. This is explored in Chapter 7.

If we do neglect this last term, then Eq. 5.15 can be combined with the continuity and stress-strain relations (Equations 5.14 and 5.5, respectively) to yield the governing equation for tissue strain:

$$\frac{\partial e}{\partial t} - K(2\mu + \lambda)\nabla^2 e + \beta P^* = 0 \quad (5.16)$$

5.2.2 Application to the experimental model

The mouse tail is an ideal experimental model both from a practical as well as theoretical point of view. If we consider the tail as a long, thin rod² (1-2 mm diameter) composed mainly of dermis and subcutis between an epidermal layer and bone (Fig. 3-4), an approximate one-dimensional pressure gradient can be induced in the dermal-subcutaneous layer by inducing a step change of pressure at the tip. By measuring the IFP with a micropipette, the response of the tissue to this step change, both transient and spatial, can be evaluated. Theoretically, this system is advantageous in many ways. First, only axial gradients are considered, assuming that radial strain (and thus IFP) equilibration is fast compared to that in the axial direction. This assumption is justified by a simple scaling analysis (the radius is an order or magnitude smaller than the characteristic axial length, which will be verified *a posteriori*) and frees us from making assumptions about isotropic transport parameters in the tissue. Also, the induced pressure gradient dominates any baseline physiological fluctuations in pressure as well as the estimated changes in osmotic pressure which makes it the primary driving force for convection. Finally, since fluid is injected into the tip and can only travel in the proximal direction (presumably within the dermis and subcutaneous space), it constitutes a geometrically closed system.

First we need to relate the measurable quantity - interstitial fluid pressure - to the tissue dilatation of Equation 5.16. We saw from Eq. 5.5 that $\nabla P^* = (2\mu + \lambda)\nabla e$, but the time dependence of P needs to also be related with that of e . Starting from Eq. 5.5,

$$\frac{\partial}{\partial t}(\nabla P^*) = (2\mu + \lambda)\frac{\partial}{\partial t}(\nabla e).$$

² The tail has approximately uniform diameter between 0.5 and 2 cm from the tip, which is well within the region of measurement or characteristic length.

For a one-dimensional system,

$$\frac{\partial}{\partial x} \left(\frac{\partial P^*}{\partial t} \right) = (2\mu + \lambda) \frac{\partial}{\partial x} \left(\frac{\partial e}{\partial t} \right),$$

and upon integration,

$$\frac{\partial P^*}{\partial t} \Big|_x = (2\mu + \lambda) \frac{\partial e}{\partial t} \Big|_x + f(t).$$

Since the tissue is considered a semi-infinite medium, we have the condition that as $x \rightarrow \infty$, $\frac{\partial P^*}{\partial t} = \frac{\partial e}{\partial t} = 0$. Thus, $f(t) = 0$ and the governing equation can now be expressed in terms of pressure

$$\frac{1}{(2\mu + \lambda)} \frac{\partial P^*}{\partial t} - K \frac{\partial^2 P^*}{\partial x^2} + \beta P^* = 0 \quad (5.17)$$

with the conditions of a step increase in pressure at the boundary

$$\begin{aligned} P^*(0, t) &= P_o^*, \\ P^*(\infty, t) &= 0, \\ P^*(x, 0) &= 0, \end{aligned} \quad (5.18)$$

where P_o^* is the applied pressure ($P_o - P_b$). Thus, the distribution of pressure is governed by the “stress diffusivity” or effective fluid conductance, $K(2\mu + \lambda)$ or K^* , and overall lymphatic conductance, $\beta(2\mu + \lambda)$ or β^* . Here the ratio $\alpha = \sqrt{K/\beta}$ is introduced as a characteristic penetration length to describe these relative resistances to fluid transport and which governs the steady-state pressure profile.

The analytical solution to Equations 5.17-18 was first solved for heat conduction in a thin wire, where convection is approximated as a homogeneous generation term for high

Biot numbers (Carslaw and Jaeger 1947), and then for chemical diffusion and adsorption into a semi-infinite medium by Danckwerts (1953). This is:

$$\frac{P^*(x,t)}{P_o^*} = \frac{1}{2} e^{-x/\alpha} \operatorname{erfc}\left(\frac{x}{2\sqrt{K^*t}} - \sqrt{\beta^*t}\right) + \frac{1}{2} e^{x/\alpha} \operatorname{erfc}\left(\frac{x}{2\sqrt{K^*t}} + \sqrt{\beta^*t}\right) \quad (5.19)$$

According to this model, the steady state pressure (P_{ss}^*) will decrease exponentially with distance according to the ratio of tissue to lymphatic conductivities (α):

$$P_{ss}^* = P_o^* e^{-x/\alpha} \quad (5.20)$$

If the tissue poses a much greater resistance to fluid transport than the lymphatics, we would expect a steep pressure profile within a short penetration depth; conversely, if the lymphatics were nonfunctional, IFP would eventually become constant everywhere.

Therefore, by measuring transient and steady-state pressure profiles, the quantities $K(2\mu+\lambda)$, $\beta(2\mu+\lambda)$, and their ratio α^2 can be estimated. Because the speed of pressure propagation depends intrinsically on the tissue elasticity ($2\mu+\lambda$), the transport parameters K and β cannot be separated. However, their product can be estimated from a total mass balance on the injection. Since injected fluid moves through the tissue until it is taken up by the lymphatics (or blood circulation), the net flow rate Q into the tail must equal the total lymphatic uptake rate integrated over the tail.

$$Q = \int_0^{\infty} \beta P^* \cdot A_c \cdot dx.$$

Here, A_c is the cross-sectional area of the tail through which fluid flows, assuming that dermal and subcutaneous tissue poses less resistance to flow than the other local tissue compartments, and is estimated from stained images of tail cross-sections. This can be evaluated at steady state:

$$Q_{ss} = \int_0^{\infty} \beta P_o^* e^{-x/\alpha} \cdot A_c \cdot dx = A_c \cdot \sqrt{\beta K} P_o^* \quad (5.21)$$

Thus, by measuring the injection flow rate along with the steady-state pressure profile³, a complete analysis of the system is provided and the estimation of each parameter is possible.

5.2.3 Special case of oscillating pressure

In addition to a step increase in pressure at the boundary, the system was analyzed for the condition of oscillating boundary pressure, since natural intrinsic stresses within a tissue are typically oscillatory. Although these were not explored experimentally because of technical feasibility, the theoretical pressure profiles and total uptake rates in oscillating stress conditions were compared with those from the constant pressure boundary condition. Oscillations were imposed about the same pressure magnitude:

$$P^*(0, t) = P_o^*(1 + \sin \omega t), \quad (5.22)$$

Duhamel's Theorem (Carslaw and Jaeger 1959, p.31) can be used to solve Equations 5.17 and 5.22:

$$P_{osc}^* = \int_0^t (1 - \sin \omega \varphi) \frac{\partial P^*(t - \varphi)}{\partial t} d\varphi; \quad (5.23)$$

where P^* is the constant-surface pressure solution from Equation 5.19. The total fluid flow rate, or total lymphatic drainage rate, is then

$$Q_{osc}(t) = \beta \int_0^\infty \int_0^t (1 - \sin \omega \varphi) \frac{\partial P^*(t - \varphi)}{\partial t} d\varphi dx. \quad (5.24)$$

³ Theoretically, all three parameters could be evaluated simply from the initial transient profile of injection flow rate:

$$\begin{aligned} Q(t) &= -KA \left. \frac{\partial P^*(t)}{\partial x} \right|_{x=0} \\ &= -KA \left(\frac{1}{\sqrt{\pi K(2\mu + \lambda)}} (1 - e^{-\beta(2\mu + \lambda)t}) + \frac{1}{\alpha} \operatorname{erf}(\sqrt{\beta(2\mu + \lambda)t}) \right). \end{aligned}$$

However, because of the lack of a sensitive flow meter, this is not experimentally feasible.

Pressure profiles and flow rates were computed numerically using the parameter values given in Table 5.1.

5.2.4 *In vitro* elastic modulus

For comparison with the *in situ* data, *in vitro* stress-strain tests were performed by confined compression using a Dynastat apparatus as previously described (Frank and Grodzinsky 1987) to estimate the elasticity of mouse tail skin during compression. Tail skin was excised immediately after sacrifice by making two circumferential incisions approximately 1 cm apart, joining them with a third axial incision, and carefully ‘peeling’ the skin from the bone using a hemostat and scalpel. From this tissue, a 3-mm disk was bored and placed in a confined compression chamber. Placement was specifically epidermal-side down, with the assumption that the epidermis has a higher elastic modulus than the dermis and subcutis so that stress (measured from the top) resulted from the dermal and subcutaneous tissue only. Displacements of 25 μm were imposed over a period of 15 seconds and the resulting steady-state stress measured for a total of 6 displacements

5.3 Results

5.3.1 Tissue fluid balance parameters

Results of pressure propagation from a typical experiment are shown in Figures 5-3 and 5-4. The ratio α was estimated by fitting the spatial pressure profile to Eq. 5.20. Furthermore, the intercept (relative position where $P=P_o$) determined the infusion “origin” ($x=0$) from which the transient positions could be adjusted accordingly.

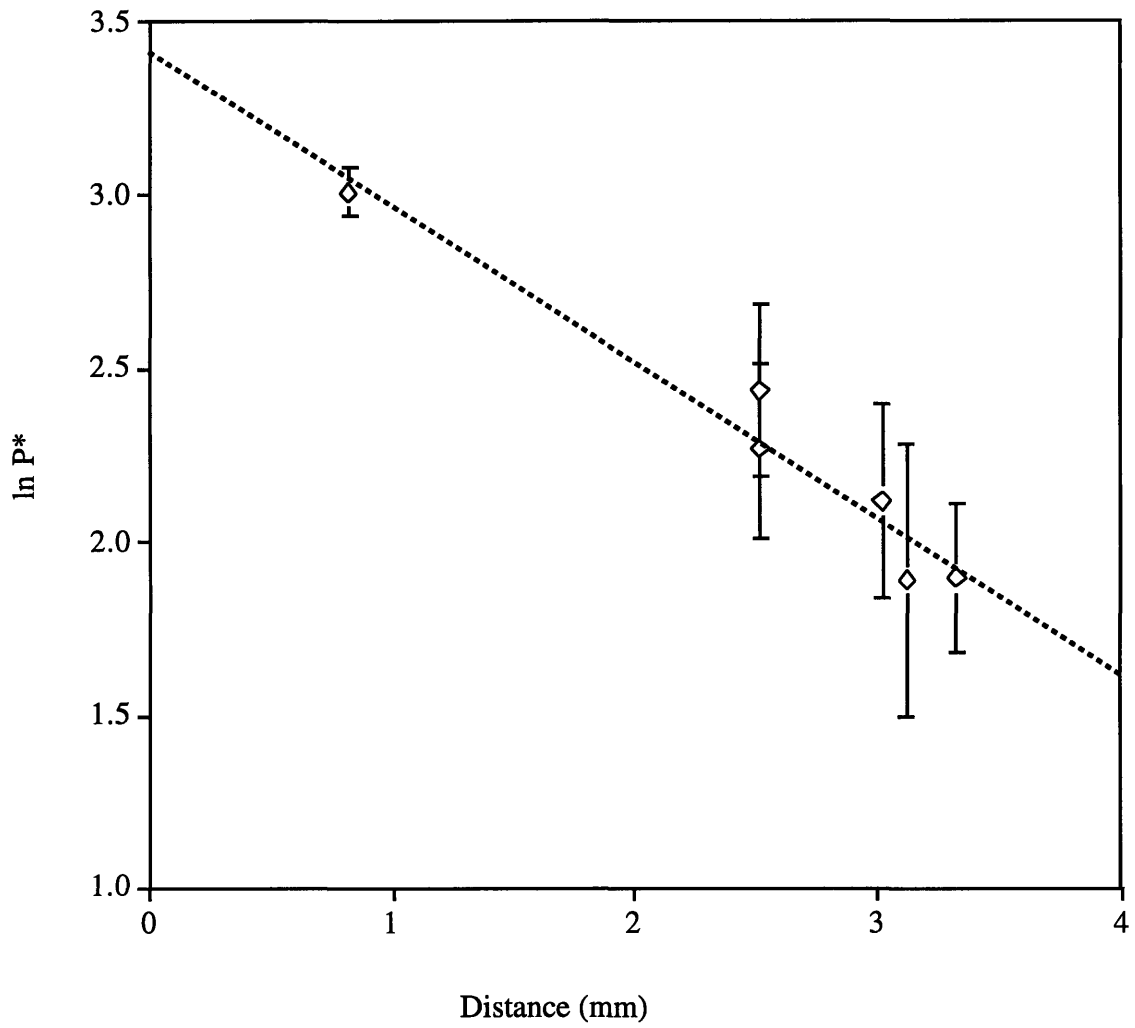


Figure 5-3. Spatial pressure profile from a typical experiment (the same as shown in Figure 5-2) after a steady state had been established.

In all experiments, the steady infusion flow rate (which stabilized after no more than 10 minutes in all cases) was linearly proportional to infusion pressure in the range used, and, according to Eq. 5.21, resulted in estimates of β and K when combined with α . The cross-sectional area A_c , determined by analysis of histological sections (Figure 3-4), was found to be $65\pm 4\%$ of the total tail cross-section ($\pi d^2/4$). For the 5 mice used in the experiments, this area was determined from diameter measurements at approximately 1 cm from the tip and averaged 0.8 ± 0.2 mm² (mean \pm s.d.). Diameter was unchanging, to the precision of our measurement, within injection region (2-10 mm). The pressure-flow relationship from this particular experiment is shown in Figure 5-4.

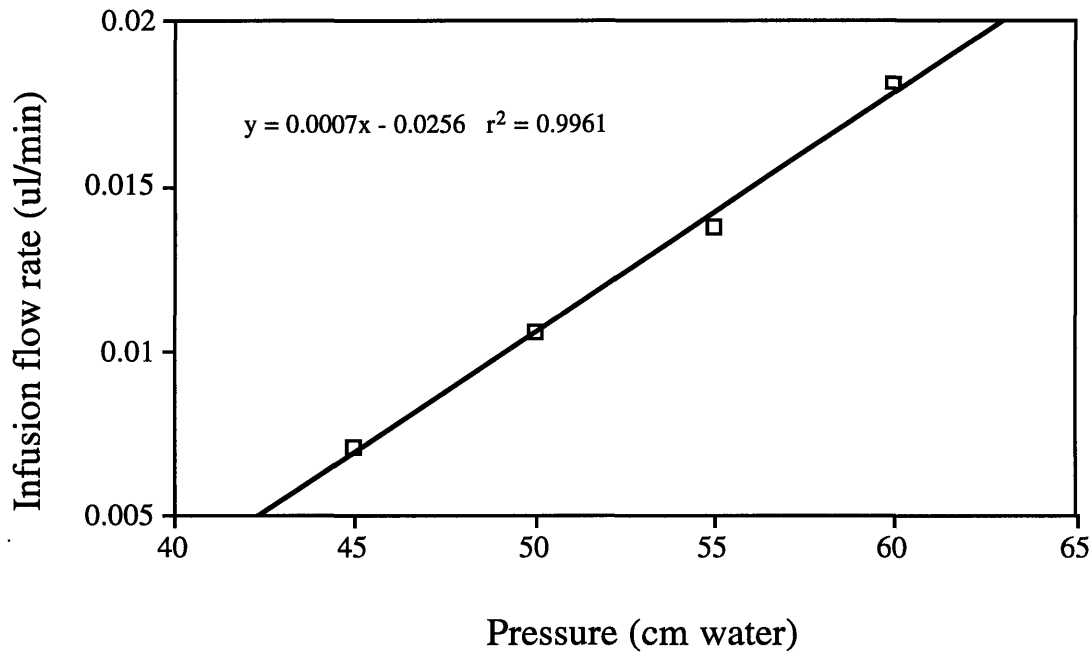


Figure 5-4. Typical data showing the dependence of infusion flow rate on infusion pressure.

Finally, using these values for x and α , the transient profile was fit to Equation 5.19 using Matlab (Mathworks, Inc., Natick, MA) to determine the pressure diffusivity $K^* = K(2\mu + \lambda)$. The fit to the data is shown below in Figure 5-5.

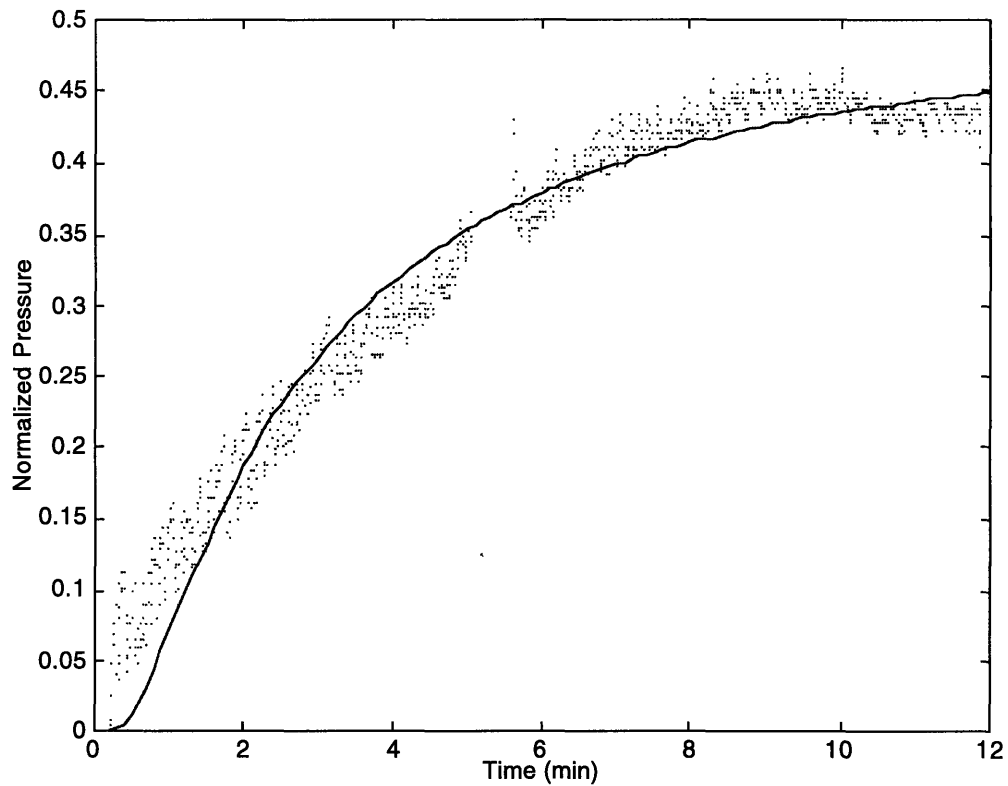


Figure 5-5. The transient IFP profile at 3.2 mm (the same data as shown in Fig. 5-3), normalized to the infusion pressure, and its fit to Equation 5.19 (solid line).

Results from the 5 experiments are summarized in Table 5.1. Baseline pressures were measured approximately 1 cm from the tip of the tail. Individual data from each experiment is given in Appendix B.

	<u>Mean</u> \pm <u>s.d.</u>
Baseline pressure P_b (mm Hg)	9 ± 6
Infusion flow rate for 50 cm water (37 mm Hg) infusion ($\mu\text{l}/\text{sec}$)	$2 \pm 1 \times 10^{-3}$
Steady-state ratio $\alpha = \sqrt{K/\beta}$ (cm)	0.23 ± 0.07
Effective lymphatic conductance β ($\text{sec}^{-1} \cdot \text{mm Hg}^{-1}$)	$4 \pm 2 \times 10^{-5}$
Interstitial hydraulic conductivity K ($\text{cm}^2 \cdot \text{sec}^{-1} \cdot \text{mm Hg}^{-1}$)	$1.5 \pm 0.4 \times 10^{-6}$
Tissue elasticity $2\mu + \lambda$ (longitudinal modulus) (mm Hg)	110 ± 20

Table 5.1. Results of 5 experiments with infusion pressures of 40-60 cm water.

Although a wide range of baseline pressures and infusion flow rates was measured among the experimental animals, a remarkable consistency is seen for their gradients and therefore the calculated parameter values. The sensitivities of the theoretical fit to the parameters α and K^* are shown in Figure 5-6.

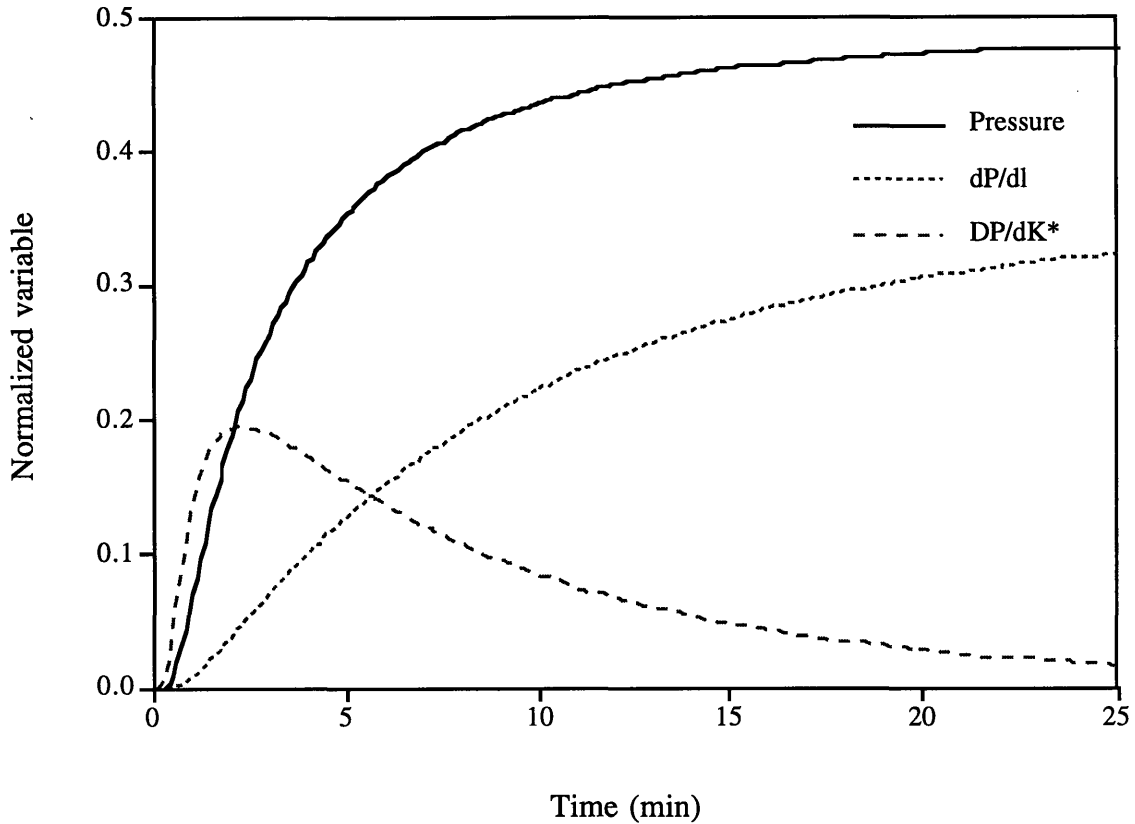


Figure 5-6. Sensitivity analysis of the transient pressure profile on the variables given in Eq. 5.19. The solid line is the normalized pressure profile, where $P^{**} = \frac{P^*}{P_o^*} = \frac{P - P_{base}}{P_{inflation} - P_{base}}$, using the parameters obtained from the data in Figure 5-4 (i.e. the best fit of this data). The dotted line shows the sensitivity of this profile to the ratio $\alpha = \sqrt{K/\beta}$, or a normalized $\frac{\partial P^{**}}{\partial \alpha} = \frac{\alpha_o}{P^*} \frac{\partial P^*}{\partial \alpha}$, and controls the steady-state value of the pressure (important at longer times). On the other hand, the parameter $K^* = K(2\mu + \lambda)$ governs the initial shape of the pressure propagation and dominates the initial reaction, and is shown by the dashed line $\frac{\partial P^{**}}{\partial K^*} = \frac{K_o}{P^*} \frac{\partial P^*}{\partial \alpha}$.

5.3.2 In vitro parameters

After the application of a fixed strain in the confined compression tests, the load was recorded as the fluid was drained from the tissue. The steady-state stress is then related to the unidirectional solid displacement u_x by the elastic modulus:

$$\tau_{xx} = (2\mu + \lambda) \frac{du_x}{dx} \quad (5.25)$$

The stress responses of the confined compression tests were measured for 6 successive displacements to estimate the modulus. This parameter was fairly consistent for up to 20% compression for 4 tests. $(2\mu + \lambda)$ was found to be 240 ± 60 mm Hg (mean \pm s.d.). Considering the important differences between the *in vitro* and *in situ* measurements, such as excised vs. living tail skin, radial vs. axial strains, and compressive vs. swelling stresses, the results from the confined compression tests serve to give validity to our *in situ* model and are discussed in the next section.

5.3.3 Oscillating surface pressure simulations

When an oscillating pressure is imposed at the boundary, it propagates within the tissue in an analogous manner to that of constant pressure. As seen in Figure 5-7(a), an oscillating pseudo-steady state is achieved, which leads to oscillating drainage rates (Figure 5-7(b)). As expected from the theoretical foundation, these drainage rates yield identical drainage volumes (Figure 5-7(c)).

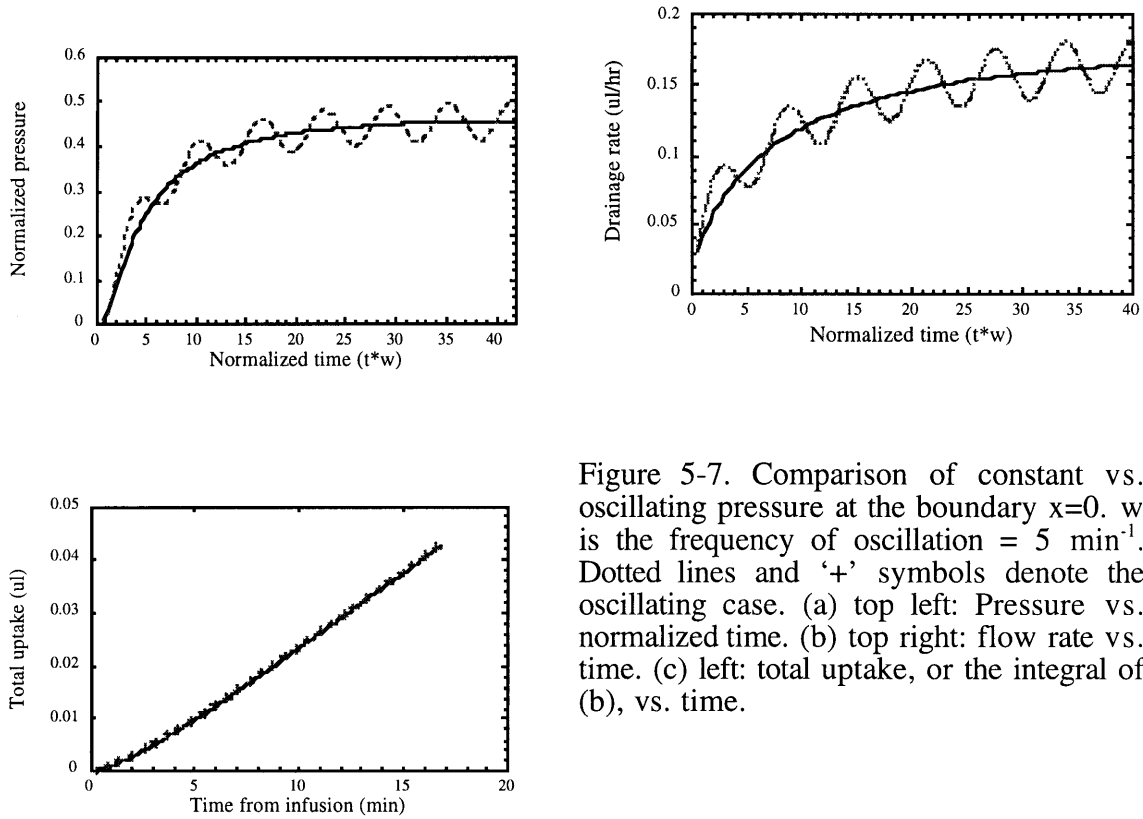


Figure 5-7. Comparison of constant vs. oscillating pressure at the boundary $x=0$. w is the frequency of oscillation = 5 min^{-1} . Dotted lines and '+' symbols denote the oscillating case. (a) top left: Pressure vs. normalized time. (b) top right: flow rate vs. time. (c) left: total uptake, or the integral of (b), vs. time.

5.4 Discussion

The coupling between tissue mechanics and fluid flow has been described by biphasic and poroelastic models which have been useful in elucidating biomechanical functions of tissues such as bone and articular cartilage (Barry and Aldis 1990, Mow *et al* 1984, Grodzinsky 1983, Simon 1992) where deformation-induced fluid flow dominates any other fluid transport mechanisms. In other tissues such as skin, the lymphatics may play a more important role in governing fluid distribution. The aim of this chapter was to evaluate the mechanical relationships among key variables which control interstitial-lymphatic fluid balance (i.e. Figure 5-1) and utilize the mouse tail model to examine this description. The model was based on the assumption that the balance between stress (hydrostatic pressure), strain (hydration), and lymphatic drainage was governed by three tissue parameters - effective tissue elasticity, hydraulic conductivity, and lymphatic conductance - which were taken as effective or bulk-averaged constants within the injection region. Although not without limitations, our model could predict the mechanical response of a tissue to a controlled perturbation and yielded estimates of the effective tissue parameters, albeit in swollen rather than normal states. Furthermore, the experimental data confirmed that lymphatic drainage is an important determinant of interstitial fluid movement in tissues such as skin and should be considered in modeling the mechanics of such tissues. This is shown in Figure 5-3, where the stress distribution within a lymphatic-rich tissue resulting from a continuous infusion is governed by the penetration length or ratio between lymphatic and interstitial resistances. The characteristic time for the redistribution of fluid pressure, T_p , following such a perturbation depends on tissue elasticity as well as lymphatic drainage:

$$T_p \approx \frac{1}{\beta(2\mu + \lambda)} = \frac{\alpha^2}{K(2\mu + \lambda)} \quad (5.26)$$

Since the propagation of the pressure wave generated by an interstitial injection in a poroelastic medium is determined by $K(2\mu + \lambda)$, the effect of lymphatic drainage is a reduction in the apparent propagation speed. This is shown in Figure 5-6, where the parameter $K(2\mu + \lambda)$ is seen to affect the shape of pressure propagation (important at early times) while α regulates the magnitude of the pressure profile (dominant at later times).

It should be emphasized that this characteristic time is for fluid or pressure equilibration following the step increase in pressure at the tip. It does not describe the uptake time introduced in Chapter 4, which characterized macromolecular transport. This will be explored in Chapter 6. Aside from fluid pressure equilibration time, there exists a characteristic time for injected fluid to saturate the injection length (T_f), which would be equal to that for molecular transport if the molecules were much smaller than the characteristic pore size within the interstitium. This is the time it would take for a packet of fluid to travel the characteristic length α :

$$v = \frac{dx}{dt} = -\frac{K}{\varepsilon} \nabla P^* \approx \frac{\sqrt{K\beta}}{\varepsilon} P_o^* e^{-x/\alpha}$$

$$T_f = \int_0^{\alpha} \frac{dx}{v} \approx \frac{\varepsilon}{\beta P_o^*} \quad (5.27)$$

Thus, the pressure distribution within a tissue following an interstitial injection can be quantitatively described by the simplified theoretical framework presented. This allows a new dimension to our understanding of lymphatic function and offers an insightful and quantitative method for simultaneously examining three key constituents of interstitial-lymphatic fluid balance *in situ* - swelling mechanics, interstitial transport, and lymphatic drainage. Given that the response of the tissue is relatively sensitive to the controlling parameters, this model can be used to evaluate different types of edema, examine the effects of relevant drugs (such as those which alter microvascular permeability or the extracellular matrix), or test clinical procedures such as tissue grafting on the various aspects of tissue fluid balance, for example.

5.4.1 Hydraulic conductivity

The validity of the estimates for hydraulic conductivity and tissue elasticity can be discussed on the basis of the vast amount of previous work to estimate these parameters. These are summarized in a review (Levick 1987). Hydraulic conductivity has been measured in many tissues in a variety of ways and, due to method and technique differences, a broad range of values have been reported. Swabb *et al* reported a value of 5×10^{-9} cm²/sec/mm Hg for rat skin (Swabb *et al* 1974), and Bert and Reed found flow

conductivities in rat dermis between $3-8 \times 10^{-9} \text{ cm}^2/\text{sec}/\text{mm Hg}$ (1995). The discrepancy of over two orders of magnitude between their values and those presented here can be attributed to the fact that these *in vitro* estimates resulted from pressure-flow measurements across excised tissue. We estimated K in tail skin *in situ* and at maximal swelling. Since K depends strongly on hydration (Levick 1987, Bert and Reed 1995, Bert 1970), both because of frictional drag forces as well as electrical charge density (Aukland and Reed 1993), it is expected that a tissue undergoing compression would yield lower values of K than if it were swollen by hydrostatic pressure instead. In fact, as early as 1966 it was shown that changes in K of more than 5 orders of magnitude could result from various swelling conditions (Guyton *et al* 1966). This is also seen from the confined compression tests, in which K was estimated as $6 \pm 2 \times 10^{-7} \text{ cm}^2/\text{sec}/\text{mm Hg}$, or approximately half the value found *in situ*. For the *in situ* model, hydration was accounted for and within the infusion region, where pressure was higher than physiological values, the intrinsic K was found to be approximately constant. This K represents an effective, bulk-averaged value for normal tail skin which is acutely and temporarily swollen by an imposed IFP.

5.4.2 Tissue elasticity

Tissue elasticity is commonly reported as compliance, or the slope of IFV vs. IFP. The first measurements were made by Guyton (1965), who showed the shape of the compliance curves in general: linear at low pressures (in the range of negative to slightly above normal), nearly infinite at intermediate pressures (approximately 5-7 mm Hg), and linear again at even higher pressures. Since then, numerous measurements of tissue compliance have verified this trend (although with lower pressure values using more accurate techniques) and are summarized in a recent review (Aukland and Reed 1993). For our purposes we assumed the compliance was linear within the characteristic length (region of the imposed pressure profile) of the tail skin. In the limit of small strain, Equation 5.5 can be scaled to the approximation $\Delta IFP \approx (2\mu + \lambda)\Delta IFV$. In this regard, the compliance of the tail skin in the range of 10-50 mm Hg could be estimated as the inverse of elasticity, or 0.91 ml/100 g wet tissue/mm Hg. Although the compliance of mouse tail skin has not been reported to date, Aarli and Aukland estimated the compliance of rat tail skin between 0.1 and 0.34 ml/100 g wet tissue/mm Hg. It should be noted first that theirs was a radial compliance rather than axial, so that hoop stress would tend to effectively decrease this net radial compliance; second, that rat tail skin is much more “scaly” and thus less compliant than that of the nude mouse; and finally, that they did not account for the bone volume in

their calculation of ΔIFV , which would result in an underestimation of compliance. Other estimates of skin compliance include 5.4 ml/100 g wet tissue/mm Hg during dehydration of rat skin (Wiig and Reed 1981), 7.5 ml/100 g wet tissue/mm Hg in hydration of dog skin (Brace *et al* 1979), and 3.2 ml/100 g wet tissue/mm Hg in cat skin (Wiig and Reed 1985). Discrepancies are most likely due to the method of measurement, location of skin and species, and state of the animal or tissue (i.e. *post mortem* or *in vitro*).

Furthermore, there are documented differences between tissue elasticity measured *in situ* with that measured *in vitro*. For example, the stress-strain relationships in skin were crudely measured before and after a tattoo grafting operation and it was found that for all levels of unidirectional tension, the modulus was lower *in situ* than in the excised specimen (Kenedi *et al* 1965). These researchers also showed nonlinear stress-strain relationships for human skin in uniaxial tension, whose slopes increase with tensile strain until the failure point is reached. This is presumably due to the stretching of the randomly intertwined collagen bundles. At low strains, the collagen fibers begin to straighten in the direction of the load, and as strain increases, these fiber bundles become more oriented and more closely packed (resulting in an increasing modulus) until the failure or breakage point is reached (Markenscoff and Yannas 1979). This has also been shown histologically (Craik and McNeil 1965). In light of this, we would expect low tensile strains to yield a smaller elastic modulus than equivalent compressive strains, which would pack the matrix fibers closer together and therefore resist deformation more. The fact that charged components of the ECM are also concentrated during compression, increasing the Donnan forces within the interstitium, would also contribute to this effect. Also, higher strains were used in the confined compression tests than those which resulted from the interstitial infusion.

5.4.3 Net lymphatic conductance

Lymphatic conductance has been considered in this study as a lumped parameter, combining the resistances to fluid drainage posed by the initial lymphatic structures with the systemic drainage capacity rather than a true permeability of a lymphatic capillary. In relation to interstitial resistance, this parameter is useful in understanding the overall tissue fluid equilibrium, and as such, the few literature estimates of local (Starling) lymphatic fluid conductance (Abernathy *et al* 1995, Hendriksen 1985) are not relevant for comparison purposes. The lymphatic conductance presented here is meaningful in examinations of different physiological and pathological conditions in the tail model, *e.g.* in lymphedema, tissue grafting, or drug effects. These will be explored in Chapter 7.

5.4.4 Distribution of hydration and fluid velocity

From the stress-strain relationship of Equation 5.2, the distributions of fluid velocity and strain or hydration can also be evaluated from the pressure measurements. Starting with Darcy's Law (Equation 5.6),

$$\phi \left(\bar{v} - \frac{\partial \bar{u}}{\partial t} \right) = -K \frac{\partial P^*}{\partial x}$$

At steady state, $\frac{\partial \bar{u}}{\partial t} = 0$ and $P_{ss}^* = P_o^* e^{-x/\alpha}$. Strain is related to hydration by

$$e = \nabla \cdot \bar{u} = \frac{\delta V_T}{V_{T_o}} \cong \frac{V_T - V_{T_o}}{V_{T_o}} = \frac{\phi - \phi_o}{1 - \phi}, \quad (5.28)$$

and since $P^* = (2\mu + \lambda)e$, hydration is related to pressure by

$$\phi = \frac{P^* + \phi_o(2\mu + \lambda)}{P^* + (2\mu + \lambda)}. \quad (5.29)$$

Therefore, the steady-state swelling distribution is

$$\phi_{ss}(x) = \frac{P_o^* e^{-x/\alpha} + \phi_o(2\mu + \lambda)}{P_o^* e^{-x/\alpha} + (2\mu + \lambda)} \quad (5.30)$$

and the steady-state bulk velocity profile is

$$\bar{v}_{ss}(x) = -\frac{K}{\phi_{ss}} \frac{\partial P_{ss}^*}{\partial x} = \frac{P_o^* \sqrt{\beta K} e^{-x/\alpha} (P_o^* e^{-x/\alpha} + (2\mu + \lambda))}{P_o^* e^{-x/\alpha} + \phi_o(2\mu + \lambda)}. \quad (5.31)$$

5.4.5. Assumptions and limitations

The parameters were initially kept as constants because of the assumption that within the characteristic length of the infusion, swelling was maximal and changes in the parameters were small compared to their values. In this way they represented bulk-averaged quantities in this region, where all of our measurements were made. The assumption of constant K was discussed in Section 5.2.1. It is also possible that the tissue fluid volume fraction, or state of hydration, can affect lymphatic uptake. Lymphatic capillaries are thin-walled and usually without a basement membrane, consisting of a monolayer of overlapping endothelial cells whose intercellular gaps comprise channels for lymph formation. To preserve integrity, therefore, they rely on anchoring filaments which secure the endothelium to structural components of the interstitial matrix (Leak 1976, Castenholz *et al* 1991a, Gerli *et al* 1991, Aukland and Reed 1993); as the interstitium fills with excess fluid, the matrix swells, exerting tension on the anchoring filaments which pull open the pores of the lymphatic capillaries to effectively increase their permeability. This concept has been supported by the observation that changes in IFV alone (without change in IFP) cause changes in lymphatic drainage (Hogan and Unthank 1986, Aarli *et al* 1991a). In the analysis presented here, the parameters governing fluid distribution are considered averaged over the entire pressure gradient imposed (again, where swelling is assumed maximal), and small variations in lymphatic permeability due to changes in hydration should be negligible compared to the overall average. Furthermore, it is assumed that the applied pressure gradient is much larger than normal physiological pressure oscillations (Aukland and Reed 1993, Bollinger 1993, Hogan and Unthank 1986, Zaugg-Vesti *et al* 1993) and thus dominates forces driving lymphatic uptake. In this case, the porosity or permeability of the initial lymphatics would be maximal and thus constant throughout the bulk of the applied pressure gradient (where most of the fluid uptake occurs). This assumption is verified by the linear data shown in Figures 5-3 and 5-4.

5.5 Alternative methods

The experimental methods presented up to this point have sought to verify the theoretical framework and yield estimates of three parameters which control the mechanical aspects of tissue fluid balance. It would be desirable to utilize this model for parameter approximations in various other states of tissue fluid balance, such as the effects of relevant drugs, lymphedema, enhanced microvascular permeability, or alteration of the extracellular matrix. The micropipette techniques presented here, however, are difficult and tedious, causing obstacles for routine use. This section describes an alternative method for estimating the parameters K and β using fluorescence microscopy rather than micropipettes. Although it is an approximate method, based on measurements of characteristic lengths rather than pressure profiles, it is much simpler experimentally and still sensitive enough to measure gross changes in the parameters during lymphedema and other conditions (which will be explored in Chapter 7).

5.5.1 Theory

According to Equation 5.20, the IFP profile at steady-state decays exponentially with the ratio $\sqrt{K/\beta}$. This is also shown by the steady-state IFP measurements in Figure 5-3. For any given pressure P_L^* , therefore, the relationship between the infusion pressure P_o^* and length L at which $\bar{v} = (-K/\varepsilon)\nabla P^* = \sqrt{\beta K} P_o^* e^{-x/\alpha}$ is given by

$$L = -\alpha \ln \frac{P_L^*}{P_o^*} = \alpha (\ln P_o^* - \ln P_L^*)$$

or

$$\ln P_o^* = \frac{1}{\alpha} L + \ln P_L^* \quad (5.32)$$

Theoretically, we could estimate the ratio α by simply measuring a steady-state “length” associated with a specific P_L^* as a function of infusion pressure. We would define the length L as that length in which P_L^*/P_o^* is small enough for solute convection to be negligible. The exact value of P_L^* need not be defined as long as consistency is maintained with each measurement and the times of measurement are not too long - *i.e.* when molecular diffusion might affect the visible length. As we shall see, this is indeed feasible

and yields approximate values for α which are consistent with those found from IFP profiles. First of all, the characteristic time for infused fluid to saturate this region is shown by Equation 5.30 to be on the order of $\frac{\epsilon}{\beta P_o^*}$, or less than 14 minutes, according to the parameter estimates from Table 5.1 (and assuming ϵ is less than 1). Fluid is not visible, however, but rather the fluorescently labeled molecules which convect with the fluid. The characteristic time for solute transport in the tissue will depend on tissue-solute interactions, such as size exclusion, but the characteristic *length* should be the same as that for fluid transport if molecular diffusion is neglected⁴.

5.5.2 Methods

To test this idea, five mice were infused (at constant pressure) with a solution containing FITC-Dextran 2M (Sigma) according to the methods outlined in Chapter 3. Infusion pressure was increased every 30 minutes from 45 to 60 cm water (33-44 mm Hg) and images acquired with the Hamamatsu CCD camera for on-line analysis (again, refer to Chapter 3 for details). Average pixel intensities were recorded for 10-20 vertical rectangles, each spanning an axial length of 300 micrometers. Characteristic lengths were determined by finding the steady-state “front” - i.e. the vertical rectangle which had the greatest intensity change between its end intensities. This estimate was used rather than a mean

distance (i.e. $\bar{x} = \frac{\int_0^{\infty} \theta x dx}{\int_0^{\infty} \theta dx}$, where θ is the normalized intensity as defined in Equation

3.1) because of anticipated gradients in the concentration or intensity profiles within the characteristic length. In other words, a mean distance would refer to the solute transport, while the “front” would more accurately represent the characteristic length of the infusion by ignoring solute concentration gradients within the injection region. These two distances would only be equivalent if the solute can be approximated as a marker for fluid movement (i.e. infinitesimally small compared to the dimensions of the extracellular matrix “pores” and electrically neutral).

⁴ The diffusion coefficient of FITC-Dx 2M in water is on the order of 10^{-7} cm²/s using FRAP (unpublished data). Diffusion coefficients in tissue are about 3 times lower than those in water for molecules of this size range (Berk *et al*, 1993). Therefore diffusion will be negligible compared to convection when $x/v \ll x^2/D$. From Equations 5.6 and 5.20, $\bar{v} = (-K/\epsilon)\nabla P^* = \sqrt{\beta K P_o^*} e^{-x/\alpha}$, and according to Table 5.1, $\beta=4 \times 10^{-5}$ s⁻¹·mmHg⁻¹, $K=1.5 \times 10^{-6}$ cm²·s⁻¹·mmHg⁻¹, and $\alpha=0.2$ cm. Thus for $P_o^*=30$ mmHg, molecular diffusion is

5.5.3 Results and implications

Figure 5-8 below shows a typical progression of the moving front resulting from an infusion of FITC-Dx 2M (0.01 g/ml). As expected, the characteristic times required for the establishment of the characteristic length (i.e. for fluid to saturate the infusion region) is on the order of 10 minutes. Thus, a 30-minute period was allowed to confirm the estimation of the characteristic length.

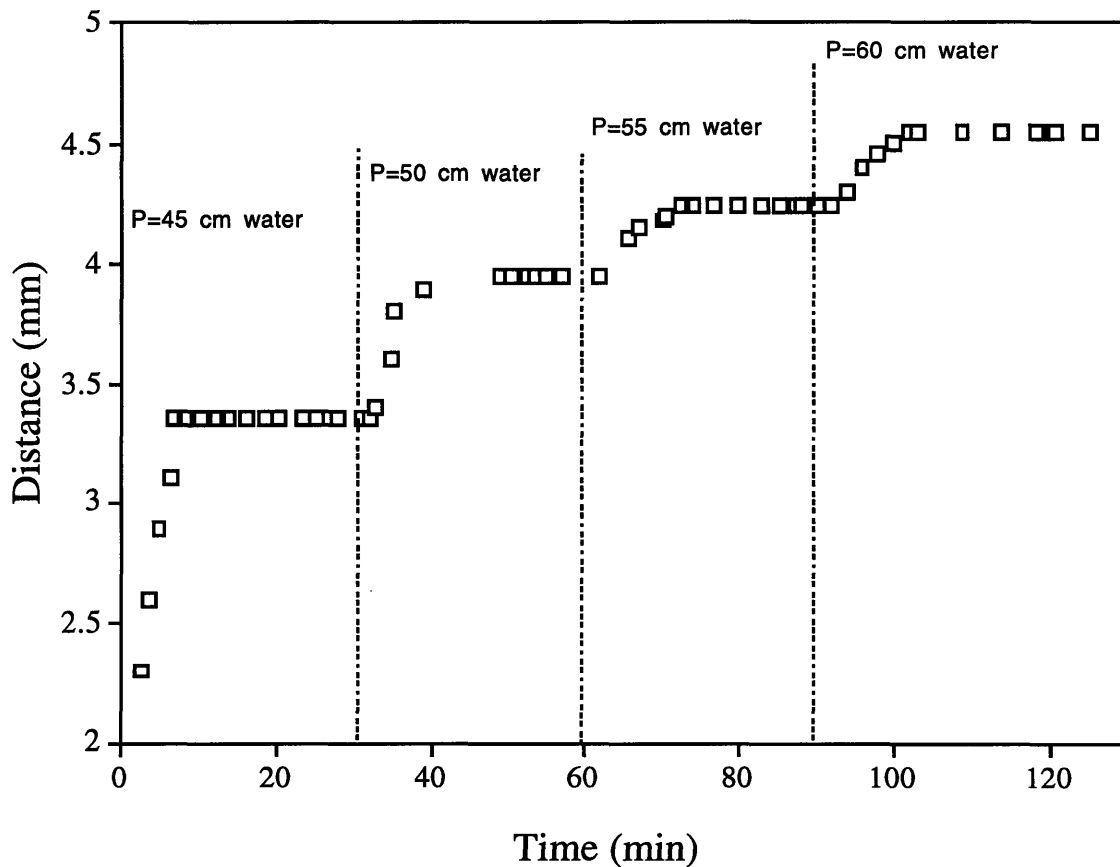


Figure 5-8. Position of the “leading edge” of fluorescent solute, or “moving front”, with time. At each 30-minute interval, infusion pressure was increased step-wise by 5 cm water (3.7 mm Hg) which is indicated by the vertical dotted lines. The establishment of approximate steady-state conditions can be seen before each successive perturbation.

negligible compared to convection for distances less than 2 cm. This is well within the characteristic infusion length of 2 mm and the region of measurements.

If this front length L is plotted against $\ln(P_o^*)$, then L/α is the slope and $\ln(P_o^*)$ is the intercept. This is shown below in Figure 5-9, using the data from Figure 5-8 and assuming a baseline pressure of 9 mm Hg (see Table 5.1).

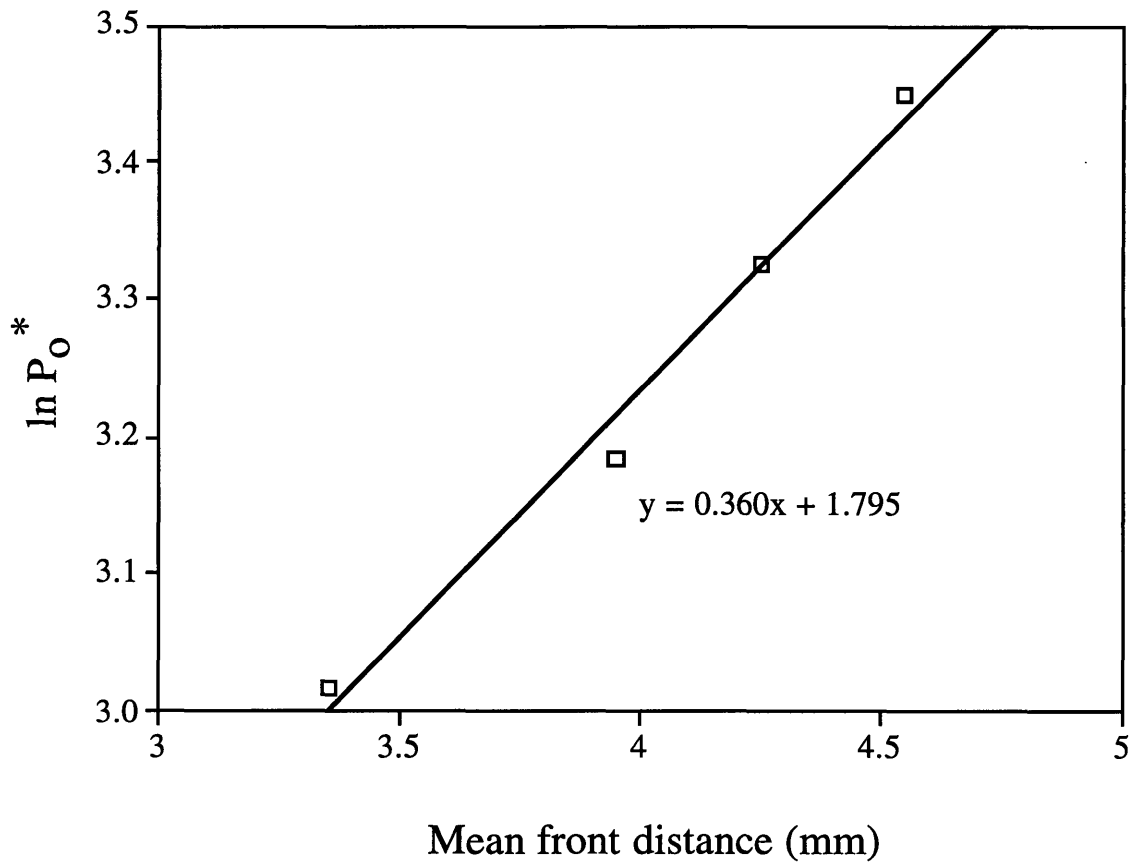


Figure 5-9. Length of infusion, as measured by the saturation of the interstitium with fluorescent tracer (FITC-Dx 2M), vs. $\ln(P_o^*)$. As shown, this particular data yielded a slope α of 2.8 mm.

This was performed in five mice, yielding an average value for α of 4.7 mm with a standard deviation of 1.9 mm. Together with the pressure-flow measurements (Equation 5.21 and Figure 5-4), the parameters K and β can thus be easily estimated from a simple two-hour experiment. From five experiments, these parameters were calculated to be $2 \pm 1 \times 10^{-6} \text{ cm}^2 \cdot \text{s}^{-1} \cdot \text{mmHg}^{-1}$ (mean \pm s.d.) for K and $7 \pm 5 \times 10^{-6} \text{ s}^{-1} \cdot \text{mmHg}^{-1}$ for β . This can be compared to estimates from the more precise micropipette technique of $1.5 \pm 0.4 \times 10^{-6} \text{ cm}^2 \cdot \text{s}^{-1} \cdot \text{mmHg}^{-1}$ and $4 \pm 2 \times 10^{-5} \text{ s}^{-1} \cdot \text{mmHg}^{-1}$, respectively. Although this alternative method results in approximate values of α (i.e. higher standard deviations than that obtained with the micropipette measurements of the steady-state IFP profile), it is much simpler and relevant for acquiring bulk estimates of the tissue parameters K and β for a variety of conditions. The alternative method will therefore be used in Chapter 7, where modifications in tissue fluid balance are investigated.

5.6 Conclusions

The model presented here provides an accurate description of convective interstitial-lymphatic fluid movement and represents a valuable tool to estimate tissue and lymphatic transport parameters *in situ*. Aside from interstitial fluid pressure, the model also describes the distributions of fluid velocity, tissue dilatation, and stress. The good agreement between the theory and experimental results, along with parameter estimations which are within physiological ranges, support the validity of the model and its assumptions. To study interstitial-lymphatic mechanics, however, more important than the actual values of these parameters are their functional relationships which can be investigated only by perturbing the system and measuring its transient and steady state responses. In this way, the model can be used to study the mechanisms of pathological conditions such as edema. Furthermore, this description of fluid transport provides the necessary foundation for studying convective macromolecular transport.

Chapter 6

Convective interstitial-lymphatic solute transport

6.1 Introduction

Useful and appropriate theoretical models require a careful balance between simplicity and relevance. The model must be accurate in describing a particular phenomenon while still maintaining the fundamental physics which govern the primary level of the problem. It is especially a challenge to model physiological systems because the underlying or microscale processes are usually poorly understood.

The goal in this section was to translate observations of convective phenomena into estimations of bulk transport hindrances *in situ*. In Chapter 4, fluorescently labeled solute was used to indicate fluid transport within the lymphatic vessels. Here, the focus is shifted from transport of the fluid within the vessels to the interstitial transport of the solute. Interstitial solute movement can be observed by fluorescence intensity measurements near the injection. If the intensity is linearly proportional to concentration, the normalized intensity profiles would be equivalent to interstitial solute concentration profiles. Typical profiles which motivated this work are shown in Figure 6-1. In solution, these intensities were well within the linear intensity-concentration range but could not be calibrated because it was not possible to measure tissue concentrations.

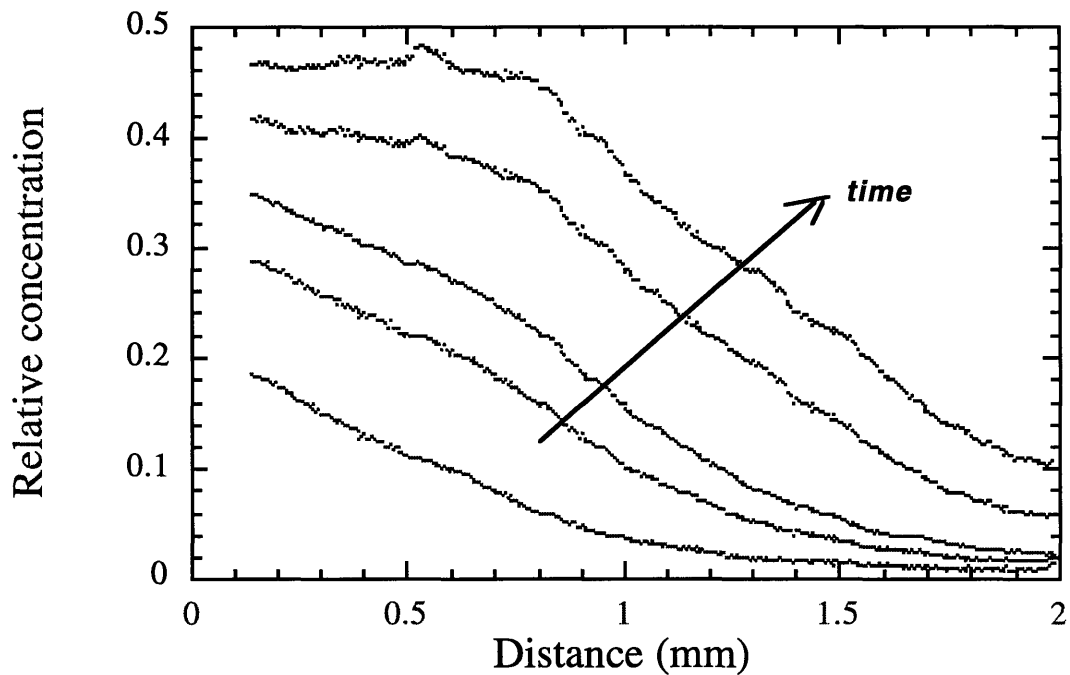


Figure 6-1. Spatial profiles of FITC-Dextran 2M at 2.5, 4.2, 5, 8, and 10 minutes following injection.

Direct observation suggests that different molecules convect through tissue at different rates and in different ways. For example, larger molecules may convect faster and with a steeper concentration gradient than smaller molecules. Along with fluid convection, various factors were considered which could give rise to differences in spatial and temporal concentration profiles. For example, size partitioning would result in larger available volume fractions for smaller molecules, yielding slower net velocities and increased dispersivity.

It should be emphasized that the goal here was not to examine the microscopic interactions between the solute and the tissue which give rise to interstitial or lymphatic transport behavior but simply to measure or characterize their macroscopic effects. This would provide not only a much needed quantitative *in situ* model for convective transport of macromolecules, but also a tool for exploring and optimizing drug delivery both for targeting the lymph nodes as well as any drugs which are injected interstitially, such as vaccines or intratumoral infusions.

6.2 Background

There are several ways to describe the distinguishing features of the interstitial concentration profiles exemplified in Figure 6-1, depending on the information desired. The following sections will discuss some of the theoretical considerations, their implications, and their relevance in characterizing key aspects of convective transport of macromolecules following an interstitial injection.

The general problem in consideration arose from the RTD studies of Chapter 4. It was observed that although the net velocity in the superficial network was independent of injection pressure (Figure 4-2), there was a characteristic uptake time which did depend on the injection pressure. This was seen by extrapolating the relationship between distance and mean residence time (MRT), which was measured within the lymphatic capillaries, to an arbitrary distance close to the injection. At higher pressures, this characteristic time was shorter and it took less time for the lymphatic network to become stained.

First, then, the relationship between injection pressure and a vaguely-defined characteristic uptake time T was examined to obtain a zero-order understanding of the phenomenon. Following the procedures of Section 4.3.1, T was calculated as the extrapolation of x vs. MRT (downstream in the lymphatic capillary network) to $x=0$ (defined at the needle tip). This was estimated for different injection pressures in four different mice, and the results are shown in Figure 6-2. This verified that the characteristic uptake time was indeed inversely proportional to the injection pressure. The next step was to determine the key determinants of macromolecular transport and uptake according to properties of the specific solute molecule itself, so that the model could fulfill its potential as a unique and powerful tool for observing and measuring convective macromolecular transport *in vivo*.

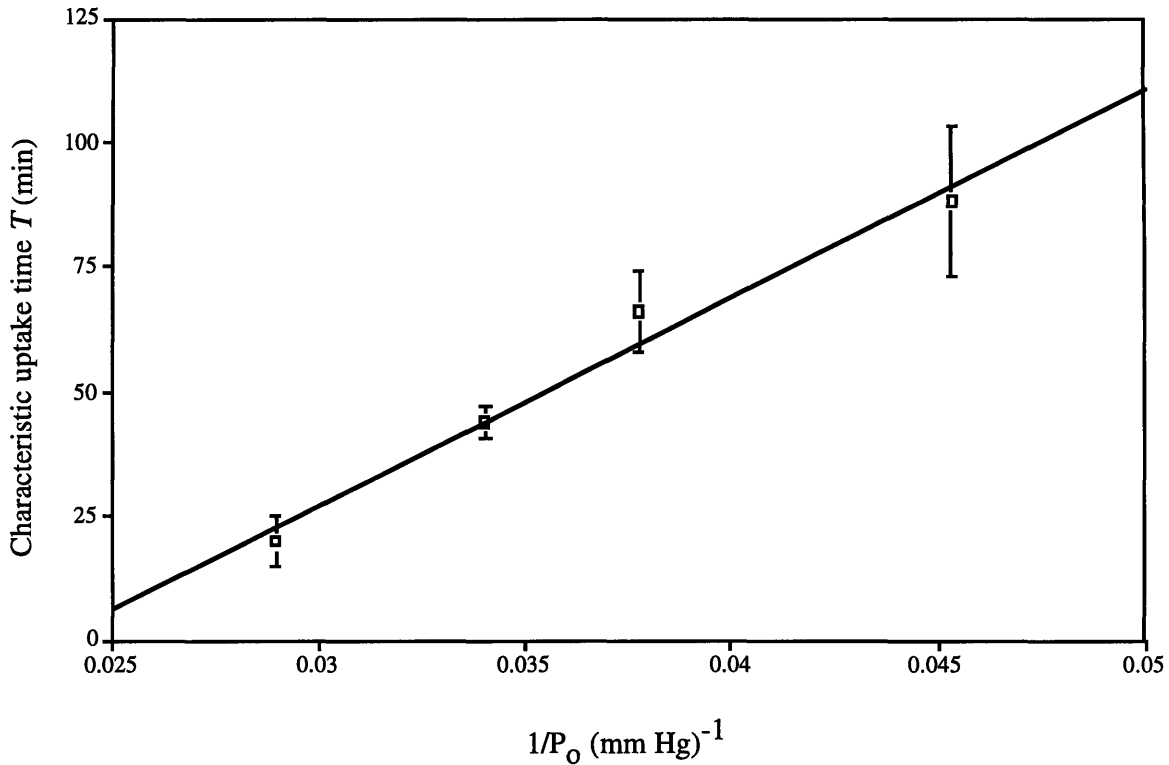


Figure 6-2. Relationship between injection pressure and “characteristic uptake time”, which was taken from plots of intralymphatic MRT vs. distance (see Figure 4-2) as the intercept or MRT at $x=0$.

6.3 Solute convection

Considering the most general case, solute convecting through tissue may undergo dispersion (with molecular and convective parts), convection, disappearance into the lymphatics, and adsorption onto the extracellular matrix or cells. The corresponding coefficients for each of these mechanisms are not constant (the fluid velocity and pressure profiles, on which they all depend, are exponential functions of distance), and thus a balance which includes all mechanisms may be overly complex compared to the experimental data to which it is applied. The goal here was to simply describe macroscopic concentration profiles which could be measured in the mouse tail.

At first, the concentration profiles were modeled using convective transport equations where dispersive effects were considered small compared to convection. A drag

coefficient ζ was utilized as a phenomenological coefficient to describe a bulk hindrance to interstitial convective transport ($\zeta = 1$ implies no hindrance). A reflection coefficient σ_L was defined in a similar way for bulk hindrance to lymphatic uptake (*i.e.* $\sigma_L=0$ when solute moves freely into the lymphatics with no translymphatic concentration difference, and $\sigma_L=1$ when the lymphatics are impermeable to the solute):

$$\frac{\partial C}{\partial t} + \nabla \cdot (\zeta \bar{v}_f C) + J_v(1 - \sigma_L) \frac{C}{\varepsilon} = 0 \quad (6.1)$$

where C is the total tissue (macroscale) concentration, \bar{v}_f is the bulk fluid velocity vector, ε is the fluid volume fraction, and J_v is the lymphatic drainage term (volume of fluid drained per tissue volume per time) as defined in Equation 5.12 ($J_v = \beta P^*$). In the one-dimensional system of Chapter 5, $v_{bulk} = \sqrt{\beta K} P^*$ where β = effective lymphatic conductance ($s^{-1} \cdot \text{mmHg}^{-1}$), K = effective hydraulic conductivity ($\text{cm}^2 \cdot \text{s}^{-1} \cdot \text{mmHg}^{-1}$), and P^* is the IFP in the tissue above baseline (mmHg).

If the pressure profile is assumed to be at steady state (*i.e.* $P^* = P_o^* e^{-\hat{x}}$, where $\hat{x} = x \sqrt{\beta / K}$) and we only consider one dimensional flow, then Equation 6.1 simplifies to:

$$\frac{\partial C}{\partial \hat{t}} + \zeta e^{-\hat{x}} \frac{\partial C}{\partial \hat{x}} + k_1 e^{-\hat{x}} C = 0 \quad (6.2)$$

where $\hat{t} = \beta P_o^* t$ and

$$k_1 = \left(\frac{(1 - \sigma_L)}{\varepsilon} - \zeta \right),$$

representing an effective decay rate coefficient.

Appropriate boundary conditions are those of a semi-infinite medium with zero initial concentration and constant flux at the boundary:

$$\begin{cases} \zeta \bar{v}_f C|_{\hat{x}=0} = \frac{Q_{inj} C_{inf}}{area} \\ C(x, 0) = 0 \end{cases} \quad (6.3a)$$

where C_{inj} = infusate concentration, $area$ = cross-sectional area of dermal/subcutaneous tissue tail (see Section 3.6 and Figures 3-3 and 3-9), and Q_{inf} = infusion flow rate. The latter was discussed in Chapter 5 and evaluated at steady state in Equation 5.21:

$$Q_{inf} = Q_{ss} = area \sqrt{\beta K P_o^*};$$

therefore,

$$C(0, t) = \frac{C_{inf}}{\zeta} \quad (6.3b)$$

Transforming into Laplace space, with $\tilde{C}(\hat{x}, s) = \mathcal{L}[C(\hat{x}, \hat{t})]$, Equation 6.2 becomes

$$\zeta e^{-\hat{x}} \frac{\partial \tilde{C}}{\partial \hat{x}} + (k_1 e^{-\hat{x}} + s) \tilde{C} = 0$$

with a transformed boundary condition of

$$\tilde{C}(0, s) = \frac{C_{inf}}{s \zeta}$$

This is easily solved:

$$\tilde{C} = \frac{C_{inf}}{s \zeta} \exp\left(\frac{-1}{\zeta} (k_1 \hat{x} + s(e^{\hat{x}} - 1))\right)$$

and inverted to give

$$C = \frac{C_{\text{inf}}}{\zeta} \exp\left(\frac{-k_1 \hat{x}}{\zeta}\right) h\left(\hat{t} - \frac{(e^{\hat{x}} - 1)}{\zeta}\right) \quad (6.4)$$

where h is the Heaviside step function. Upon examination, Equation 6.4 can account for spatial concentration decay within the interstitium but not their transient developments. This is expected, since the only time effect arises from the fluid movement (convection) and therefore the transient behavior of solute movement predicted by such a model is simply a step function. In other words, the concentration at any distance is instantly fixed as soon as the injected fluid has traveled that distance, and thus the last term in Equation 6.4 represents the time for fluid to travel a distance x at steady state.

It can also be readily seen from Equation 6.4 that a characteristic time associated with solute movement is linearly proportional to the inverse of u_1 , which is consistent with the original findings of Chapter 4 (see Figure 6-2), since $u_1 = \zeta \beta P_o^*$. Graphical representations of Equation 6.4 are shown in Figures 6-3 (a)-(b). The major limitation of this approach was, of course, that the spatial profiles did indeed show a strong transient development as shown by the different curves in Figure 6-1.

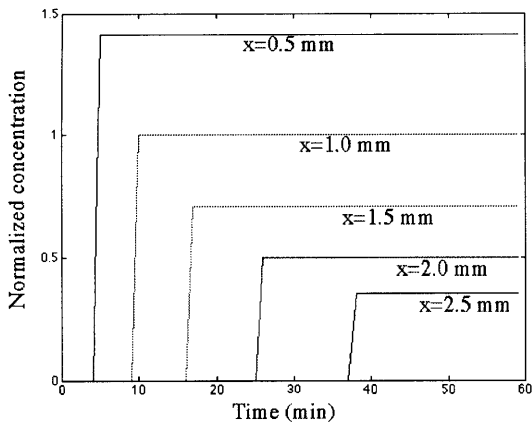
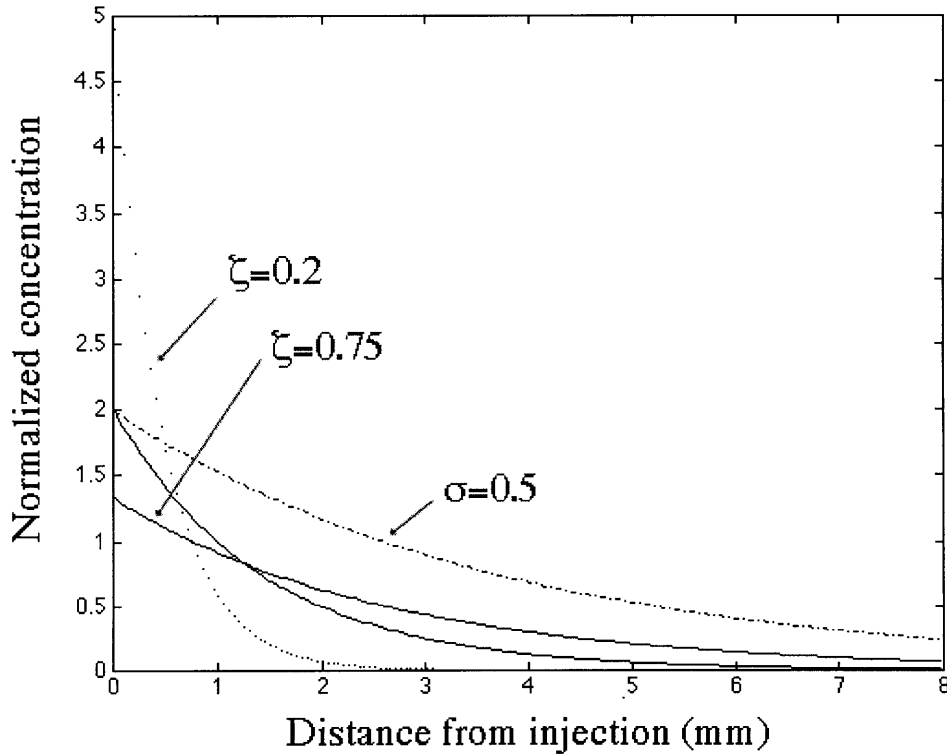


Figure 6-3 *Left* (a): Concentration vs. time for several distances as predicted by Eq. 6.4. Concentration is normalized to the infusate concentration, and the parameters σ_L , ζ , and ε were estimated as 0.1, 0.5, and 0.5, respectively. Values for β and K were taken from Table 5.1 ($4 \times 10^{-5} \text{ s}^{-1} \cdot \text{mmHg}^{-1}$ and $1.5 \times 10^{-4} \text{ mm}^2 \cdot \text{s}^{-1} \cdot \text{mmHg}^{-1}$). A was estimated as 0.6 mm^2 and P_o^* as 30 mm Hg . *Below* (b): Steady-state concentration profiles (normalized) and the effects of varying the parameters ζ , and σ_L . Unless otherwise noted, the parameters σ_L , ζ , and ε were fixed at 0.1, 0.5, and 0.5, respectively.



6.4 Convection and adsorption of solute

To phenomenologically describe the transient behavior of solute convection, a new model was considered using concepts of adsorption rather than convective drag:

$$\frac{\partial C}{\partial t} + \nabla \cdot (\bar{v}_f C) + J_v \frac{(1 - \sigma_L)}{\varepsilon} C + (1 - \varepsilon) \frac{\partial n}{\partial t} = 0 \quad (6.5)$$

where $(1 - \varepsilon)$ is the solid fraction and $\frac{\partial n}{\partial t}$ represents the net rate of solute “adsorption” to the solid or immobile fluid phases of the tissue (n [=] moles per volume solid). Such a model is commonly used to describe adsorption chromatography (Aris and Amundson, 1973, Watson and Jones 1984, DeSmedt and Wierenga 1979).

If linear adsorption is assumed, the adsorbed concentration can be expressed as:

$$\frac{\partial n}{\partial t} = \psi(\kappa C - n) \quad (6.6)$$

where κ is a partition coefficient and ψ is the linear adsorption coefficient [s^{-1}].

Consider some limiting cases: (1) ψ goes to infinity (instantaneous binding), (2) κ goes to zero (no binding), and (3) short times where $\kappa C \gg n$. Case (2) is equivalent to Equation 6.1, and so we will not consider that again here. Case (1) would imply that solute cannot move through the tissue at all because it adsorbs immediately. Case (3), however, is experimentally close to what we would expect from the measurements shown in Figure 6-1. It only neglects saturation effects and would thus be valid only for short times and/or small concentrations compared to “binding sites”. Because this model is applied here to phenomenologically describe solute dispersion and buildup, saturation-type effects will be neglected.

If $\kappa C \gg n$, the binding term defined in Eq. 6.6 becomes $\psi \kappa C$. In this way the parameters ψ and κ are indistinguishable in terms of experimental measurements. Therefore they are lumped into a new parameter here which will be called γ to represent the (insaturable) affinity for adsorption (incorporating the solid fraction $1 - \varepsilon$ as well; *i.e.* $\gamma = \psi \kappa (1 - \varepsilon)$). Then,

$$\frac{\partial C}{\partial t} + \nabla \cdot (\bar{\mathbf{v}}_f C) + \left(\frac{(1 - \sigma_L)}{\varepsilon} J_v + \gamma \right) C = 0. \quad (6.7)$$

Once again assuming steady-state fluid velocity, this can be written as

$$\frac{\partial C}{\partial \hat{t}} + e^{-\hat{x}} \frac{\partial C}{\partial \hat{x}} + (k_2 + k_3 e^{-\hat{x}}) C = 0, \quad (6.8)$$

where $\hat{x} = x\sqrt{\beta/K}$ and $\hat{t} = \beta P_o^*$ as before, $k_2 = \frac{\gamma}{\beta P_o^*}$, and $k_3 = \left(\frac{(1 - \sigma_L)}{\varepsilon} - 1 \right)$.

The constant-flux boundary condition is now $C(0, \hat{t}) = C_o = \varepsilon C_{\text{inf}}$, since any tissue “drag” or hindrance to convection is now modeled as adsorption/desorption phenomena.

In Laplace space, Equation 6.8 becomes:

$$e^{-\hat{x}} \frac{\partial \tilde{C}}{\partial \hat{x}} + (s + k_2 + k_3 e^{-\hat{x}}) \tilde{C} = 0$$

whose solution has a similar form to the previous case:

$$\tilde{C} = \frac{\varepsilon C_{\text{inf}}}{s} \exp\left(k_2(1 - e^{\hat{x}}) - k_3 \hat{x} + s(1 - e^{\hat{x}})\right)$$

Inverted, this yields a concentration profile

$$C = \varepsilon C_{\text{inf}} \exp\left(\left(k_2(1 - e^{\hat{x}}) - k_3 \hat{x}\right)h\left(\hat{t} - (e^{\hat{x}} - 1)\right)\right) \quad (6.9)$$

which still has a step dependence on time but whose spatial profiles have a bifunctional dependence on distance. Spatial profiles are shown below along with their dependence on the parameters γ , ε , and σ_L .

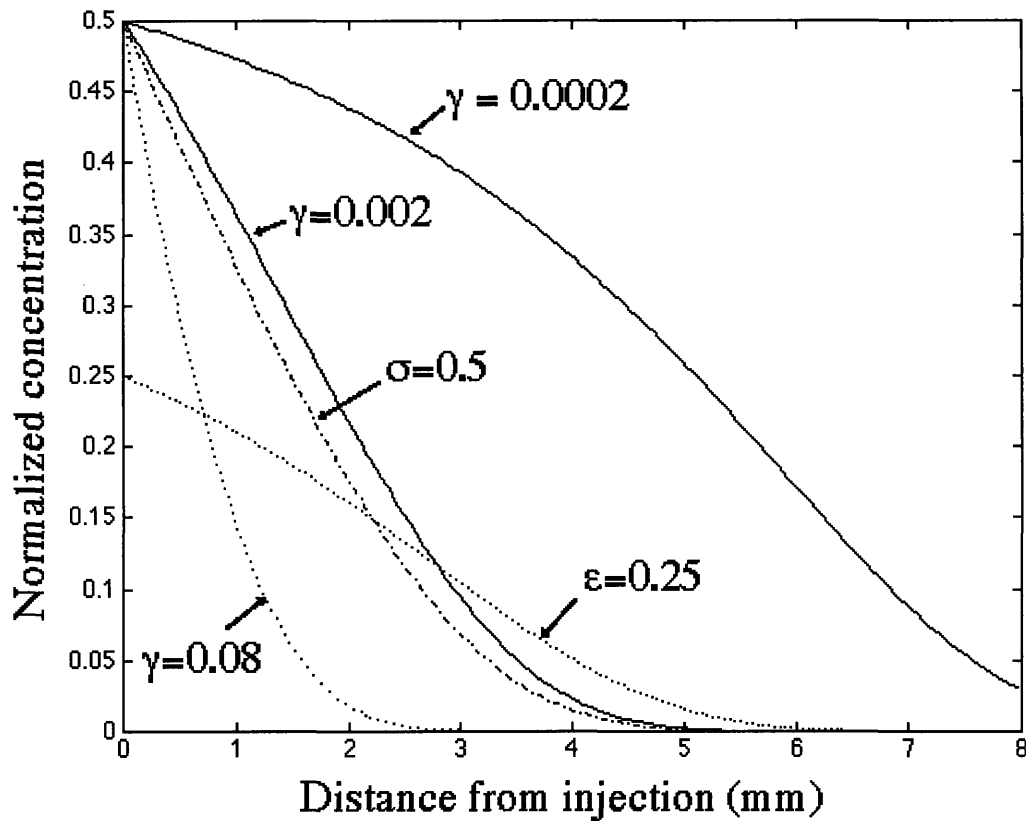


Figure 6-4. Spatial profiles described by Equation 6.9 using the same parameter values as before (see Figure 6-3 legend). Unless noted, values for ϵ , σ_L , and γ were taken as 0.5, 0.1, and 0.002 s^{-1} , respectively.

Therefore this model could account for the spatial dispersion of Figure 6-1, but not a transient dispersion. In other words, it attributes spatial concentration gradients to adsorption which is assumed insaturable. To validate the condition of insaturability, short observation times were required (i.e. the “plateau” seen in later times in Figure 6-1 could not be accounted for by this model).

6.5 Dispersive effects

Although a simple macroscale model was desired to highlight the dominant principles which governed solute transport through skin, it was clear that a second-order term - dispersivity - would be required to describe transient behavior of solute movement. Because the velocity field decayed within that characteristic region, a dispersivity which depended on velocity was necessary.

6.5.1 General theory

In the following analysis, the dermal or subcutaneous tissue of the tail is treated as a one-dimensional, semi-infinite, homogeneous porous media whose fluid balance resulting from an interstitial injection is described in Chapter 5. Solute which moves through the interstitium may have a different volume fraction (ϕ) in which to travel than that of the mobile bulk fluid (ϵ) due to partitioning. Furthermore, dispersive effects may arise from a number of factors including shape, charge, and molecular diffusivity of the solute as well as variations in the local (microscale) fluid velocity.

Caution must be exercised in defining an appropriate conservation equation for convective-dispersive solute transport through porous media. A phenomenological convective-diffusive representation, which is analogous to local or exact behavior in a well-defined system (*i.e.* Taylor 1953), can be expressed on a macroscopic scale by careful definition of the macroscopic variables¹. This was elegantly shown by Brenner (1980) using a method of moments. Here, lymphatic drainage is included as a sink term, R_v , in which solute 'disappears' or convects into the lymphatics along with the draining fluid. On a macroscopic scale, L (length scale of observation) $\gg 1$ (length scale of a hypothetical pore), and the bulk (measurable) solute concentration is governed by the following macroscale relation:

$$\frac{\partial \bar{C}}{\partial t} + \bar{\nabla} \cdot \bar{\mathbf{J}} + \bar{R}_v = 0 \quad (6.10)$$

¹ A bulk-averaged quantity \bar{P} is defined here as $\bar{P} = \frac{1}{V_o} \int P dV$, where P is the local variable and V_o is the total tissue unit volume.

where \bar{C} is the average (measurable) solute concentration in the tissue, \bar{R}_v represents solute drainage by the lymphatics, and \bar{J} is the net solute flux. This is given as

$$\bar{J} = \bar{U}^* \bar{C} - \underline{\underline{D}}^* \cdot \nabla \bar{C} \quad (6.11)$$

where \bar{U}^* and $\underline{\underline{D}}^*$ are the macroscale or apparent solute velocity vector and dispersion dyadic, respectively. They represent macroscopic phenomenological parameters which depend on a number of possible factors including the underlying (microscale) structure of the tissue and solute-tissue interactions.

6.5.2. Constitutive equations and variable definitions

It is desired to apply Equations 6.10 and 6.11 to the solute concentration profiles exemplified in Figure 6-1 (i.e. those resulting from an interstitial injection into the tail skin) in order to estimate bulk-average transport parameters. We will first focus on defining the variables for the tail injection system to determine a specific macrotransport conservation equation, then discuss assumptions and limiting cases in which the key parameters may be evaluated.

Combining Equations 6.10 and 6.11 for a one-dimensional system and omitting the overbars for simplicity, we have

$$\frac{\partial C}{\partial t} + \frac{\partial}{\partial x} (U^* C) - \frac{\partial}{\partial x} \left(D^* \frac{\partial C}{\partial x} \right) + R_v = 0 \quad (6.12)$$

with the boundary and initial conditions of the system either as constant surface concentration:

$$\left[\begin{array}{l} C(x, 0) = 0 \\ C(0, t) = C_o \\ \left. \frac{\partial C}{\partial x} \right|_{x \rightarrow \infty} = 0 \end{array} \right], \quad (6.13a)$$

where $C_o = C_{inj}(\varepsilon + (1-\varepsilon)\kappa)$, or with constant surface flux:

$$\left[\begin{array}{l} C(x,0) = 0 \\ \left[-D^* \frac{\partial C}{\partial x} + U^* C \right]_{x=0} = \frac{Q_{inf} C_{inf}}{A} \\ \left. \frac{\partial C}{\partial x} \right|_{x \rightarrow \infty} = 0 \end{array} \right] \quad (6.13b)$$

For simplicity, the first condition (constant concentration at $x=0$) will be considered in this section.

*Effective solute velocity U^**

A partitioning model is assumed to describe the mean solute velocity U^* . In this case, U^* differs from the average net fluid velocity ν^* (i.e. the Darcy velocity, or flow rate per total tissue area) by the porosity ε and a partition coefficient κ (Brenner 1980) according to:

$$U^* = \frac{\varepsilon \nu}{\varepsilon + (1-\varepsilon)\kappa} \quad (6.14)$$

Partitioning is somewhat ambiguously defined here, since the interstitial space is more like a polymer gel than a packed bed of porous beads for which this was intended. In the present case, the porosity represents the mobile fluid volume fraction in which all solute molecules can move, and the solid or partitioning phase represents other “pores” in the interstitium into which smaller molecules can diffuse. Then, the larger particles will have higher macroscale velocities than the smaller particles, a phenomenon also known as size-exclusion chromatography. The upper limit of mean solute velocity is reached when $\kappa=0$; i.e. when the solute has no partitioning into the non-mobile phase. In this case U^* will be equal to the true mean interstitial fluid velocity ν^* . Because the parameters ε and κ cannot be distinguished experimentally, the symbol ϕ will be used to represent the available

volume fraction for a given molecule; *i.e.* $\phi = \varepsilon + (1-\varepsilon)\kappa$. Therefore, $(1-\phi)$ is the excluded volume fraction and $\phi \geq \varepsilon$ accordingly.

In Chapter 5, it was established that at steady state, the Darcy-scale axial fluid velocity (not the pore fluid velocity v_{pore} of Equation 5.6 but instead $v_{\text{Darcy}} = \varepsilon \cdot v_{\text{pore}}$) decayed exponentially with distance:

$$v_{ss} = \sqrt{\beta K P_o} e^{-x/\alpha} \quad (6.15)$$

This decay of fluid velocity is essential to the analysis. The concentration profiles develop almost entirely within the characteristic injection length, yielding a variable dispersivity which should be governed by the fluid velocity at relatively small x and by molecular diffusion when $x \gg \alpha$. We cannot assume constant velocity even for small ranges of x close to the injection, because the profiles at any distance are governed by their dispersion history. Also, this fluid velocity affects the drainage and convective terms as well as the convective part of the dispersion term in Equation 6.12, since dispersivity is presumably a function of velocity.

It was shown in Section 5.4 that the characteristic time for fluid pressure to reach the steady state following injection, T_p , was on the order of $(\beta(2\mu + \lambda))^{-1}$, or roughly 10 minutes. By a simple scaling analysis of Equation 6.13, the characteristic time for the solute convection (T_p) is \bar{U}^{-1} , or roughly $(\phi(\varepsilon\beta P_o))^{-1}$. Then the ratio $T_p/T_p \sim \phi(2\mu + \lambda)/\varepsilon P_o$ will be assumed to be much greater than 1 for the experiments described and is verified by simultaneous measurements of IFP and solute movement at 1 mm from the injection, shown in Figure 6-5 below. This assumption allows us to consider the steady-state fluid velocity in observing solute concentration profiles, which, from Equation 6.14, leads to a mean solute velocity of

$$\begin{aligned} u^* &= \frac{\sqrt{\beta K P_o} \varepsilon}{\phi} e^{-x/\alpha} \\ &= u_o e^{-x/\alpha} \end{aligned} \quad (6.16)$$

Therefore, a steady-state fluid velocity can be assumed in modeling solute convection. Furthermore, by simply comparing mean solute velocities in the tail skin tissue, we can estimate the ratio ε/ϕ .

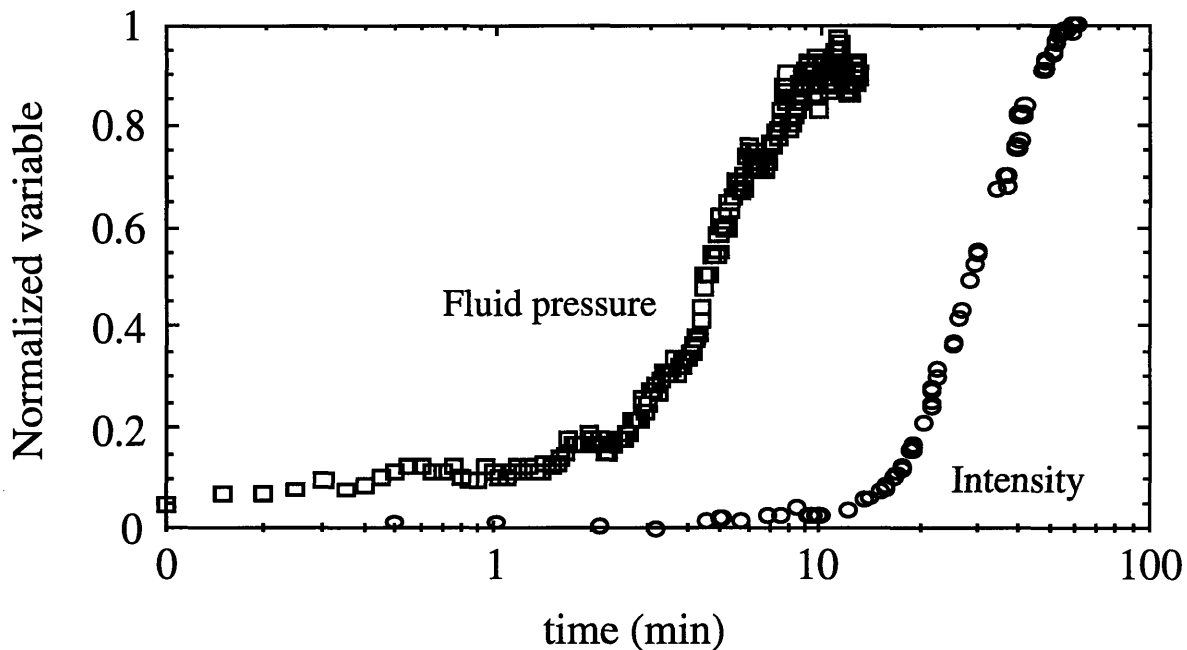


Figure 6-5. Transient development of interstitial fluid pressure (IFP) and solute concentration at a point approximately 3 mm from infusion.

Effective dispersivity

Dispersivity in porous media such as tissue is a phenomenological occurrence. It can arise from a number of factors including interactions between the solute and the interstitium (mechanical as well as electrical or chemical), immobile fluid and stagnant flow regions, and molecular diffusion. If a dominating mechanism can be identified and accurately described, then the dispersive term may not be needed. Such is the case for adsorption chromatography, which is often treated as we have above in Section 6.4.

When the interactions are more complex and when several mechanisms come into play, a generic dispersivity term serves the purpose of describing bulk macroscopic effects. However, because of the nature of its bulk definition, this term is sensitive to its

circumstances. For example, for flow in streams or long packed beds where $x \gg L$, dispersivity may increase asymptotically according to distance (Bear 1972):

$$D^* = aL \left(\frac{v}{\varepsilon} \right) (1 - e^{-bx/L}) + D^M \quad (6.17)$$

where a is the slope of x vs. D at $x=0$, b is a constant (<1), L is the characteristic length, and D^M is the molecular diffusivity. Furthermore, when $x/L < 200$, the exponential model for dispersivity predicts concentration profiles nearly equivalent to those predicted from a linear dispersion model (Yates 1992, Yates 1990):

$$D^* = a_2 \frac{v x}{\varepsilon L} + D^M. \quad (6.18)$$

A number of other relationships between dispersivity and space, time, or velocity have also been postulated (Logan 1996, Rubinstein and Mauri 1986, Auriault and Adler 1995, Basha and El-Habel 1993).

For the mouse tail model, solute dispersion is observed for relatively short distances and short times. Since the characteristic length for velocity decay is on the order of our observation length scale, it would seem appropriate to put the primary dependence of D^* on fluid velocity. Therefore, a linear relationship will be assumed:

$$D^* = D^C + D^M = Av_f + D^M \quad (6.19)$$

It will be further assumed that in the region of measurement, convective effects on dispersion dominate diffusive effects. Since the solute molecules in question are very large (2 to 2,000 kDa), this assumption infers that the Peclet number will be large within the region of measurement. Although this cannot be verified yet since there is no basis for estimating the convective dispersion parameter A , it can be confirmed *a posteriori*. Therefore,

$$\begin{aligned} D^* &\cong Av_f = A\sqrt{\beta K P_o^*} e^{-x/\alpha} \\ &= D_o e^{-x/\alpha} \end{aligned} \quad (6.20)$$

Lymphatic drainage

Finally, the lymphatic drainage term remains to be defined. Again assuming convection-dominated solute drainage, a first-order type decay is expected according to

$$R_v = J_v C \frac{(1 - \sigma_L)}{\varepsilon}, \quad (6.21)$$

where J_v is the fluid drainage into the lymphatics given by Eq. 5.12. At steady-state fluid pressure, this becomes

$$\begin{aligned} R_v &= \beta P_o^* e^{-x/\alpha} \frac{(1 - \sigma_L)}{\varepsilon} C \\ &= k_o e^{-x/\alpha} C. \end{aligned} \quad (6.22)$$

6.5.3 Conservation Equation

Combining Equations 6.12, 6.16, 6.20, and 6.22, the conservation equation for one-dimensional, convective-dispersive solute transport with lymphatic drainage becomes:

$$e^{x/\alpha} \frac{\partial C}{\partial t} - D_o \frac{\partial^2 C}{\partial x^2} + \left(\frac{D_o}{\alpha} + u_o \right) \frac{\partial C}{\partial x} + \left(k_o - \frac{u_o}{\alpha} \right) C = 0.$$

Using the dimensionless variables $\hat{x} = \frac{x}{\alpha}$ and $\hat{t} = \frac{\beta P_o^* \varepsilon}{\phi} t$, this can be written as

$$e^{\hat{x}} \frac{\partial C}{\partial \hat{t}} - D_o^* \frac{\partial^2 C}{\partial \hat{x}^2} + u_o^* \frac{\partial C}{\partial \hat{x}} + k_o^* C = 0 \quad (6.23)$$

where D_o^* , u_o^* , and k_o^* are given by

$$D_o^* = A \frac{\phi}{\alpha \varepsilon}, \quad u_o^* = A \frac{\phi}{\alpha \varepsilon} + 1 = D_o^* + 1, \quad \text{and} \quad k_o^* = \frac{\phi(1 - \sigma_L)}{\varepsilon^2} - 1,$$

representing the bulk-effective equivalents of the parameters (diffusivity, mean solute velocity, and first-order decay constant, respectively). Note that the parameters ϕ and σ_L are

always seen in conjunction with ε and so only the ratios ϕ/ε and $(1-\sigma_L)/\varepsilon$ are important in determining solute transport behavior.

Simulations

Numerical solutions to Equation 6.23 with boundary conditions of constant surface concentration (Equation 6.13a) were generated to investigate the effects that each solute transport parameter (A , ϕ/ε , and $(1-\sigma_L)/\varepsilon$) had on the bulk concentration profiles. These were performed using previously written code (Baxter, 1990) and are shown below in Figures 6-6 (a)-(g).

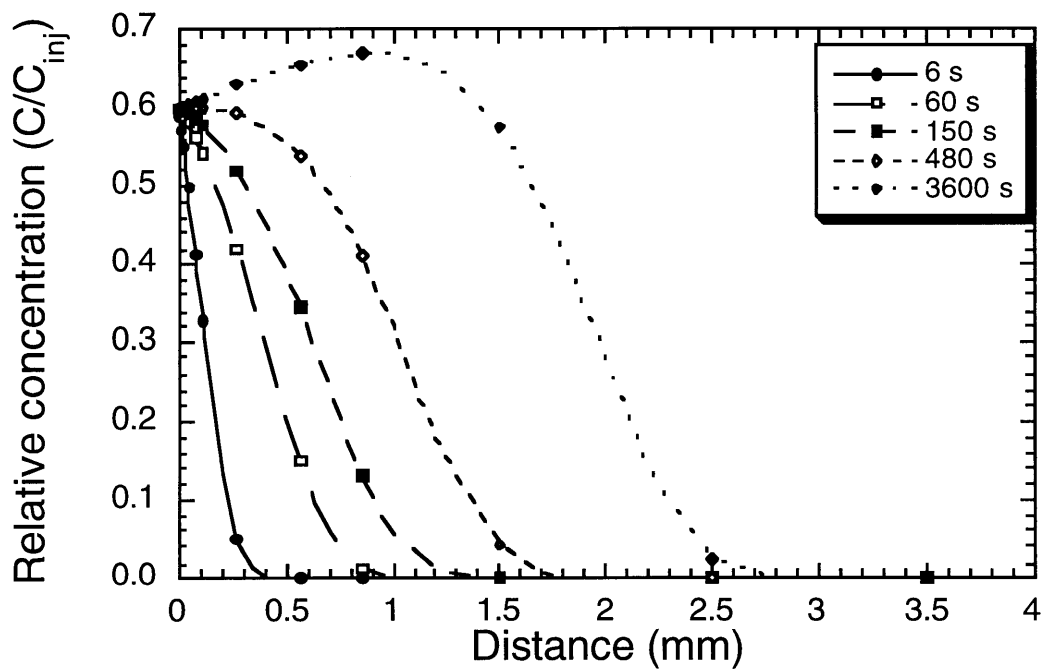


Figure 6-6. Graphical representations of Equation 6.23. (a) Baseline parameter values of $A=1.0$ mm, $\phi/\varepsilon=2$, and $(1-\sigma_L)/\varepsilon=3.3$. Fluid transport parameters β and K were assumed to be $4 \times 10^{-5} \text{ s}^{-1} \cdot \text{mmHg}^{-1}$ and $1.5 \times 10^{-4} \text{ mm}^2 \cdot \text{s}^{-1} \cdot \text{mmHg}^{-1}$, respectively, according to Table 5.1. Thus, $D_o^*=1.03$, $u_o^*=2.03$, and $k_o^*=5.67$. Concentration is normalized to the constant surface boundary condition; i.e. $C_{norm}=C/C_o=C/(C_{inj}\phi)$.

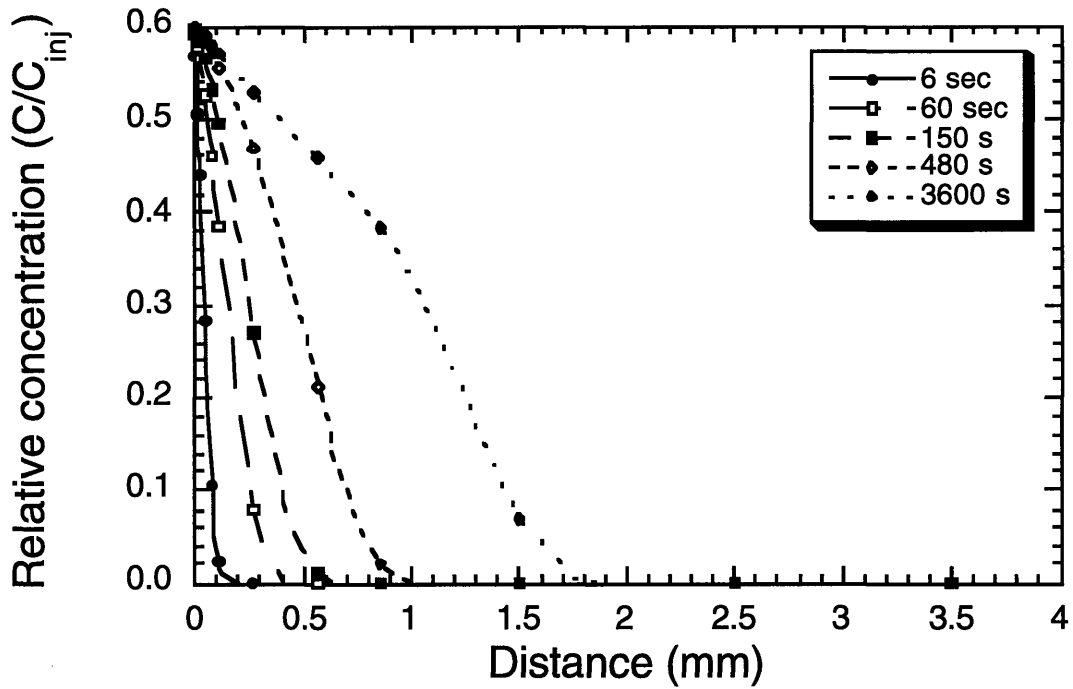


Figure 6-6 (b) Parameter values are the same as those given in Fig. 6-6(a) except A is decreased to a value of 0.1 mm. Thus, $D_o^*=0.103$, $u_o^*=1.103$, and $k_o^*=5.67$.

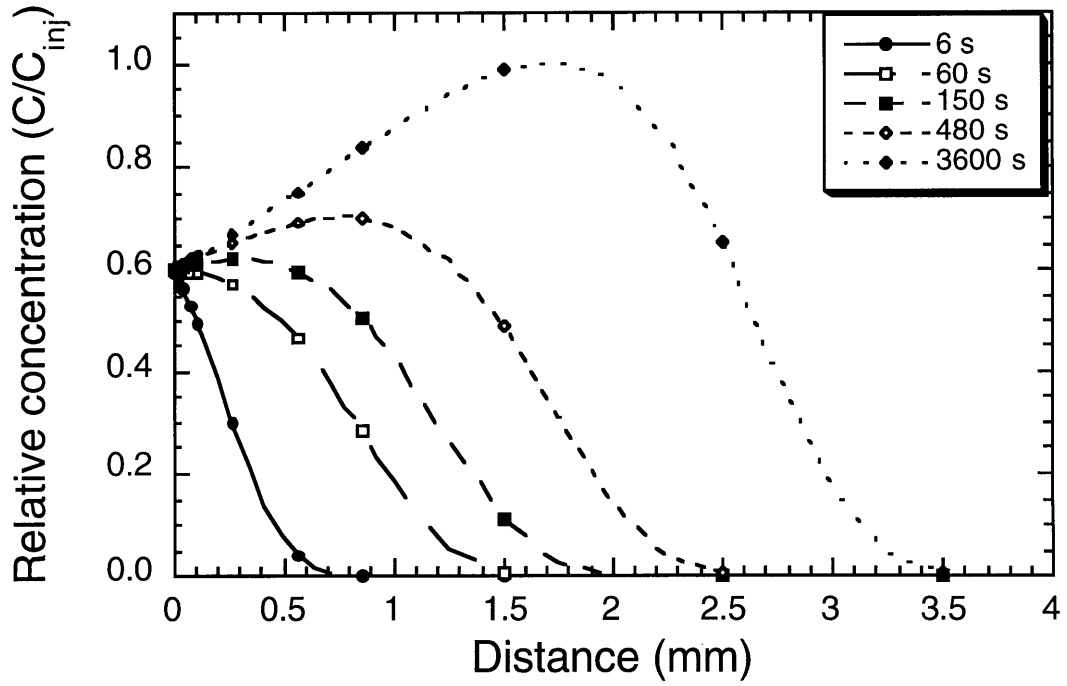


Figure 6-6 (c) Parameter values are the same as those given in Fig. 6-6 (a) except A is increased to a value of 5 mm. Thus, $D_o^*=5.165$, $u_o^*=6.165$, and $k_o^*=5.67$

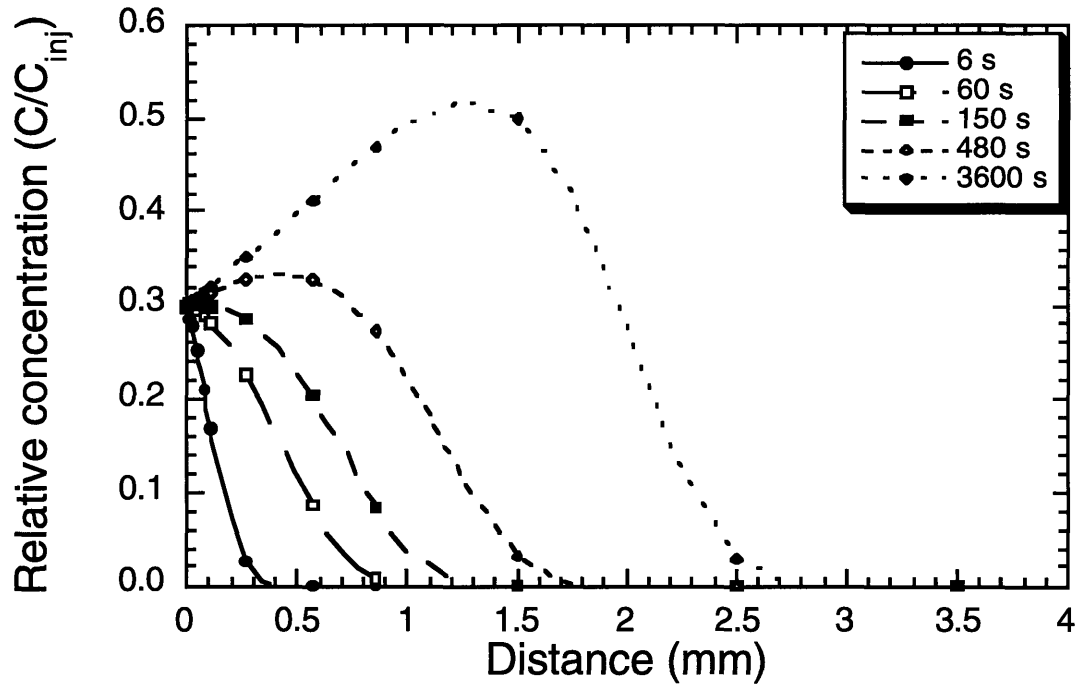


Figure 6-6 (d) Parameter values are the same as those given in Fig. 6-6(a) except ϕ/ε is increased to a value of 2.67. Thus, $D_o^*=1.377$, $u_o^*=2.377$, and $k_o^*=8.89$

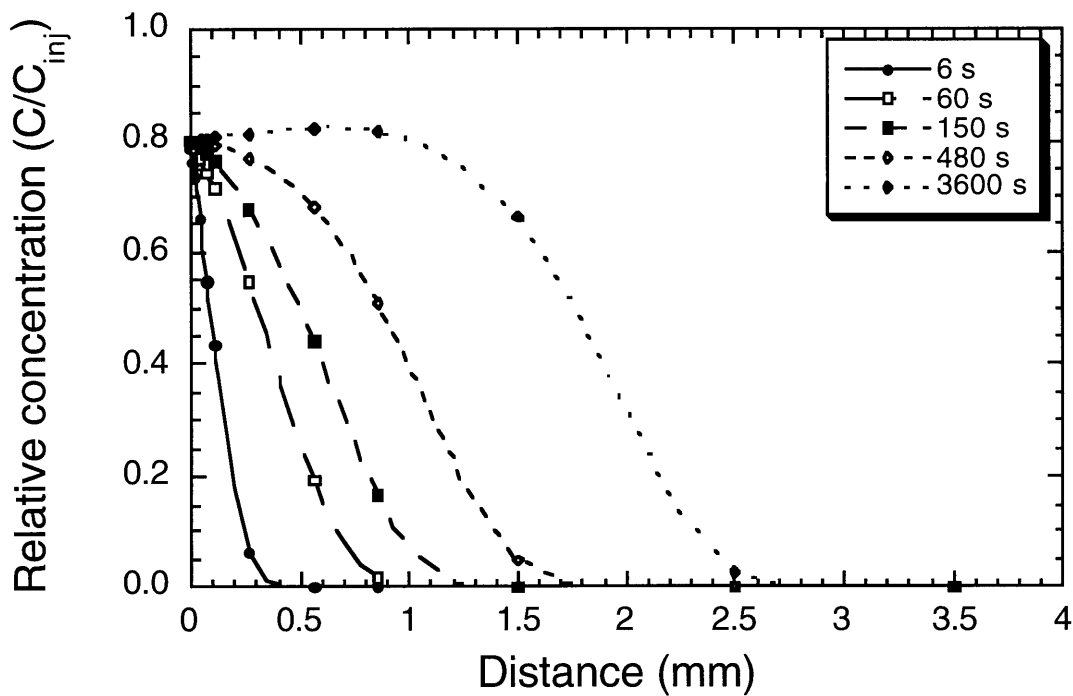


Figure 6-6 (e) Parameter values are the same as those given in Fig. 6-6(a) except ϕ/ε is decreased to a value of 1.0. Thus, $D_o^*=0.5165$, $u_o^*=1.5165$, and $k_o^*=2.33$

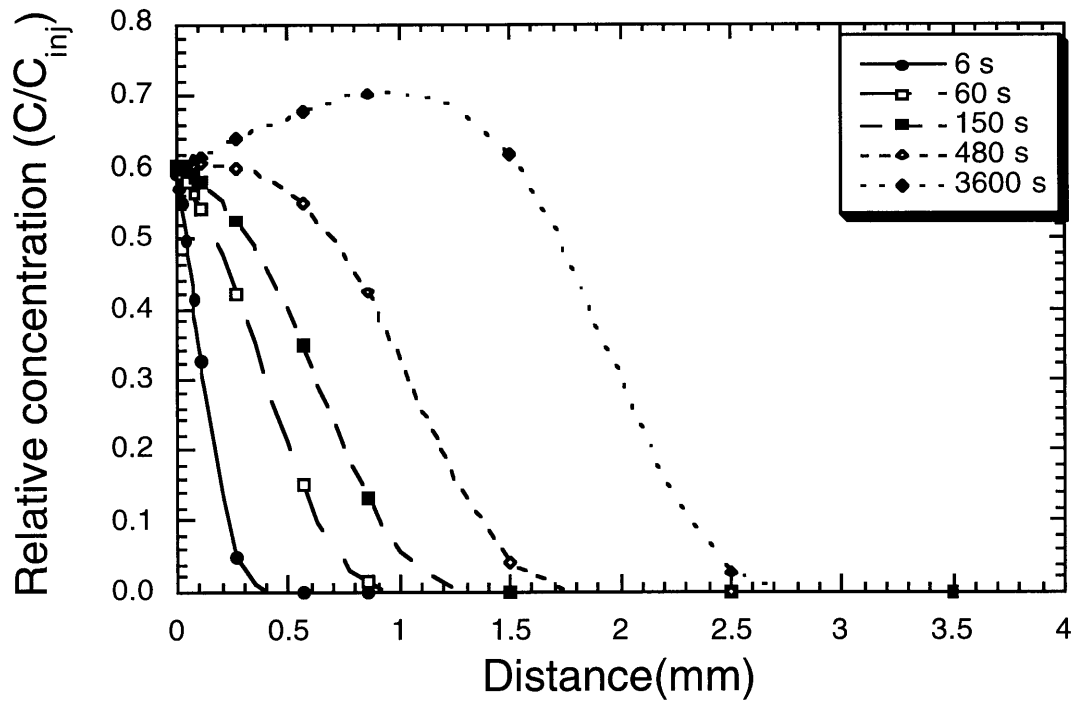


Figure 6-6 (f) Parameter values are the same as those given in Fig. 6-6(a) except σ_L is increased to a value of 0.1. Thus, $D_o^*=1.03$, $u_o^*=2.03$, and $k_o^*=5.00$

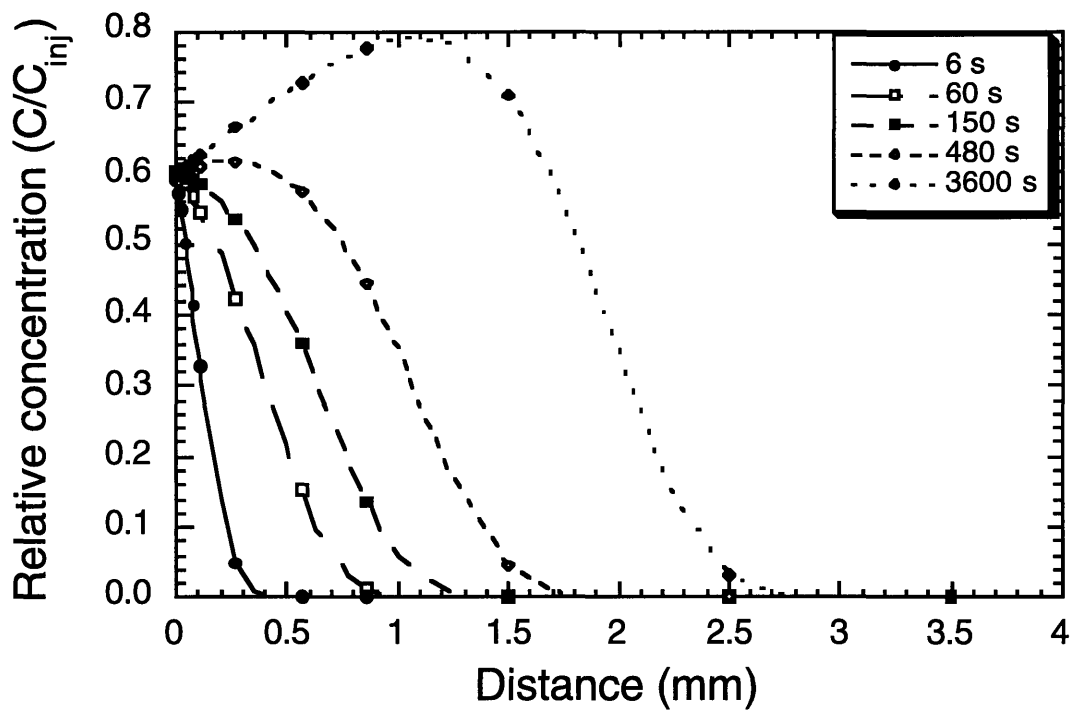


Figure 6-6 (g) Parameter values are the same as those given in Fig. 6-6(a) except σ_L is increased to a value of 0.3. Thus, $D_o^*=1.03$, $u_o^*=2.03$, and $k_o^*=3.67$.

Figures 6-6 (a)-(g) reveal the implications of the convective-dispersive model described by Equation 6.23. Figure 6-6(a) is regarded as the “baseline” plot while (b)-(g) show perturbations of each parameter about this baseline. The most prominent feature of the plots is the rise in normalized concentration ($C_{norm} = C/(C_{inj}\phi)$) to values greater than one at longer times. This effect is exaggerated by increasing A or σ_L or decreasing the ratio ϕ/ϵ . The physical meaning of this rise and subsequent decline, or crest, in the solute concentration profiles is not intuitively obvious.

A critical consideration of the theoretical model is the fact that the boundary condition for large distances (x approaching infinity) given in Equation 6.13 only applies to Equation 6.23 for relatively short times. Since the velocity decays exponentially, it never reaches zero exactly and therefore the solute can continue to progress beyond the characteristic injection length, although at infinitely slow rates. The evaluation of Equation 6.23 at steady state reveals a linear, homogeneous second-order ordinary differential equation with constant coefficients:

$$D_o^* \frac{\partial^2 C}{\partial \hat{x}^2} - u_o^* \frac{\partial C}{\partial \hat{x}} - k_o^* C = 0. \quad (6.24)$$

Since D_o^* , u_o^* , and k_o^* are all positive numbers, a general steady-state solution is given by

$$C_{ss} = b_1 e^{m_1 x} + b_2 e^{m_2 x}$$

where m_1 and m_2 are

$$m_1, m_2 = \frac{1}{2D_o^*} \left(u_o^* \pm \sqrt{u_o^{*2} + 4k_o^* D_o^*} \right).$$

If we impose the conditions of Equation 6.13, then b_1 must be zero to satisfy the infinity condition, leaving a simple exponential decay to describe the spatial profile of the solute (b_2 is then $\phi \cdot C_{inj}$). This is not consistent with the curves in Figure 6-6, however, which show increases in solute concentration at long times which peak before decaying exponentially to zero.

The reason for this discrepancy is that a steady-state solution in solute concentration cannot exist in a semi-infinite medium. The exponential decay of fluid velocity implies a

corresponding exponential decay in solute velocity, so that solute continuously travels more and more slowly at larger and larger distances. This concept helps to explain the crests in the long-time solute concentration profiles shown in Figures 6-6 (a), (c), (d), (f), and (g). If we examine the roots m_1 and m_2 for each of the cases in Figure 6-6, patterns emerge which correlate with the graphical features; these are summarized in Table 6.1 and illustrated in Figure 6-7 which shows the profiles of Figures 6-6 at one hour. In particular, it is shown that m_1 and m_2 are greatly increased in magnitude when A is decreased to 0.1 mm, and conversely, greatly decreased when A is increased to a value of 5 mm. These correspond to the most extreme decrease and increase, respectively, in the characteristic humps of Figure 6-7, indicating that the higher the dispersivity coefficient, the greater the effect of apparent accumulation (i.e. the rise and subsequent decline in concentration). This is even more evident when we compare the mean convective solute velocity with the mean dispersivity. This ratio can be regarded as a dispersive Peclet number, $Pe = \frac{v_o \varepsilon / \phi \alpha}{A v_o / \alpha^2}$ or

$\frac{\alpha \varepsilon}{A \phi}$. When $Pe > 1$, convection dominates dispersion. This is shown in Fig. 6.6 (b) and (e), which do not show characteristic humps. The humps are most exaggerated in cases (c) and (d), where $Pe < 1$ and thus dispersive effects are greater than convective ones. Again, it is emphasized that this is a direct consequence of the assumption of semi-infinite media complicated by the exponential decay in velocity.

Therefore we can conclude that this effect is due to the choice of values for A in the simulations relative to the ratio ϕ/ε . When the dispersive Peclet number is less than one, dispersive effects dominate and solute disperses or “builds up” at a greater rate than it convects axially. Upon examination of our experimental data (as we shall later see), this ratio is most likely larger than 1 so that convective forces dominate and no accumulation is seen.

case	A (mm)	ϕ	ε	σ_L	D_o^*	u_o^*	k_o^*	m_2	m_2	Pe
(a)	1.0	0.6	0.3	0	1.05	2.05	5.7	3.5	-1.55	1
(b)	0.1	0.6	0.3	0	0.105	1.1	5.7	14.3	-3.80	10
(c)	5.0	0.6	0.3	0	5.26	6.3	5.7	1.8	-0.6	0.2
(d)	1.0	0.8	0.3	0	1.4	2.4	7.9	3.4	-1.65	0.75
(e)	1.0	0.3	0.3	0	0.526	1.5	2.33	4.0	-1.1	2
(f)	1.0	0.6	0.3	0.1	1.05	2.05	7.4	3.8	-1.86	1
(g)	1.0	0.6	0.3	0.3	1.05	2.05	3.7	3.1	-1.13	1

Table 6.1. Summary of the coefficients used for Figures 6-6(a)-(g) with corresponding effective parameter values and implications for fast times. Pe refers to the ratio $\alpha\varepsilon/A\phi$, or the dispersive Peclet number, to which reference was made in the preceding text.

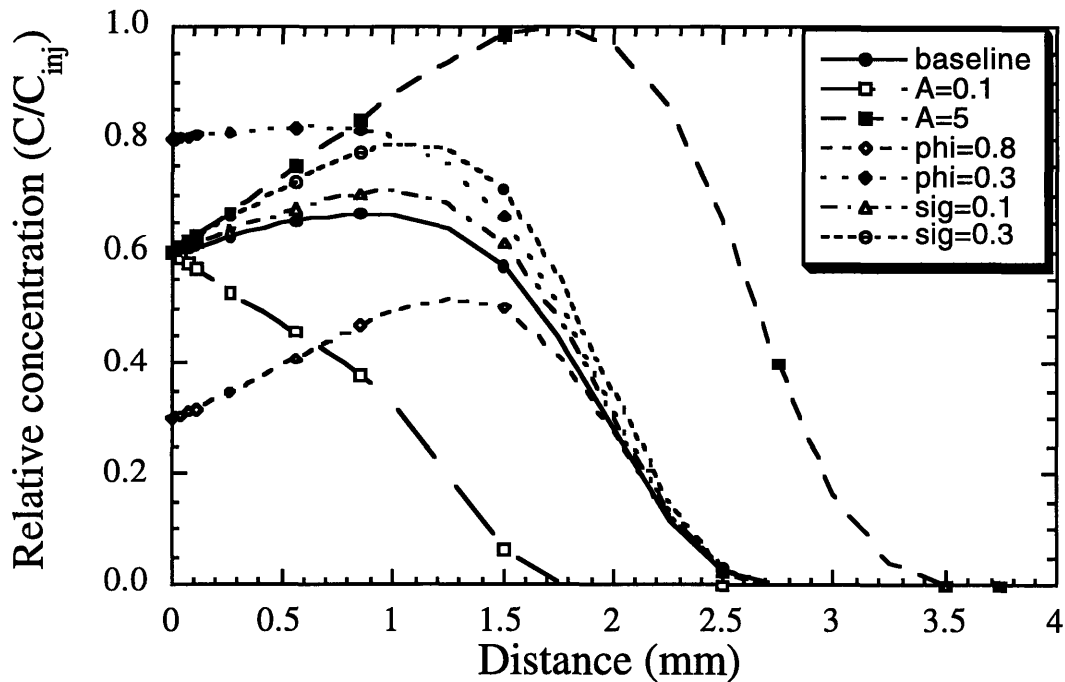


Figure 6-7. Spatial profiles of each case shown in Figures 6-6 (a)-(g) at long times (one hour).

Therefore, dispersivity acts in this model to extend the characteristic length of the infusion region as well as to cause buildup within the convective region. Solute partitioning dictates the magnitude of measurable concentration and the apparent (effective) solute velocity, as well as affects buildup within the convective region, but does not affect the apparent characteristic length for solute transport. Finally, lymphatic reflection coefficient has the least effect on the solute transport profiles, perturbing the shape slightly (increasing the buildup with increasing resistance, as would be expected) but not affecting the apparent solute velocity or apparent characteristic length.

6.6 Experimental data

The first approach was to inject a fluorescently labeled solution of a particular macromolecule, measure its intensity profiles over time, and fit these profiles to one of the characterization methods presented in Sections 6.3-6.5. However, the experimental variation proved to be greater than any measurable differences in solute concentration profiles, and thus differences in transport behavior among different types of solute molecules could not be evaluated.

To avoid ambiguity with fluid flow profiles and experimental variation, a second approach was designed using a coinjection of two solutes, each labeled with a different fluorophore. In this way their transport characteristics could be directly compared because they were convecting with the same fluid flow parameters and relative to the same infusion conditions in the same tissue. For each experiment, one solute was always used for consistency and represented a standard to which the others could be compared. This standard was chosen as a small, neutral molecule: dextran of molecular weight 3 kDa labeled with Texas Red (TR-Dx 3K). It was coinjected with anionic FITC-Dx 3K, FITC-Dx 71K, FITC-BSA (i.e. bovine serum albumin, which also has a molecular weight of approximately 73 kDa but is globular in shape rather than linear like dextran), or FITC-Dx 2M. Therefore 'green' always denoted the experimental solute while 'red' denoted the low molecular weight standard.

A typical spatial profile following a coinjection of FITC-Dx 2M and TR-Dx 3K is shown in Figure 6-8. This profile was taken at 10 minutes from the start of the injection. Distinguishing features include the short-distance plateau, lower apparent dispersivity, and faster apparent propagation of the larger solute. This again suggests that excluded volume plays a major role in determining the spatial profiles - a smaller ϕ would result in faster

apparent velocity and smaller C_{tissue}/C_{fluid} (which is the definition of relative intensity in Figure 6-8). Complete data for each experiment are given in Appendix C.

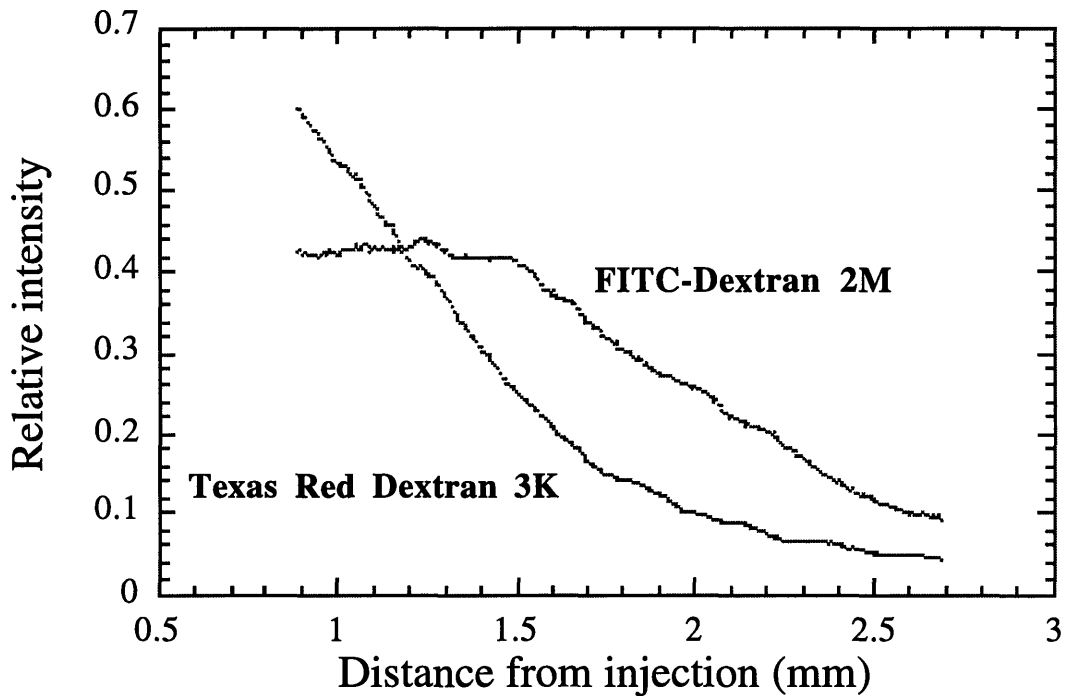


Figure 6-8. Solute concentration profiles for two co-injected molecules at 10 minutes. Intensity was normalized as $\theta = \frac{I - I_{bkgd}}{I_{max} - I_{bkgd}}$, where I was the measured intensity, I_{bkgd} was the pre-infusion or background intensity, and I_{max} was the maximum intensity measured in the tissue (taken as the limit of intensity in smaller and smaller sampling region).

6.7 Analysis and discussion

6.7.1 Net solute velocity

It is appropriate to first evaluate the apparent solute velocity profiles to estimate the relative ϕ for each solute pair, since this is readily achieved. The fluid transport parameters K and β can be estimated by measuring the dependencies of flow and characteristic length on infusion pressure as described in Chapter 5. Or, the averages calculated in Table 5.1 can be used; these were $0.009 \text{ mm}^2 \cdot \text{min}^{-1} \cdot \text{mm Hg}^{-1}$ for K and $0.0024 \text{ (min} \cdot \text{mm Hg)}^{-1}$ for β , respectively, in the range of infusion pressure between 33 and 44 mm Hg (24-35 mm Hg above baseline IFP).

Next, the net velocity of the solute can be measured relative to that of the standard (TR-Dx 3K). Consider $U^* = \frac{\partial x}{\partial \bar{t}}$, where \bar{t} represents the mean residence time or the concentration-weighted average time for the solute to travel a distance x . This can be determined by the RTD method described in Chapter 4:

$$\bar{t} = \frac{\int_0^{\infty} \theta t dt}{\int_0^{\infty} \theta dt}$$

Since

$$U^* = U_o e^{-x/\alpha} = \frac{\partial x}{\partial \bar{t}},$$

$$x = \alpha \ln \left(\frac{U_o}{\alpha} \bar{t} + 1 \right) \quad (6.25)$$

Therefore by comparing $\bar{t}(x)$ for different solutes, U_o and thus $\phi (= \varepsilon + (1-\varepsilon)\kappa)$ can be estimated. This still does not reveal the partition coefficient, but by examining the behavior of ϕ for larger and larger molecules, the lower limit should provide an estimate for ε . That is, if the larger molecule, Dx 2M, is assumed to have negligible partitioning in the solid or

immobile fluid phase, then $\phi_{2M} = \varepsilon$ and the partition coefficient for Dx 3K (κ_{3K}) can be estimated from the measured ratio ϕ_{2M}/ϕ_{3K} by:

$$\kappa_{3K} = \frac{\varepsilon(1 - \phi_{2M}/\phi_{3K})}{\phi_{2M}/\phi_{3K}(1 - \varepsilon)} \quad (6.26)$$

where ε is estimated as the fraction $\varepsilon = \frac{\theta_{tissue}}{\theta_{fluid}} = \frac{C_{tissue}}{C_{fluid}}$ of the large solute molecule.

To show the effectiveness of this method, the mean solute velocity analysis of the data from Figure 6-8 is shown in Figure 6-9. This particular experiment yielded a ratio $\phi_{2M}/\phi_{3K} = 0.58$. A summary of all experiments is provided in Table 6.2.

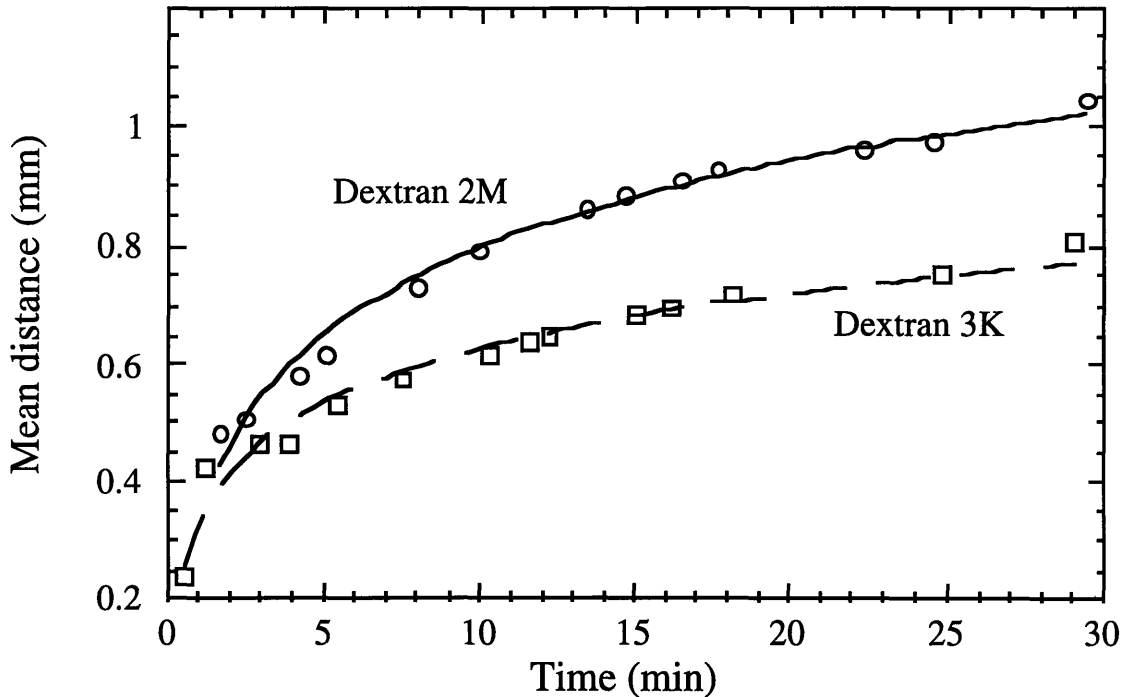


Figure 6-9. Mean distance or length of solute transport vs. time for FITC-Dx 2M and TR-Dx 3K.

Solute coinjected with TR-Dextran 3K (standard)	Average volume fraction ratio ($\phi_{solute}/\phi_{standard}$)
FITC-Dextran 3K (-)	0.89 ± 0.11
FITC-Dextran 71K	0.69 ± 0.08
FITC-BSA	0.64 ± 0.06
FITC-Dextran 2M	0.59 ± 0.09

Table 6.2 Average solute volume fraction relative to that of the standard for four different macromolecules. The molecular weight of BSA is approximately 69K, but unlike dextran of the same molecular weight, it is globular in form.

From Table 6.2, three key generalizations are proposed. First, negative charge may decrease the effective partitioning of the solute. This is expected since the extracellular matrix of skin has a significant percentage of glycosaminoglycans (Aukland and Reed 1993), which contain a high density of negative charge. Therefore we would assume the net effect of a charged matrix on same-charge solute transport would be one of volume exclusion.

Second, there may be reptation effects seen when comparing two molecules of the same size but different shape. Dextran 71K is a linear molecule while BSA (~69K) has a globular form. The BSA shows less effective partitioning, which may suggest that the linear molecule can reptate into spaces which exclude the apparently larger albumin molecule. However, it should be noted that the albumin has a slightly negative charge at physiological pH, which may contribute to the decreased partitioning as well.

Finally, we see a definitive size exclusion effect by comparing FITC-Dx of molecular weights 3K, 71K, and 2M. There is not a linear relationship between molecular weight and ϕ . Larger particles - latex microspheres of 100 nm or larger - showed no mobility within the interstitium following injection, so FITC-Dx 2M was taken as an upper limit of solute size. From this it might be implied that the volume fraction ϕ for FITC-Dx 2M is approximately equal to the mobile fluid volume fraction ϵ , and thus a partitioning coefficient for each molecule can be estimated by Equation 6.26.

To gain further insight into the problem using the simulated data, the net solute velocity implied by each of the cases presented in Figures 6-6 were evaluated according to the simulated data using the same methods. These are shown in Figure 6-10.

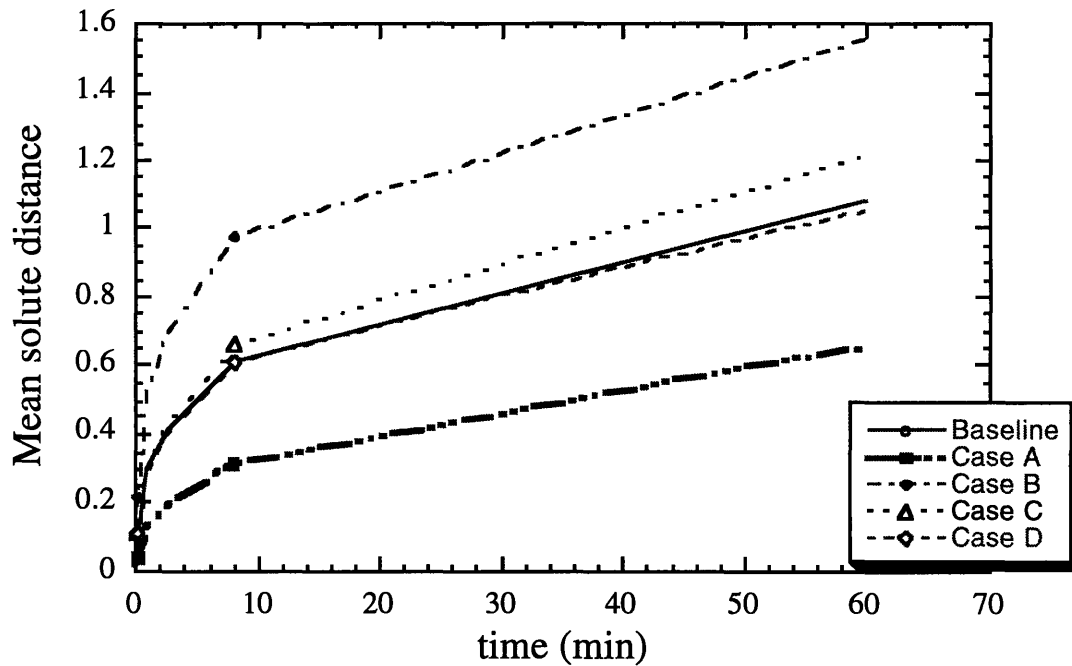


Figure 6-10. Mean solute transport profiles for each of the cases in Figure 6-6.

As expected, the dispersivity strongly affects the apparent solute velocity. In the theoretical analysis, the parameters A and ϕ/ϵ were considered independent. However, it makes sense intuitively that the dispersivity itself would most likely be determined by the volume fraction ratio ϕ/ϵ . This is supported by the simulations shown in Figs. 6.6. Therefore, these data imply that the excluded volume effect is the most important factor in determining solute transport behavior is the excluded volume effect.

6.7.2 Spatial profiles

The spatial profiles from the coinjection data can also be analyzed according to the theoretical developments in Section 6.4. If resistance to solute transport is modeled as an insaturable adsorption phenomenon, the solute concentration profiles (see Appendix C) can be evaluated to yield relative estimates of the effective adsorption rate coefficient (γ) and lymphatic reflection coefficient (σ_L). Upon fitting the curves in Appendix C to Equation 6.8, which are summarized in Table 6.3, it can be seen that the adsorption model is adequate for characterizing differences due to size in solute transport behavior for relatively short times. In other words, the larger the particle, the less interaction (“adsorption”) with the interstitial matrix. However, there seems to be an opposite trend (more solute-matrix interaction) with negatively charged particles as compared to the size-exclusion phenomena described in Section 6.5. This is most likely due to the decreased sensitivity of the methods (i.e. the ratio for FITC-Dx 3K is actually close to 1), which is shown by the large standard deviations in all parameter value estimates.

Solute coinjected with TR-Dextran 3K (standard)	Average ratio γ ($\gamma_{\text{solute}}/\gamma_{\text{standard}}$)	Average ratio k_3 (solute/std) $k_3 = \frac{(1 - \sigma_L)}{\epsilon} - 1$
FITC-Dextran 3K (-)	1.3 ± 0.2	1.6 ± 1.6
FITC-Dextran 71K	0.79 ± 0.02	1.0 ± 0.3
FITC-BSA	1.1 ± 0.09	0.8 ± 0.2
FITC-Dextran 2M	0.58 ± 0.09	0.6 ± 0.4

Table 6.3. Data analysis according to the adsorption model presented in Section 6.4.

Of the k_3 values, only that for FITC-Dx 2M was significantly different from 1 ($p < 0.05$), indicating little differences in lymphatic reflection coefficients among the various solute molecules. This could be due either to the possibility that the lymphatics pose very little resistance to solute transport compared to the interstitium, or to poor sensitivity of the concentration profiles on lymphatic reflection coefficient. Most likely it is the latter; Figure 6-4 shows that when σ_L is increased from 0.1 to 0.5, very little effect is seen on the resulting spatial concentration profile.

6.8 Conclusions

This chapter highlighted the mouse tail model as a unique experimental tool for investigations of interstitial convective solute transport. It is novel both in its approach as well as its capabilities. By offering a simple experimental method for evaluating size exclusion phenomena *in vivo*, it can be used to quickly and easily characterize differences in interstitial transport between different types of molecules. This can be extremely useful for evaluating resistances to protein transport, for example, or for optimizing drug delivery. Furthermore, the coinjection of the solute with a standard reference molecule greatly increases sensitivity by eliminating experimental differences between animals, injection conditions, and flow characteristics particular to the needle placement and specific anatomy of each mouse tail.

Analysis of the solute concentration profiles proved to be nontrivial. Several theoretical models to describe bulk or observable transport behavior were considered, and each were successful in phenomenologically describing at least one characteristic trait. Of those considered, a convection-dispersion model was the most successful at distinguishing transport characteristics of the experimental solute molecules.

We can conclude from the studies in this chapter that size exclusion plays a dominant role in determining the behavior of interstitial convective transport of macromolecules. The studies also suggest that the lymphatics pose little resistance to solute uptake compared to that of the tissue. In other words, if a solute particle can move through the interstitium, it can move even more easily into the lymphatics - this makes intuitive sense because otherwise interstitial accumulation would occur and steady-state oncotic pressure would not be attainable. Finally, it was shown that although size poses the major barrier to transport, charge and configuration of the solute may also affect transport behavior. Some representative molecules were used to make this point clear. It should be emphasized that the experimental studies presented in this chapter were focused on illustrating the development, utility, and sensitivity of the model.

Chapter 7

Model Applications

7.1 Introduction

This chapter illustrates some applications in physiology, medicine, and biology of the model and methods developed in Chapters 3-5. One of the most relevant and important issues in interstitial-lymphatic mechanics is lymphedema. Therefore the first part of this chapter describes the modification of the mouse tail model for lymphedema and a unique surgical technique proposed to relieve certain types of lymphedema. It also reveals physiological implications of such states and quantifies changes which occur in tissue fluid balance at regular time intervals. This work was borne from a collaboration with two surgeons, Drs. Bert Losken and Sumner Slavin of Beth Israel Deaconess Medical Center, and a radiologist, Dr. Annick Van den Abbeele of the Dana-Farber Cancer Institute.

The second part of this chapter describes the application of the model to characterize a genetic rather than surgical modification. This involved a collaboration with Drs. Arja Kaipainen and Kari Alitalo, molecular biologists from Helsinki, Finland. They had discovered a gene responsible for lymphatic endothelial cell growth and developed a strain of transgenic mice in which this gene was upregulated specifically in the skin. We performed analyses on the tails of these mice according to the methods of Section 5.5 to evaluate the effects of this condition on tissue fluid balance parameters. Therefore, net macroscale effects (*in vivo*) could be correlated with microscopic observations of gene expression and cell growth (*ex vivo*). What resulted were valuable insights into lymphatic physiology (which were the first of its kind) and a foundation for integrative studies on mechanotransduction mechanisms in lymphatic regulation of tissue fluid balance.

7.2 Surgical models of lymphedema and tissue flap transfer

7.2.1 Background

Lymphedema is a disease characterized by abnormal collections of fluid and proteins within the interstitial space. Although it can be congenital, lymphedema most commonly occurs on a secondary basis following infection, trauma, malignancy, or treatment for malignant disease with surgery, radiation therapy, or both (Mortimer 1997, Pezner *et al* 1986, Ivens *et al* 1992, Kanter *et al* 1990). Treatment options for this debilitating condition have included drug therapy, physical therapy, and surgical approaches which have yielded limited success (Mortimer 1997, Campisi *et al* 1995, Baumeister and Sivda 1990, Savage 1984, Huang *et al* 1985).

This study had two main goals. The first was to establish an animal model of lymphedema both for its own sake as well as for the evaluation of a potential surgical treatment for certain types of lymphedema, a tissue flap transfer. The second goal was to then use this model to evaluate changes in tissue fluid balance parameters according to the methods outlined in Chapter 5. The surgical treatment option was based on the idea to transfer a small “flap” of tissue from a nearby region with its major artery and vein intact in order to maintain original vascularization. This flap was then sewn into the edematous tissue, offering an alternative route for fluid drainage. The hypothesis that lymphatic continuity is restored in damaged or transplanted tissues was based on clinical observations in patients who had undergone microsurgical reconstruction of post-traumatic deformities (Smith *et al* 1987, Slavin *et al* 1997). In each instance, lymphatic continuity was either restored by the addition of healthy tissues or occurred spontaneously in the absence of surgical lymphatic repair.

Acute lymphedema was produced by ligation of the preischial lymphatics (see Figure 3-3), followed by flap reconstruction in the experimental group. In addition to tail circumference measurements, lymphatic drainage was evaluated by lymphoscintigraphy, and local uptake and flow patterns were observed by fluorescence microlymphangiography (see Chapter 3 for details)

7.2.2 Methods

Experimental groups

This study used 29 female nude mice that weighed between 20-30 g. All surgical procedures were performed inside a pathogen-free colony. Anesthesia was achieved with subcutaneous injections of ketamine (87 mg/kg) and xylazine (13 mg/kg). Animals were

closely monitored post-operatively and received analgesia (butorphanol 3.3 mg/kg SQ q 4-6) when necessary.

The mice were divided into five groups. Group B1 consisted of 6 mice with tail lymphatic ligation only. Group B2 also consisted of 6 mice which underwent ligation and myocutaneous flap transfer. B3-B5 were control groups: B3 was a group of 10 normal animals, B4 consisted of 5 mice with lymphatic tail ligation plus sham myocutaneous flap, and B5 was made up of 2 mice with sham myocutaneous flap only. The sham flap was similar to the experimental tissue flap except that it was replaced *in situ* on the abdomen and sutured to its original site rather than transpose the flap to the tail. These groups served as surgical controls.

In all groups, tail diameters were measured with a caliper at a consistent position on the tail base, which corresponded to approximately 1 mm distal to the ligation in the experimental groups. Interstitial fluid pressure (IFP) was measured with a wick-in-needle method, which is described in Section 3.5.1.

Lymphatic ligation

To identify the deeper lymphatic vessels which led to the ischial nodes, 5-10 μ l of 5% blue dextran 2M (Sigma, St. Louis) in physiological saline (0.9%) was injected into the tip of the tail. The operative site at the base of the tail was then cleansed with 70% ethanol and povidone/iodine, and a circumferential incision was made through the dermis to sever the superficial lymphatic network. The two deep lymphatic vessels located in the lateral aspects of the tail were divided and cauterized under loupe magnification (2.5 x). Finally, cauterization was applied to the edges of the circumferential wound which resulted in a gap of approximately 1 mm between the skin edges followed by secondary healing at the site of ligation.

Myocutaneous tissue flap transfer

For the experimental group (B2), the tail lymphatics were ligated as described above. A 10-15 mm skin incision was made overlying the left rectus abdominis muscle using dissecting scissors. The skin was secured to the rectus muscle at three separate locations to prevent disruption of the myocutaneous perforating vessels. The rectus muscle was incised and the resulting flap was then raised as a unit. The inferior epigastric vessels were identified, defining the pedicle of the flap. Hemostasis was achieved with

cauterization. The abdominal muscles were reapproximated with 4-0 chromic catgut suture (Ethicon). The abdominal skin incision was extended inferiorly to the tail reaching the circumferential wound. Next, the flap was rotated medially 180° on its pedicle and sutured with 6-0 nylon to the distal edge of the prepared recipient site (just distal to the circumferential wound). The remaining skin edges were reapproximated with interrupted 6-0 nylon sutures. This procedure is depicted below in Figure 7-1.

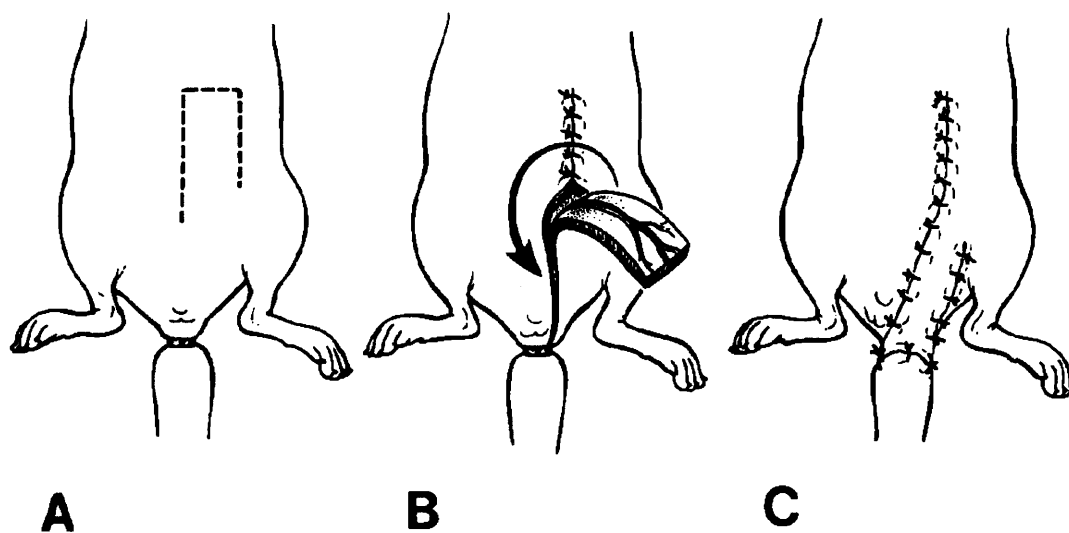


Figure 7-1. Myocutaneous flap design. (A), (B) The flap is inferiorly based, incorporating the inferior deep epigastric artery. (C) The flap has been transposed inferiorly onto the tail proximal to the site of lymphatic ligation

Lymphoscintigraphy (LS)

Each lymphoscintigraphy was performed in the Division of Oncologic Nuclear Medicine of the Dana-Farber Cancer Institute in Boston. Tc-99m-An-sulfur colloid (SC, CIS-US, INC., Bedford, MA) was prepared according to the manufacturer's instructions. The solution was allowed to cool for 15 min and the contents of the vial were then filtered through a Millipore Millex-GS 0.22 mm filter unit. The final preparation was diluted to a concentration of 10 mCi/ml. Quality controls on the filtered product were greater than 95%

bound. This filtered SC preparation is routinely used for lymphoscintigraphic studies in patients. Tc-99m-filtered SC was injected intradermally 1 cm from the tip of the tail of anesthetized mice at a dose of 500 μ ci (18.5 MBq) in a volume of 50 μ l using a 26- or 30-gauge needle.

Imaging of mice was performed on a weekly basis starting the first week post-surgery and up to 13 weeks. Sequential anterior and lateral whole body views (15 min/image) were obtained starting 5 min post-injection up to 3 hours post-injection using a large field of view gamma camera Siemens Body scanner, Siemens MultiSpect 2 (Hoffman Estates, Illinois) or Picker SX-300 (Picker International Inc., Pittsburgh, PA) equipped with an all purpose low energy parallel-hole collimator with a 20% window centered over the 140 keV photopeak. The matrix size was 256 x 256 and a magnification of 1.2-2.6 was used. Animals were kept anesthetized for the duration of the imaging sessions (up to two hours).

Fluorescence microlymphangiography (FM)

FM was performed on the mice once per week post-operatively. The two main goals of this were to collect qualitative images of lymphatic staining and filling patterns and to evaluate quantitatively the tissue fluid balance parameters. A solution of 2% FITC-Dx 2M was continuously infused intradermally at a constant pressure of 45 cm H₂O (33 mm Hg) as described in Chapter 3. After 30 minutes, these fluorescent images of the superficial capillary network were recorded and photographed, with special attention to the extent of the stained network as well as patterns near the ligated region and across the flap. Then, at 30-minute intervals, the infusion pressure was increased by 5 cm water for a total of four infusion pressures (45, 50, 55, and 60 cm H₂O). During each 30-minute interval, the length of the interstitial fluorescence deposit was monitored and the infusion flow rate recorded so that the parameters K and β (overall effective hydraulic conductivity and net lymphatic conductance) could be estimated according to the methods outlined in Section 5.5.

After 14 weeks, three mice each from groups B1-B3 were sacrificed and the ischial lymph nodes were dissected, compressed between a glass slide and cover slip, and examined for fluorescence.

7.2.3 Results

Establishment of lymphedema and reduced swelling with flap transfers

All animals survived the procedures and healed within two weeks. The flaps appeared to have excellent blood supply. Each flap healed to the tail dermal tissues without separation of the wound edges, regardless of whether the flap was actually transposed distally to the tail or replaced *in situ* (groups B2 and B4). No partial or complete necrosis was observed in any flap, nor was there any evidence of wound infection.

Figure 7-2 (*right*) shows the persistence of edema in the ligation group (B1) with tail diameter increases of roughly 20-50% seen throughout the 14-week period in this group as well as the ligation control groups (B4 and B5). Considering the anatomy of the tail, where approximately 35% of the cross-sectional area consists of bone, this corresponds to 60-200% increases in tissue volume. Lymphedema was sustained in groups B1 and B4 for over 60 days in all animals and over 100 days in those which were not sacrificed for lymph node dissection. In the animals undergoing flap transfer following ligation (B2), only slight swelling near the ligation was evident and lymphedema was not seen in any of these animals (Figure 7-2 *center*). Tail diameters are shown in Figure 7-3.



Figure 7-2. *Left:* sham flap control without ligation (B5). *Center:* flap with lymphatic ligation (B2). *Right:* ligation-only animal (B1).

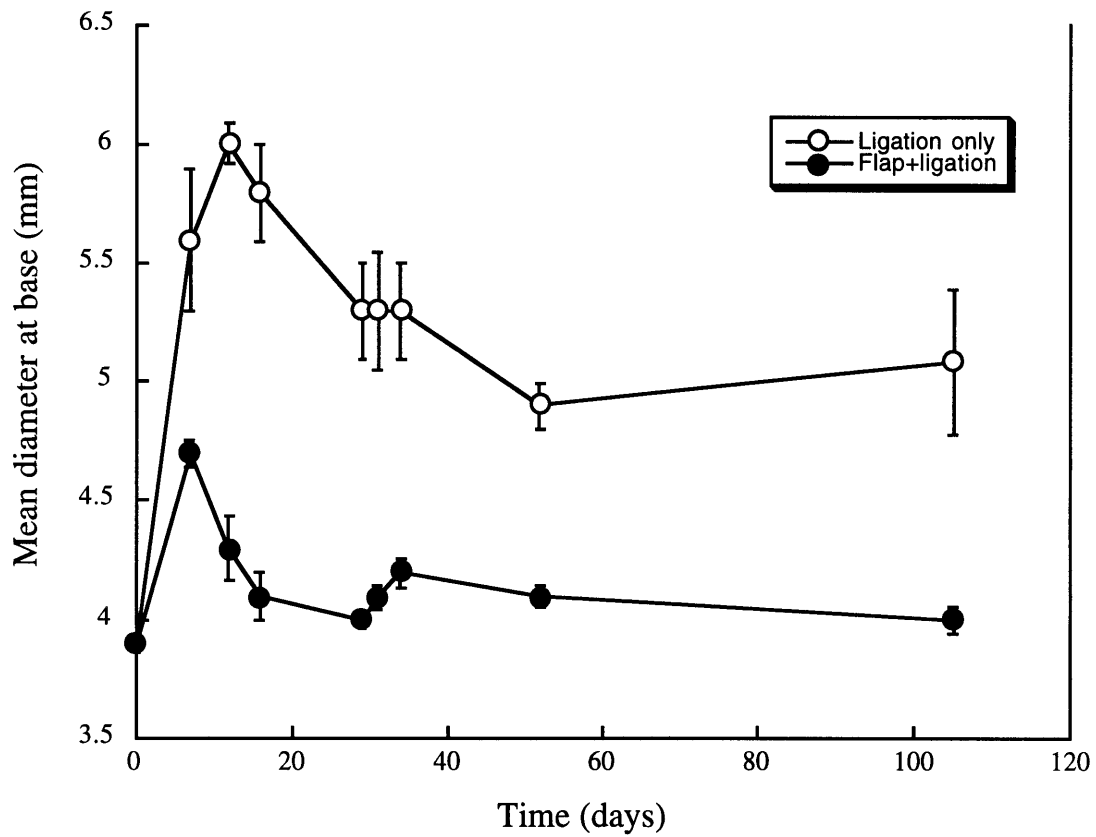


Figure 7-3. Average tail diameter increases for the experimental groups. Solid circles, experimental group (B2); open circles, ligation and sham flap groups (B1 and B4); triangles. Normal groups (no change) not shown.

Lymphatic continuity demonstrated by LS

LS in normal animals (B3) confirmed the lymphatic anatomy described previously (Engeset and Tjøtta 1960). A typical mouse tail lymphoscintigram is shown in Figure 7-4a. All animals showed one or both of the major lymphatic vessels in the tail connecting with one or both lymph nodes located laterally at the base of the tail (the ischial nodes). The lymphatic flow beyond the ischial node(s) resulted in the visualization of the lumbar and/or the renal node in most animals. The pattern of lymphatic vessels and nodal groups seen in the normal animals was also visualized in the animals who underwent a sham flap transfer without ligation (B5, shown in Figure 7-4b). Hepatic activity was always seen and is expected when communication between the lymphatic and venous systems is preserved. Activity was seen in the bladder, kidneys, liver, and thyroid in less than ten percent of animals; this may have been related to the presence of a small amount of free Tc-99m-pertechnetate in the final preparation as well as to some systemic distribution secondary to local superficial disruption of capillary vessels at the site of injection or direct communication with the thoracic duct.

Ligation control animals (Figure 7-4c) showed diffuse uptake within the entire surface of their enlarged tail equivalent to the "cutaneous flare" or dermal back flow seen in patients with lymphedema (Mandell *et al* 1993, McNeill *et al* 1989). In addition, no lymph node groups were visualized. The bladder, kidneys and liver were visualized as in the experimental and control groups, again most likely because of partial systemic distribution of free Tc-99m-pertechnetate. However, the pattern of tracer distribution in this group looked very different from the normal animals who showed no diffuse cutaneous uptake and who always demonstrated at least one lymph node group (B3, Figure 7-4a).

The experimental group that underwent ligation followed by flap transfer (B2, Figure 7-4d) showed linear uptake along the route of the lymphatic vessels in the tail without generalized diffuse uptake as seen in the group with ligation only. Although no lymph node groups were seen during the first week post-operative, they were visualized in the ischial, lumbar, and/or renal regions as early as 2 to 3 weeks post-operative. At that time, lymphoscintigraphy in these animals was virtually indistinguishable from that in normal animals suggesting that reconnection or restoration of lymphatic continuity had taken place within 2-3 weeks following flap transfer, as has been observed previously in patients (Slavin *et al* 1997).

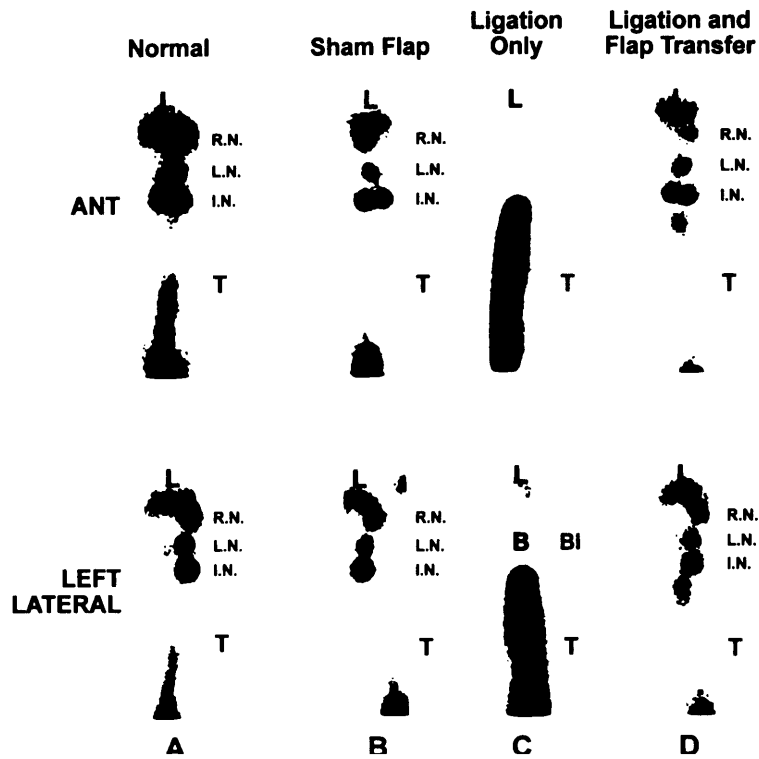


Figure 7-4. Lymphatic vessels and nodal groups in mice as evaluated by LS. The lymphatics and nodes are visualized in the normal (B3, A) and sham flap animals (B5, B). Note the diffuse uptake and the absence of nodal groups in the group of mice that underwent ligation only (B1, C). Restoration of lymphatic vessels and nodal group visualization is seen in the group of animals that underwent flap transfer following ligation (B2, D). *Abbreviations:* A = normal control (B3), B = sham flap without ligation (B5), C = ligation only (B1), D = ligation and flap transfer (B2); T = lymphatic vessels in the tail, I.N. = ischial node; L.N. = lumbar node; R.N. = renal node, L = liver, Bl = bladder.

Flow patterns visualized by FM

Lymphatic flow characteristics, observed weekly with fluorescence microlymphangiography, developed distinctive patterns in each group after 2-3 weeks. Representative photographs from each group of the proximal one-third of the tail, taken 3 weeks post-operatively, are shown in Figure 7-5. The top image shows the lymphatic capillary network of a normal mouse tail (B3). Here, the fluorescent solution is taken up by the lymphatics in the tail tip and stains most of the superficial network. However, its intensity is decreased as it travels proximally and drains to the deeper vessels; the superficial network is barely visible in the most proximal third to fourth part of the tail and only the two deeper vessels along the sides of the tail can be detected. The center image shows the lymphatic capillary network of an edematous tail from group B1 (ligation only). The network is stained in a random manner, indicating backflow from the deeper lymphatics, and near the ligation the fluorescent dye has leaked out from the lymphatics into the swollen tissue. This corresponds to the "cutaneous flare" often seen in patients with lymphedema and in the lymphoscintigrams of this group. This flow pattern was also seen in animals with ligated lymphatics and sham flap (B4).

A representative mouse tail from the experimental group, B2, is shown at the bottom of Figure 7-5. Here, the entire network is stained along the entire length of the tail. However, no lymphatic "leakage" into the tissue was detected, and fluorescent dye could be seen in the flap tissue close to the site of ligation. This indicated evidence of restored lymphatic continuity from the superficial lymphatic structures of the tail into those of the flap.

Finally, the lymph nodes from 3 mice in each group, sacrificed at the end of the fourteen week observation period, also verified that lymphatic reconnection had been achieved with the flap transfer. All the mice in groups B2 and B3 showed fluorescence in at least one node, while none of those in groups B1 or B4 contained fluorescent material, maintaining that total lymphatic obstruction had been achieved and sustained in these animals.

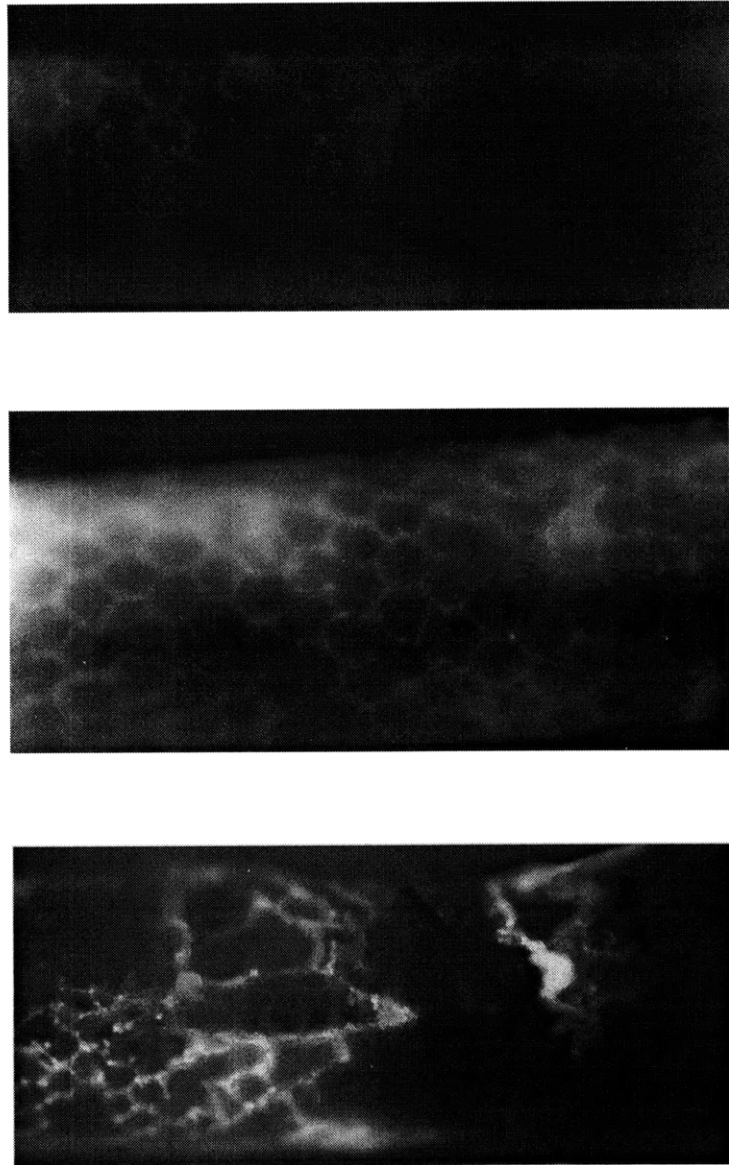


Figure 7-5. Fluorescent images of the cutaneous lymphatic network near the base of the tail following an interstitial infusion of FITC-Dextran 2M at the tail tip. *Top*: A representative image from the control group (normal mouse, B3). Fluorescent dye from the superficial network is seen draining into the deeper vessels along the sides such that only 3/4 of the tail network can be seen. *Middle*: representative image from the ligation group (B1). Note the discontinuity of network staining and leakage into the interstitium. *Bottom*: Lymphatic continuity is restored in the edematous tail following surgical flap transfer (B2). This "reconnection" is seen in the newly grafted tissue from the ligation site.

Evaluation of tissue fluid balance parameters

From each group, the parameters K and β - representing the bulk-effective hydraulic conductivity and lymphatic conductance respectively - could be estimated according to the methods of Section 5.5. Specifically, the product $K \cdot \beta$ was found from comparing infusion pressure vs. infusion flow rate (Equation 5.21), and the ratio β/K from the relationship between characteristic length and infusion pressure (Equation 5.32). Typical data for each are shown in Figures 7-6 and 7-7, which reveal the extent of differences seen between the lymphedema, normal, and flap groups.

The parameters IFP , IFV , K , and β for all experimental groups are presented in Figure 7-8 as normalized quantities, relative to the normal controls. Their absolute values are tabulated in Table 7.1.

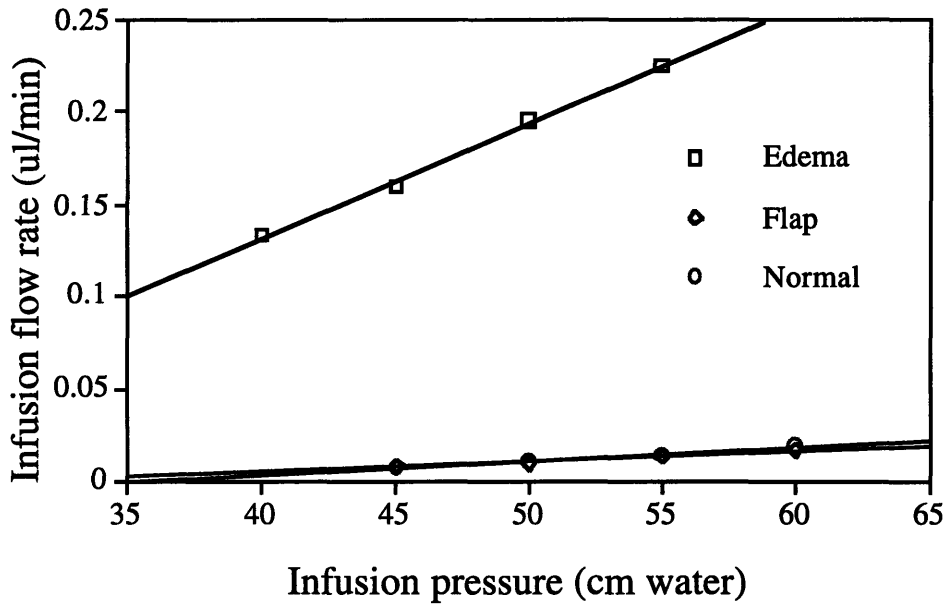


Figure 7-6. Representative data for infusion pressure vs. infusion flow rate for each experimental group. The slope is defined in Equation 5.21.

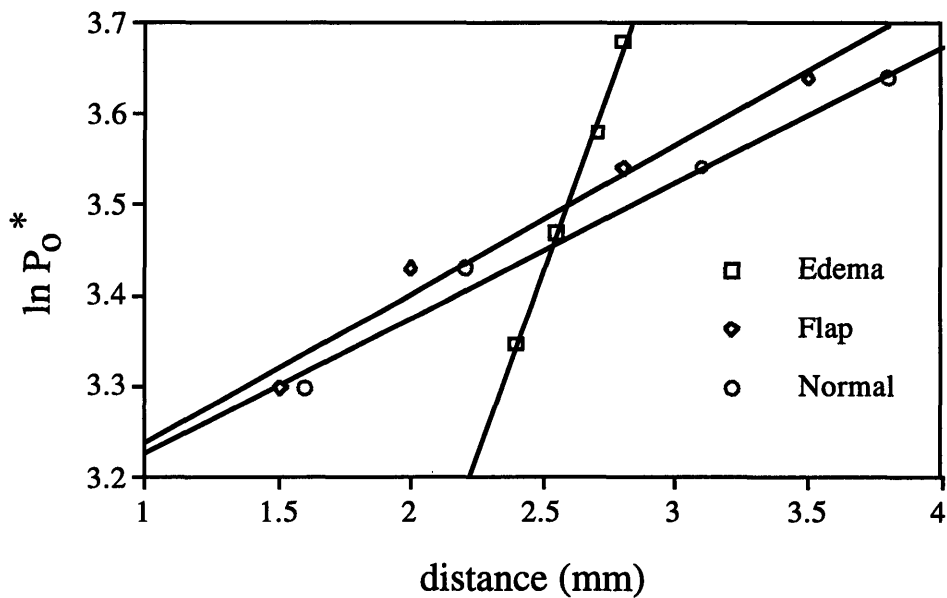


Figure 7-7. Representative data for infusion pressure vs. length of interstitial "front" for each experimental group. The slope is defined by Equation 5.32.

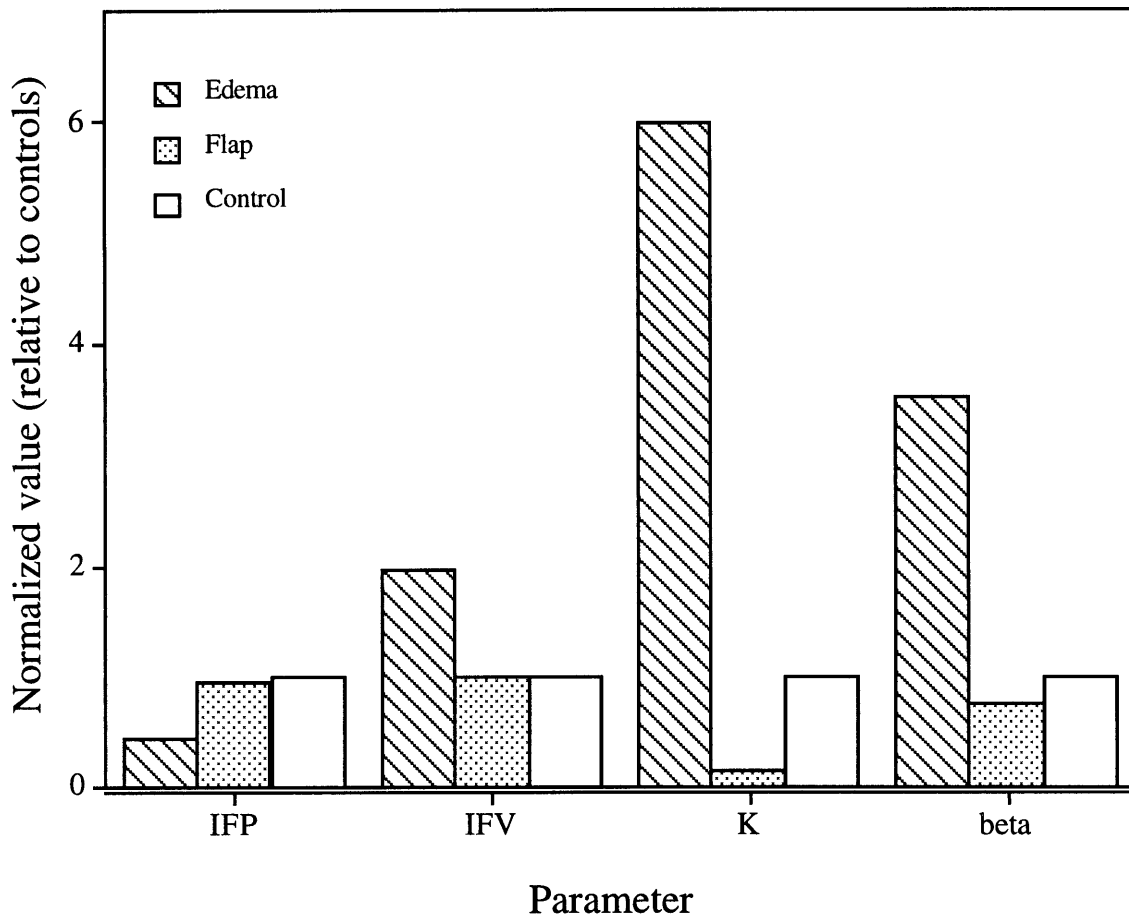


Figure 7-8. Parameters *IFP*, *IFV*, *K*, and β for all experimental groups relative to the normal controls.

	normal	edema	flap
IFP (mm Hg)	5.7 ± 3.5	2.5 ± 2.6	5.3 ± 1.9
increase in IFV (%)	0 ± 5	96 ± 46	0 ± 8
K ($\text{cm}^2 \cdot \text{s}^{-1} \cdot \text{mmHg}^{-1}$)	$3 \pm 8 \times 10^{-6}$	$4 \pm 2 \times 10^{-5}$	$9 \pm 5 \times 10^{-7}$
β ($\text{s}^{-1} \cdot \text{mmHg}^{-1}$)	$9 \pm 3 \times 10^{-6}$	$2 \pm 2 \times 10^{-5}$	$5 \pm 7 \times 10^{-7}$

Table 7.1. Averaged parameter values from all groups at ten days.

7.2.4 Discussion

A new model for lymphedema was developed using the mouse tail model as well as a surgical model for tissue flap transfer. These models were evaluated for changes in tissue fluid balance and lymphatic function over time using two techniques, lymphoscintigraphy (LS) and fluorescence microlymphangiography (FM). The mouse tail models were ideal in their experimental simplicity, reproducibility, and straightforward analysis. By documenting changes that occur following a flap transfer and/or lymphatic ligation, we have introduced and characterized reliable animal models which can be used to explore the potentials of surgical as well as non-surgical treatments of lymphedema and improve our understanding of lymphatic function.

The lymphatic capillary staining patterns shown in Figure 7-5 can be discussed using an analogy to electrical resistances. In the tail skin, a superficial network of lymphatic capillaries drains to two deeper lateral vessels which in turn drain into the ischial nodes as shown by LS. In the control (normal) mouse, FM revealed patterns of lymph flow which suggested that the lymphatic capillaries posed a somewhat greater resistance to flow than the deeper vessels to the extent that roughly 75% of the superficial network was visible. Thus, relative resistances to flow can be qualitatively evaluated - the smaller the extent of stained network, the greater the ratio of resistances between the capillary network and the deeper vessels. In the ligated, edematous tails, almost the entire network was stained with backflow from deeper lymphatics evident by a randomness or discontinuity of staining. This suggested that although the superficial network still presented a greater resistance to lymph flow than the deeper vessels, the blockage of the deeper vessels left the superficial network as the only pathway for lymph flow. Furthermore, the presence of dye "leakage" near the ligation site (also seen with LS as a cutaneous flare) implied that the deeper lymphatics remained at least partially functional after ligation and that the forces for lymph flow rely particularly on local intrinsic pumping mechanisms (as opposed to systemic driving forces such as respiration). This finding is consistent with previous work (Bollinger 1993), where FM was performed in human skin to show that the extent of network staining increased significantly in edema patients (also suggesting an increase in relative resistance of the deeper lymphatics in edematous regions). Other studies have also reported dermal backflow or cutaneous flare in patients with lymphedema (Mandell *et al* 1993, McNeill *et al* 1989).

In the ligation with flap transfer group (B2), lymph flow was "restored" after 10-14 days as suggested by LS and FM with results similar to the control groups. FM showed the absence of edema, the presence of fluorescent material in the flap tissue, and little or no evidence of backflow or leakage near the ligation. Furthermore, LS demonstrated

continuity with major lymphatic vessels and lymph node groups in the experimental (flap) animals after 14 days .

7.2.5 Physiological implications

Aside from presenting valuable experimental tools for the study of various states of tissue fluid balance, these studies provided novel insight into the pathophysiology of lymphedema which were supported or suggested by previous studies (Aukland and Reed 1993, Hogan and Unthank 1986, Schmid-Schönbein 1990, Leak 1976, Ryan 1989, Castenholz *et al* 1991a, Negrini *et al* 1996, Aarli and Aukland 1991, Zaugg-Vesti *et al* 1993).

First of all, IFP was seen to decline rapidly within days of lymphatic ligation. This is shown in Figure 7-8(a) and correlated with severe increases in interstitial fluid volume (IFV), measured by increases in tail diameter and shown in Figure 7-3. This indicates a loss in tissue elasticity (or increase in compliance), which has also been shown to accompany various types of edema by other investigations. For example, Aarli and Aukland (1991) induced chronic edema in the rat tail by venous stasis rather than lymphatic ligation and measured a compliance of 0.93 ml / 100 g tissue / mm Hg (0.93% per mm Hg). This was compared to their earlier study of compliance during acute edema (Aukland and Wiig 1984), which was 0.19% or nearly 5 times less than that during long-term edema (several days). This large increase in compliance apparently takes place over a matter of days, which is also the approximate timescale observed for ECM reorganization (Aukland and Reed 1993). Supporting this is the observation that small fragments of hyaluronic acid, a building block of the proteoglycans which help to “glue” tissue fibers together and provide elastic resistance to deformation (Aukland and Reed 1993, Levick 1987), are found in much greater free concentration in edematous tissue than that found in normal tissue (Negrini *et al* 1996). This suggests an alteration of ECM and a possible proteolytic response of the tissue cells (i.e. keratinocytes or fibroblasts) to swelling, which would manifest a decrease in elasticity. Therefore, our *in vivo* observations of greatly reduced elasticity support this body of literature and also allow day-to-day changes to be quantified.

Next, the decrease in elasticity is also supported by the increase in hydraulic conductivity (K) as shown in Figure 7-8(b). As explained in Chapter 5, the important dependence of hydraulic conductivity on swelling has been observed since Guyton’s classical studies of tissue compliance (Guyton *et al* 1966). In normal mice, the same infusion pressure yielded an estimate of K which was an order of magnitude lower than

that in the edematous tails. The fact that K was seen to increase with time contributes to the idea of a compromised ECM.

Finally, the fact that β also increased with edema indicates that the anchoring filaments, which connect the endothelium of the initial lymphatics with the ECM to facilitate lymphatic drainage, remain intact despite the loss of normal ECM structure. It also signifies the relative importance of local vs. systemic drainage mechanisms. As described in Chapter 3, local swelling facilitates lymphatic drainage by exerting tension on the anchoring filaments which in turn “open up” the otherwise floppy or collapsed initial lymphatic vessels. This lymph must then move to the deeper lymphatics and eventually drain systemically. Lymph is seen to form despite the downstream ligation of the deeper vessels, *i.e.* the removal of systemic forces from local ones. Therefore, the increase in effective lymphatic conductance reveals the local capacity to form lymph, and it also highlights the importance of the anchoring filaments in local lymph formation.

7.2.6 Clinical implications

The absence of a clinically effective treatment for chronic lymphedema reflects a need for an improved understanding of lymphatic function, including lymphatic regeneration and repair. Previous observations in patients undergoing microvascular-free flap reconstruction have demonstrated spontaneous return of lymphatic flow through the transferred tissues and into the host lymphatics as rapidly as thirteen days post-operatively (Slavin *et al* 1997). The present study was initiated by clinical observations of improved lymphatic drainage in human subjects who had flap tissues bearing normal lymphatic networks transferred to areas of abnormal lymph flow. In this study, identification and ligation of the two major lymphatic vessels in the mouse tail provided prompt and consistent swelling in each animal. Control groups undergoing either ligation with or without a sham flap (B1 and B4) developed edema but showed no improvement as determined by tail diameter and volume measurements or assessed by LS and FM.

Transfer of a rectus abdominus myocutaneous flap, vascularized by the deep inferior epigastric artery, created a viable bridge between the obstructed lymphatic channels of a ligated tail and the healthy lymphatic network of the cutaneous and subcutaneous tissues of the flap. The excellent vascularity of the myocutaneous flap promoted wound healing in the area of the tail as well as restoration of lymphatic flow at the junction of flap and severed tail lymphatics. Previously interrupted lymphatic flow showed improvement

over a fourteen day period, culminating in LS and FM evidence of lymphatic transport across the experimentally created obstruction with continuation to proximal nodes.

A precise timing of the process of reconnection - approximately two weeks - suggests that lymphatic growth and repair can occur in an area of abnormal lymphatic function. The importation of healthy lymphatic collectors, as carried by the rectus flap, acts to promote drainage without the risk of donor-site lymphedema. Furthermore, unlike earlier failures in canine models when microvascular anastomoses were performed, late thrombosis was not observed, attesting to the stability of the new pathways.

This study should serve as a stepping stone for the identification of humoral factors affecting afferent and efferent lymphatic continuity within the myocutaneous flap model. If lymphatic pathways can reconnect following surgical division, this principle might be useful to many patients suffering from chronic lymphedema.

7.3 Lymphatic hyperplasia¹

The mouse tail model was also utilized for an investigation of the molecular basis of lymphatic growth and development. The growth factor VEGF-C (vascular endothelial growth factor C) and its receptor VEGFR-3 (vascular endothelial growth factor receptor 3) were found to be specifically associated with the lymphatic endothelia (Kaipainen *et al* 1995, Kukk *et al* 1996). To study the *in vivo* effects of VEGF-C, three transgenic mouse lines were created which expressed VEGF-C under a keratin promoter. Overproduction of VEGF-C in skin keratinocytes led to the upregulation of its receptor VEGFR-3 in lymphatic endothelia. As a result the skin lymphatic endothelial cells proliferated as shown *in vitro* by incorporation of 5-bromo-2-deoxyuridine (BrdU), followed by staining with anti-BrdU antibody. This stained cells which were in the S-phase of DNA synthesis and thus indicated proliferation. Histology revealed that the vessels were dilated and on average contained more cells per cross-section than usual. The *in vivo* studies developed for the mouse tail model in Section 5.5 were then utilized to evaluate differences in lymphatic conductance and staining patterns of the lymphatic capillary network, thus providing insight into the functional implications of this growth factor as well as a basis for further investigations.

¹ This work is partially presented in Jeltsch *et al* 1997.

Fluorescence microlymphangiography of the superficial capillary network in the transgenic mouse tail skin verified the dilation of the lymphatic vessels and are shown in Figure 7-9. This also confirmed the BrdU evidence of proliferation. However, while it verified that the upregulation of VEGF-C induced proliferation of lymphatic endothelial cells, it also suggested that this growth factor does not play a primary role in lymphangiogenesis. That is, no new or sprouting lymphatic vessels were seen and the lymphatic capillary density remained the same as that in the normal mouse.

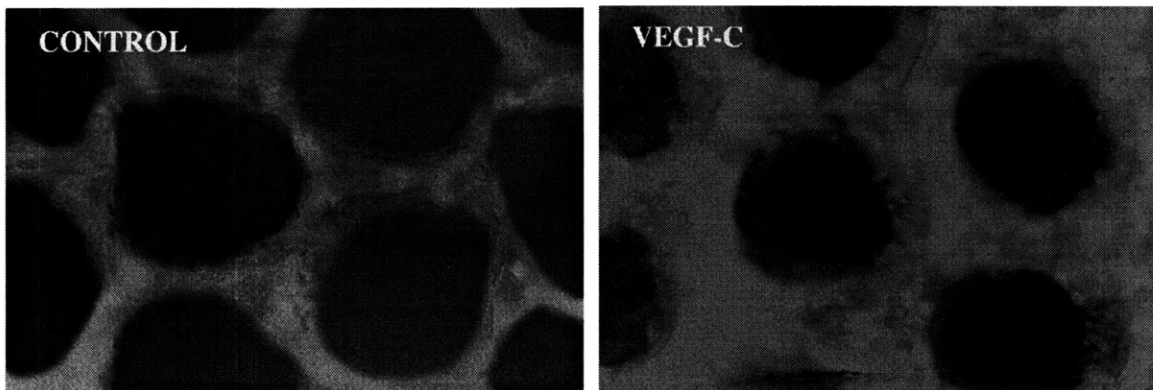


Figure 7-9. Fluorescent microlymphangiography images of the superficial capillary network of normal and transgenic mouse tail skin. Left: control mouse, where the average diameter of a lymphatic vessel is $68 \pm 22 \mu\text{m}$ and the distance across a hexagonal unit (center -to-center of opposite vessels) is $490 \pm 60 \mu\text{m}$. Right: VEGF-C upregulated mouse, where the average vessel diameter is $142 \pm 26 \mu\text{m}$ and the hexagonal mesh unit size is approximately the same, $510 \pm 60 \mu\text{m}$.

Aside from qualitative observations, the tissue fluid balance parameters could also be estimated with the methods outlined in Section 5.5. Hydraulic conductivity (K) was not significantly different between the two mouse types, but there was nearly a threefold difference in local lymphatic conductance (β). While the normal or control mice had a mean value of $2.2 \pm 0.6 \times 10^{-5} \text{ s}^{-1} \cdot \text{mmHg}^{-1}$ ($n=5$), the transgenics showed a mean value of $8 \pm 1 \times 10^{-6} \text{ s}^{-1} \cdot \text{mmHg}^{-1}$ ($n=4$).

This was somewhat surprising but contributed valuable insight into lymphatic physiology. It seems paradoxical that initial lymphatic vessels with a larger lumen would be less effective at draining fluid. However, the image of the anchoring filaments (Figure 2-2) is a reminder of the importance of interstitial-lymphatic communication in lymph formation. The initial lymphatic vessels have no smooth muscle and are typically non-cylindrical and often twisted or collapsed. The elastic fibers sense slight stresses in the interstitium which facilitate lymph formation by pulling the vessel open and increasing the translymphatic pressure difference, which is the driving force for lymph formation. This is consistent with observations that IFV rather than IFP most clearly influences lymphatic drainage (Hogan and Unthank 1986, Aarli *et al* 1990). If the vessels were larger but still twisted and partially collapsed, then the same interstitial stresses would have a lesser effect on increasing the intraluminal volume of the lymphatic vessel. In this way, larger initial vessels are less effective at draining lymph than smaller ones. This effect has also been seen in tumor vessels lacking smooth muscle cells (Jain 1988).

Therefore the tail model was useful for evaluating macroscopic changes due to alterations in molecular control. Not only could we confirm histological data with macroscale *in vivo* measurements of associated changes in tissue fluid balance parameters, but along with Section 7.2, these studies also yielded fruitful information about the importance of interstitial-lymphatic communication and its role in the pathophysiology of lymphedema. Currently, these two studies are being combined and extended to delineate molecular changes associated with lymphedema and tissue flap transfer. While the work presented in this chapter evaluated macroscale consequences of molecular regulation, current and future work examines molecular responses to changes in the macroscopic environment (*i.e.* swelling and tissue transfer).

Chapter 8

Conclusions and future direction

The main contribution of this thesis is a framework for comprehensive investigations of interstitial-lymphatic transport. First, an experimental model was designed for observing and evaluating flow in lymphatic capillaries using the mouse tail. Then the physiology of lymph formation was explored, expanding the technical potential of the model and constructing a theoretical foundation simultaneously. This parallel development was necessary for optimizing relevance in the theoretical model and pertinence in the experimental design. The experimental / theoretical model is further expanded to include solute transport within the interstitial-lymphatic continuum.

The utility of the model was evaluated by its application to critical issues in lymphatic function. Lymphedema and hyperplasia of lymphatic vessels are both related to interstitial-lymphatic mechanics, and interstitial-lymphatic communication is critical in the healing of wounds and tissue grafts. Physiological, pathological, and biological aspects of lymphedema, hyperplasia, and tissue grafting were combined with the mechanical studies that the mouse tail model could provide to yield valuable and comprehensive insight into these problems.

The importance of this work can be summarized in the value of the model as a theoretical and experimental tool along with the physiological implications of the applied studies. The model was used to elucidate certain mechanical aspects of tissue fluid balance as well as convective interstitial solute transport. As a result, it could be used to estimate the hydraulic conductivity (K), elasticity ($2\mu+\lambda$), and overall lymphatic conductance (β) of skin *in vivo*. This is the first such *in vivo* tool. Solute transport was analyzed as a convective-dispersive phenomenon, employing a drainage term to represent lymphatic uptake. This approach was motivated by the chromatography-like concentration profiles observed within the mouse tail skin. Once again, it was the first such model in which solute

transport parameters (excluded volume fraction, dispersivity, and the lymphatic reflection coefficient) could be estimated *in vivo*.

Applying the model to physiologically relevant problems has led to important observations from the standpoint of interstitial-lymphatic biology. For example, edema was found to be associated with a local increase in K and β , and caused a local decrease in IFP. The latter suggested a loss of tissue elasticity, and although K is known to increase with swelling (Guyton *et al* 1966, Bert and Fatt 1970, Levick 1987, Bert and Reed 1995), the increase in β was not expected. This observation alone has two key implications: (1) local forces dominate systemic forces in generating lymph formation and local lymph propulsion, and (2) while the extracellular matrix (ECM) may be subjected to proteolysis during sustained swelling, interstitial-lymphatic communication seems to be preserved (i.e. the anchoring filaments remain intact and functional). In the tissue graft or flap transfer model, lymphatic continuity was established between two different tissue types within two weeks. Finally, the model was used on many levels simultaneously to show that solid stress rather than IFP is the most important factor in lymphatic drainage, ECM reorganization, and lymphatic cell gene expression.

This work establishes a unique framework for novel studies of interstitial-lymphatic transport phenomena. Because it allows *in situ* examination of interstitial-lymphatic mechanics and transport, it is an ideal tool for multi-scale investigations. The feasibility of such a comprehensive model arises from the rapidly expanding field of molecular biology and its emergence as a quantitative science. The scope of Chemical Engineering has been expanding and changing over the past few decades to incorporate biology and physiology as applications. As a result, its tools and approaches can be used to further our fundamental understanding of biological and physiological systems as well as to translate current knowledge into the development of biotechnology. The work presented in this thesis is an example of such a multidisciplinary development which can both give and take from basic science. In this case, fundamental principles of mechanics and transport were applied to a physiological system, allowing for parallel development of experimental and theoretical techniques, to produce a quantitative and relevant model. Advances in other fields (biology and medicine) were incorporated into this model leading to a comprehensive tool. Such a tool can be used both to further our understanding of physiological issues (*i.e.* tissue fluid balance, edema, and lymphangiogenesis) as well as to explore and develop biotechnological applications.

One such application is the use of the lymphatic route for drug delivery. Because the lymphatic capillaries have a markedly higher permeability than those of the blood, particles of up to 500 nm can be selectively taken up from the interstitial space. Lymphatic flow rates are 1-2 orders of magnitude less than that of blood, yielding long residence times and minimal shear stress. Along with lymph node detention, these features are ideal for specific targeting of lymph nodes. Delivery applications include contrast agents for lymph node imaging (used for detection of tumor metastases), drugs which affect the immune response by activating white blood cells against a particular antigen (immunomodulators, currently investigated for HIV and cancer therapy), and some chemotherapeutics for the treatment of lymph node metastases (Torchilin 1996, Charman *et al* 1992). In the case of immunomodulators, systemic delivery trials have been unsuccessful due to liver degradation and ineffective targeting; both may be avoided by lymphatic delivery. Also, since the major problems with chemotherapy are the side effects resulting from systemic distribution, the potential of specific targeting to lymph node metastases carries important therapeutic implications. The model developed in this thesis is ideal for combining *in vivo* studies of lymphatic transport with theoretical modeling of interstitial-lymphatic convection and distribution, binding, and phagocytosis kinetics to explore the lymphatic delivery route.

A second direction for this model is in the further exploration of mechanoregulation of lymphatic growth and development. This work is currently being carried out as an extension to the work presented in Chapter 7 in collaboration with Drs. Arja Kaipainen and Judah Folkman of Children's Hospital in Boston. Since the lymphatic capillaries are intrinsically and mechanically coupled to the ECM, their function not only depends on tissue pressure and systemic lymphatic clearance but perhaps even more importantly on the geometry and structure of the capillary network and surrounding ECM assembly. Furthermore, the lymphatic endothelial cells may respond specifically to sustained local mechanical forces by proliferation or apoptosis; enlarged and nonfunctional vessels are often associated with various forms of lymphedema and cancers of the lymphatic system (Mortimer 1997, Leu and Lie 1995). In fact, mechanotransduction mechanisms of lymphatic development and disorders are completely unexplored. The work developed in this thesis is an ideal foundation from which to bring together interstitial-lymphatic transport mechanics at the macroscopic level with response and regulation at the molecular level so that lymphatic regulation can be described quantitatively and comprehensively.

Finally, the role of the lymphatics in tumor growth and metastasis is another avenue for future exploration. The lymphatics are the major route for dissemination of many soft tissue tumors, such as breast and colon carcinomas, and the interaction between the

growing tumor and the surrounding extracellular matrix is a critical factor in the prognosis of such cancers (Lochter and Bissel 1995, Carr *et al* 1989). Furthermore, tumors are typically devoid of functional lymphatic vessels. The unique qualitative and quantitative features of the mouse tail model provide an ideal tool for studies of tumor-lymphatic interactions. These features include the visibility of stained lymphatic vessels, the potential to track labeled cells within the superficial lymphatic capillary network, the variety of characterization techniques for lymphatic uptake, interstitial fluid balance, and flow within the lymphatic capillaries.

Our overall understanding of lymphatic physiology and biology has lagged behind that of the blood circulation. Thus, there exists many unanswered questions and a frontier for exploration. The work developed throughout this thesis constitutes a unique foundation for investigations of lymphatic function. These examples are just a few of the many interesting future directions which arose from this work.

Appendix A

Nomenclature

A_c	tissue cross-sectional area for fluid flow	Ch. 5
A	convective dispersion parameter ($D^c = A \cdot v$)	Ch. 6
C	total tissue concentration	Ch. 6
C_{inf}	solute concentration of the infusate	Ch. 6
D^*	effective dispersivity [mm^2/s]	Ch. 6
D^c	convective dispersivity [mm^2/s]	Ch. 6
D^M	molecular diffusivity [mm^2/s]	Ch. 6
e	dilatation of solid phase of the interstitium	Ch. 5
H	bulk elastic modulus ($2\mu + \lambda$) [mmHg]	Ch. 5
J_v	net volumetric lymphatic fluid drainage [ml/g tissue/s]	Ch. 5
K	hydraulic conductivity [$\text{mm}^2 \text{ s}^{-1} \text{ mm Hg}^{-1}$]	Ch. 5-7
K^*	effective pressure diffusivity ($=K(2\mu + \lambda)$) [mm^2/s]	Ch. 5
L_p	average permeability of lymphatic capillary [mm/(s·mm Hg)]	Ch. 5
n	adsorbed solute concentration [moles per volume solid]	Ch. 6
P	interstitial fluid pressure (IFP) [mm Hg]	Ch. 5-7
P^*	pressure above baseline; $P - P_o$ [mm Hg]	Ch. 5-7
P_b	Baseline IFP [mm Hg]	Ch. 5-7
P_i	interstitial fluid pressure (IFP or P) [mm Hg]	Ch. 5
P_l	intralymphatic (local) pressure [mm Hg]	Ch. 5
P_o	infusion pressure [mm Hg]	Ch. 5-7
P_o^*	applied pressure above baseline ($P_o - P_b$) [mm Hg]	Ch. 5-7
Q	net flow rate of infusion [$\mu\text{l}/\text{s}$]	Ch. 5-7

Q_{ss}	steady-state flow rate of infusion [$\mu\text{l/s}$]	Ch. 5-7
R_s	net systemic resistance to lymphatic drainage [$\text{s}\cdot\text{mm Hg}$]	Ch. 5
R_t	total lumped (series) resistance to lymphatic drainage [$\text{s}\cdot\text{mm Hg}$]	Ch. 5
R_{v_s}	lymphatic uptake rate of solute [moles/g/s]	Ch. 6
S/V	surface area-to-volume ratio of lymphatic capillaries [mm^{-1}]	Ch. 5
\hat{t}	dimensionless time	Ch. 6
\bar{t}	mean residence time (MRT)	Ch. 4-6
\mathbf{u}	solid displacement vector	Ch. 5
$\bar{\mathbf{u}}$	average solid displacement vector	Ch. 5
U_o	mean solute velocity at $x=0$ [mm/s]	Ch. 6
U^*	mean solute velocity [mm/s]	Ch. 6
v_{bulk}	bulk (average) fluid velocity ($v_{bulk} = \varepsilon \cdot v_{pore}$)	Ch. 6
$\bar{\mathbf{v}}_f$	bulk fluid velocity vector ($\bar{\mathbf{v}}_f = \varepsilon \cdot \bar{\mathbf{v}}$)	Ch. 6
v_{pore}	average pore fluid velocity	Ch. 6
$\bar{\mathbf{v}}$	average pore fluid velocity vector	Ch. 5
\hat{x}	dimensionless distance	Ch. 6
α	characteristic (SS) length of pressure and solute profiles [mm]	Ch. 5-7
β	lymphatic conductance [$\text{s}^{-1} \text{mm Hg}^{-1}$]	Ch. 5-7
ε	porosity or fluid volume fraction	Ch. 5-6
$\underline{\underline{\varepsilon}}$	Cauchy strain tensor	Ch. 5
ϕ_p	Available volume fraction (fluid + partitioning phases) for molecule or particle p	Ch. 6
γ	insaturable adsorption affinity; $\gamma = \psi \kappa (1 - \varepsilon)$	Ch. 6
κ	partition coefficient for solute transport	Ch. 6
λ	2nd Lamé constant	Ch. 5
μ	1st Lamé constant	Ch. 5
ψ	linear adsorption coefficient [s^{-1}]	Ch. 6
ρ_f	fluid density fraction of tissue	Ch. 5

ρ_s	solid density fraction of tissue	Ch. 5
σ_L	lymphatic reflection coefficient	Ch. 6
$\underline{\underline{\tau}}$	total tissue stress tensor	Ch. 5
θ	normalized intensity	Ch. 4-6
T_f	characteristic time for fluid transport	Ch. 4-6
T_p	characteristic time for pressure equilibrium	Ch. 5
T_s	characteristic time for solute transport	Ch. 6
ζ	solute drag coefficient	Ch. 6
$(2\mu+\lambda)$	bulk elastic modulus (H) [mm Hg]	Ch. 5

BSA	bovine serum albumin
ECM	extracellular matrix
FITC	Fluoroisothiocyanate
FITC-Dx 3K	FITC-labeled dextran, mol. weight 3,000 Da
FITC-Dx 71K	FITC-labeled dextran, mol. weight 71,000 Da
FITC-Dx 2M	FITC-labeled dextran, mol. weight 2,000,000 Da
Flt4	fms-like tyrosine kinase receptor 4 (also called VEGFR3)
FM	fluorescence microlymphangiography
FRAP	fluorescence recovery after photobleaching
IFP	interstitial fluid pressure
IFV	interstitial fluid volume
LS	lymphoscintigraphy
MRT	mean residence time
RITC	rhodamine B isothiocyanate
RITC-Dx 73K	RITC-labeled dextran, mol. weight 73,000 Da
RTD	residence time distribution
TR-Dx 3K	Texas Red-labeled dextran, mol. weight 3,000 Da.
VEGF	vascular endothelial growth factor (aka vascular permeability factor (VPF))
VEGF-C	vascular endothelial growth factor C
VEGFR3	vascular endothelial growth factor receptor 3 (also called Flt4)

Appendix B

Experimental data: pressure propagation

Figures B-1 (a)-(e) below show transient pressure profiles of each experiment used in Chapter 5. Unmarked lines show IFP as measured with a micropipette while the lines marked with circles show the infusion pressure which was measured with a pressure transducer in the infusion line.

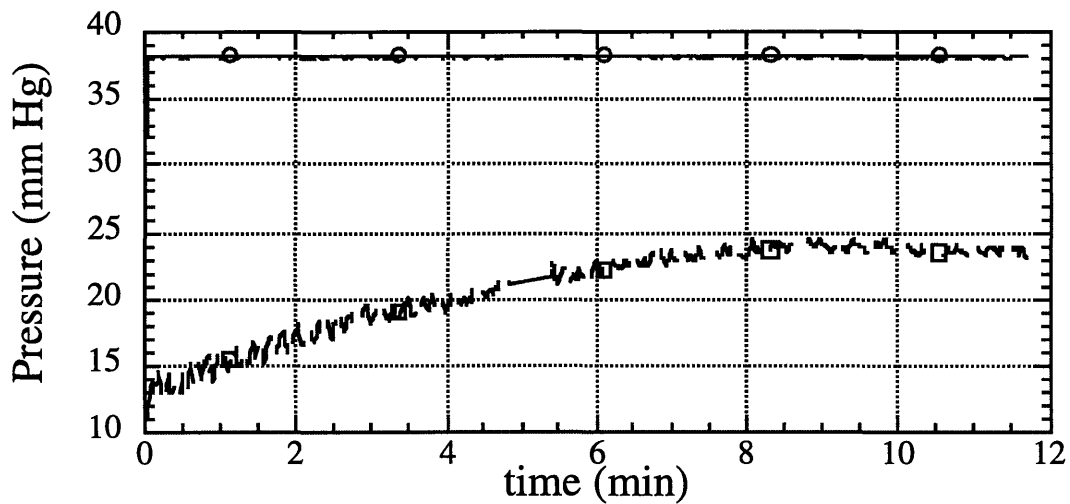


Figure B-1 (a). Transient pressure profile; experiment #1.

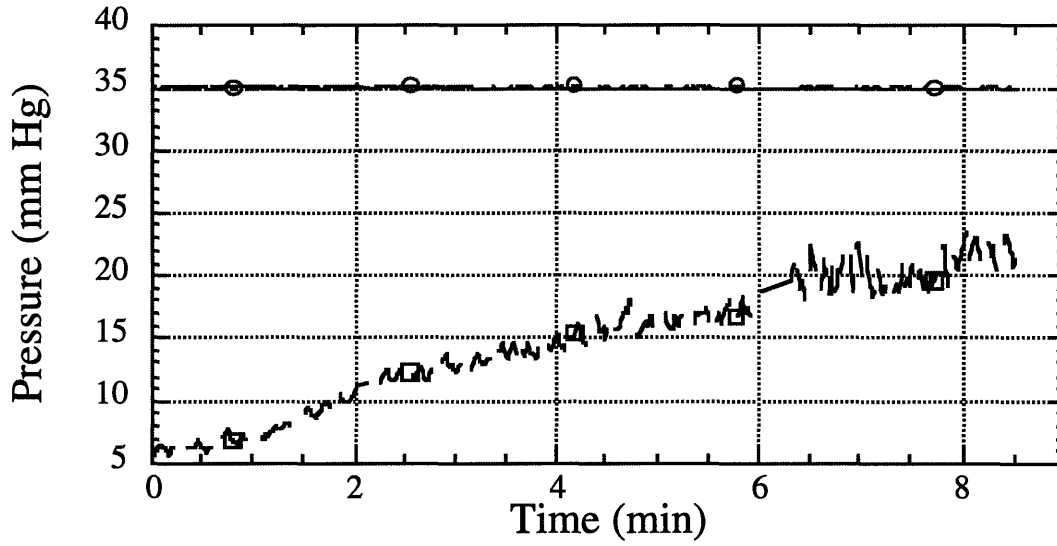


Figure B-1 (b). Transient pressure profile; experiment #2.

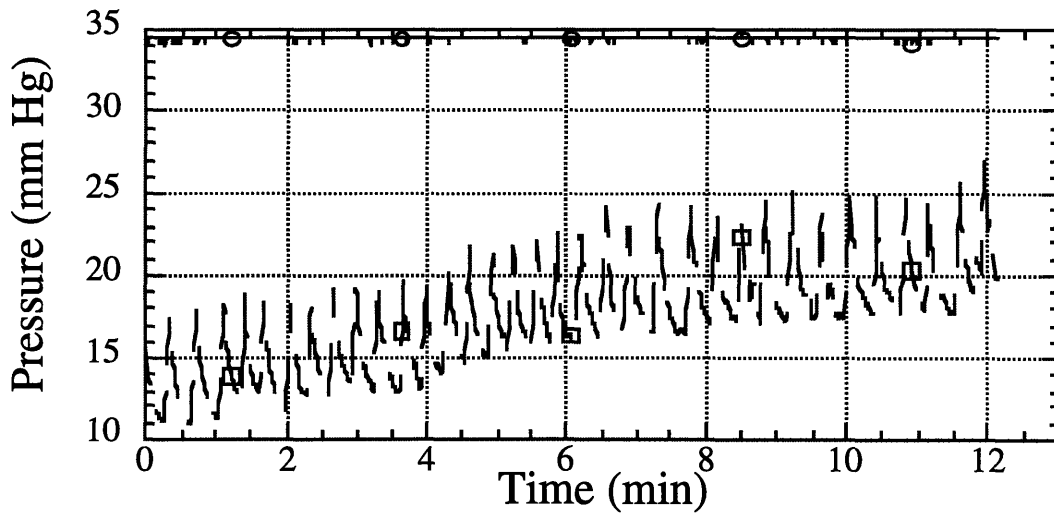


Figure B-1 (c). Transient pressure profile; experiment #3.

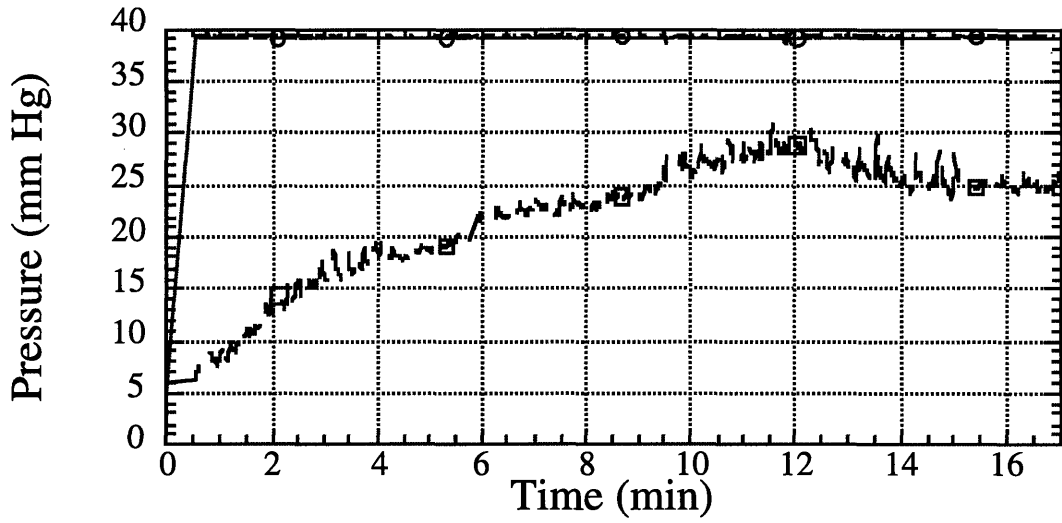


Figure B-1 (d). Transient pressure profile; experiment #4.

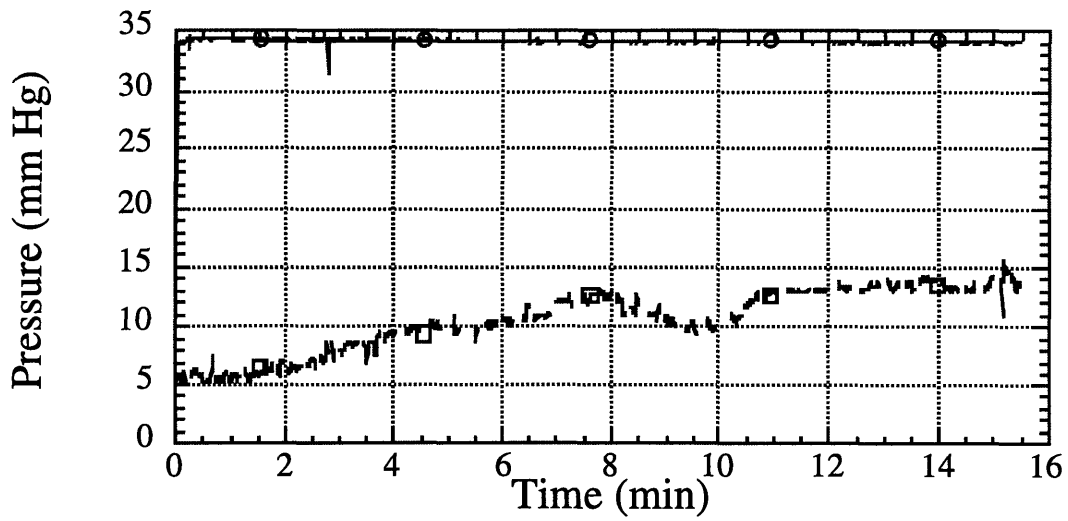


Figure B-1 (e). Transient pressure profile; experiment #5.

Appendix C

Experimental data: solute co-injections

Three experiments were performed for each FITC-labeled molecule (anionic Dx 3K, Dx 71K, Dx 2M, and BSA). Each solution was coinjected with TR-Dx 3K (neutral). Thus, each data set is given as a pair of graphs, with the experimental molecule on the left and TR-Dx 3K on the right. Timepoints are indicated on the legend in minutes. Intensities (y-axis) have been corrected for background readings. The first three sets (Figs. C.1 (a)-(c)) show data for anionic Dx 3K; Figs. C.2 (a)-(c) show data for Dx 71K; Figs. C.3 (a)-(c) show data for Dx 2M, and finally, Figs. C.4 (a)-(c) show data for BSA.

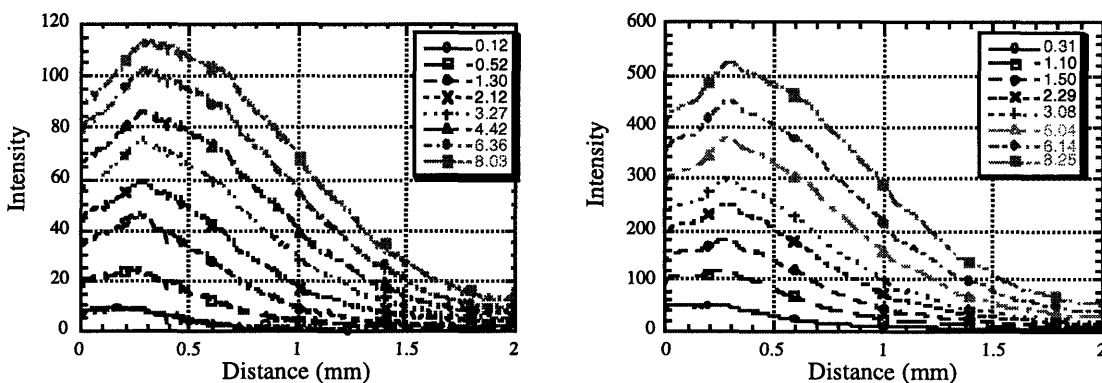


Figure C-1 (a) Experiment #1: spatial profiles of anionic FITC-Dx 3K (left) coinjected with TR-Dx 3K (right). Times (in minutes) are indicated in the legend.

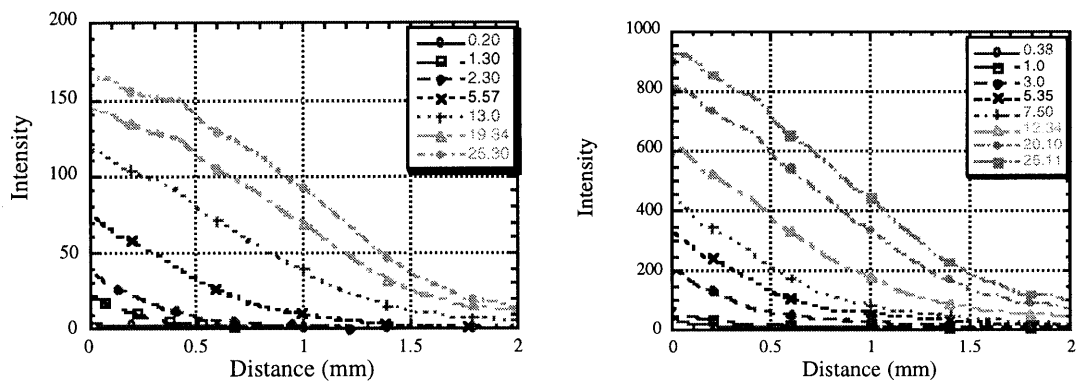


Figure C-1 (b) Experiment #2: spatial profiles of anionic FITC-Dx 3K (left) coinjecting with TR-Dx 3K (right).

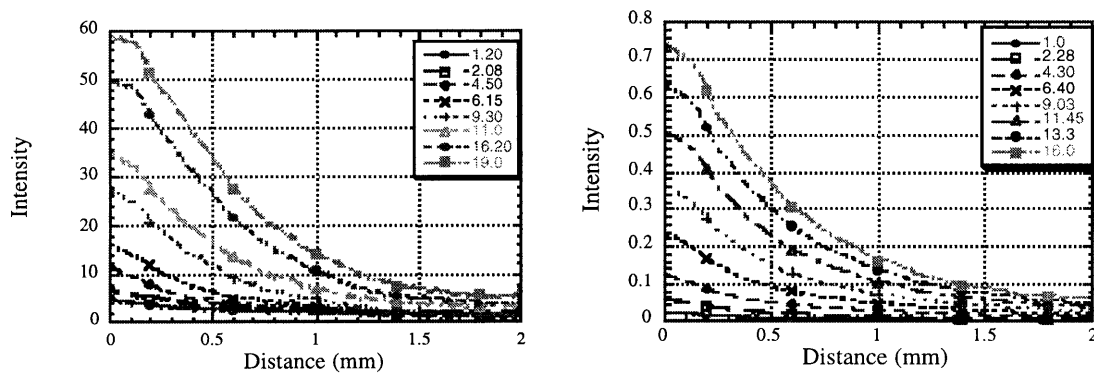


Figure C-1 (c) Experiment #3: spatial profiles of anionic FITC-Dx 3K (left) coinjecting with TR-Dx 3K (right).

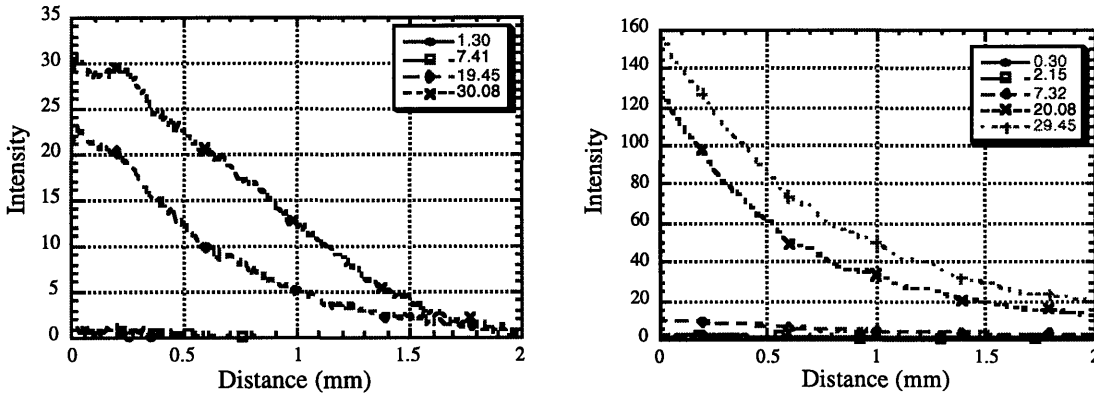


Figure C-2 (a) Experiment #4: spatial profiles of FITC-Dx 71K (left) coinjecting with TR-Dx 3K (right).

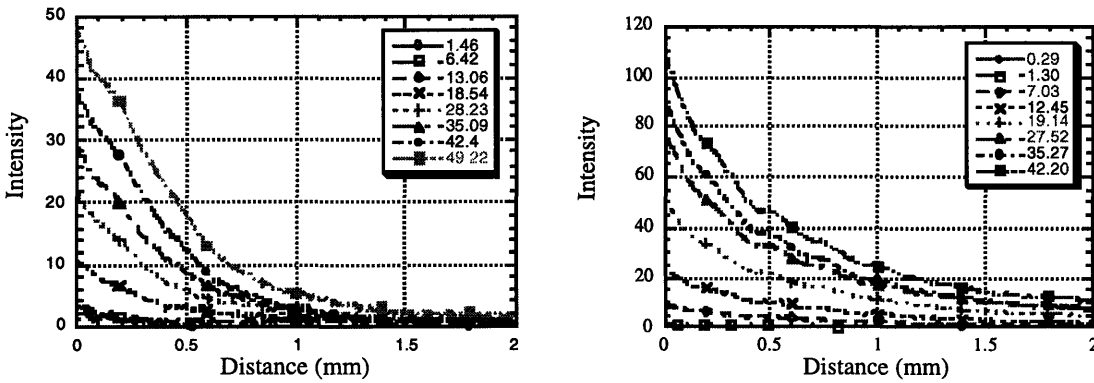


Figure C-2 (b) Experiment #5: spatial profiles of FITC-Dx 71K (left) coinjecting with TR-Dx 3K (right).

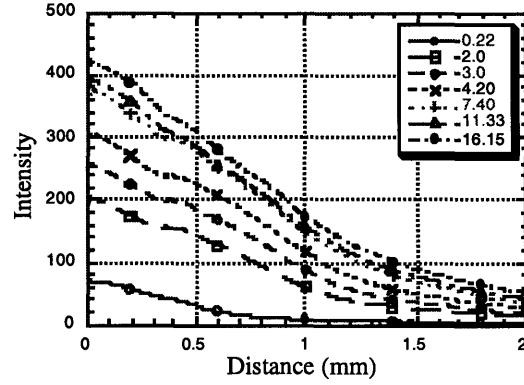
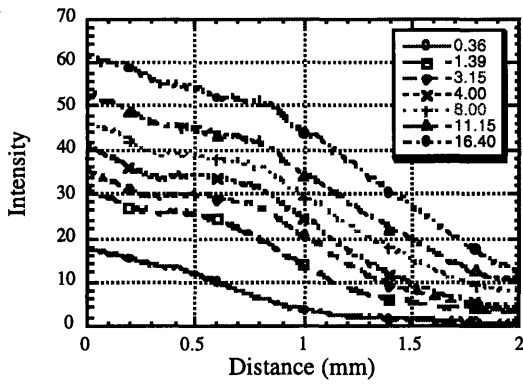


Figure C-2 (c) Experiment #6: spatial profiles of FITC-Dx 71K (left) coinjected with TR-Dx 3K (right).

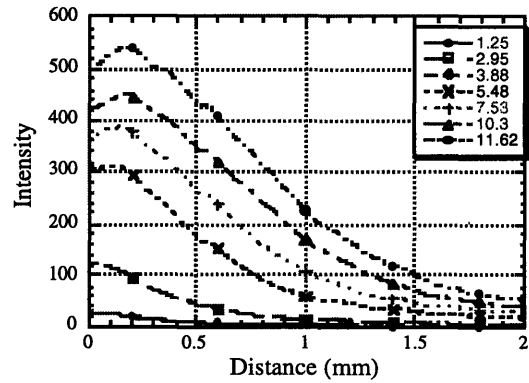
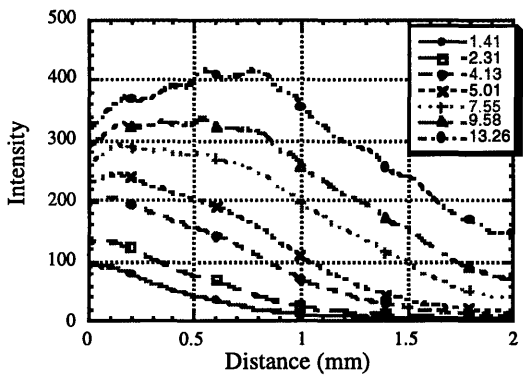


Figure C-3 (a) Experiment #7: spatial profiles of FITC-Dx 2M (left) coinjected with TR-Dx 3K (right).

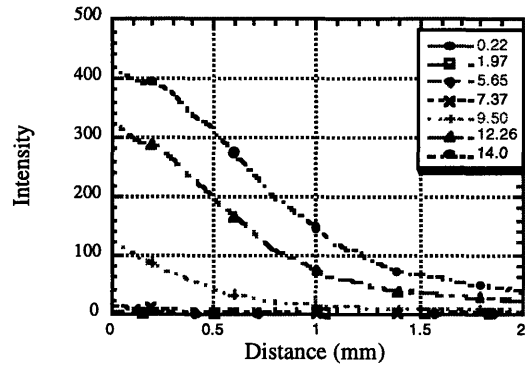
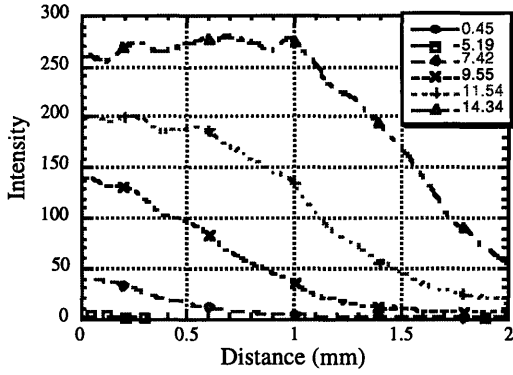


Figure C-3 (b) Experiment #8: spatial profiles of FITC-Dx 2M (left) coinjected with TR-Dx 3K (right).

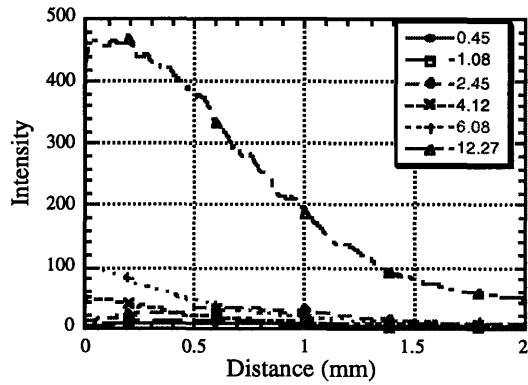
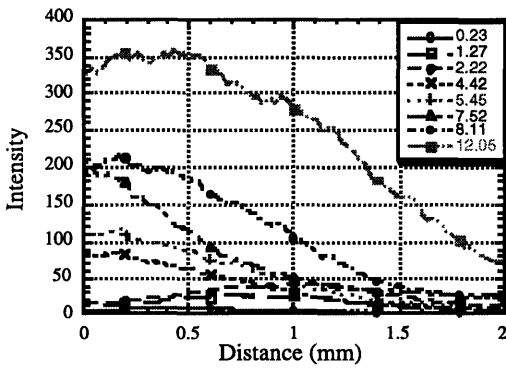


Figure C-3 (c) Experiment #9: spatial profiles of FITC-Dx 2M (left) coinjected with TR-Dx 3K (right).

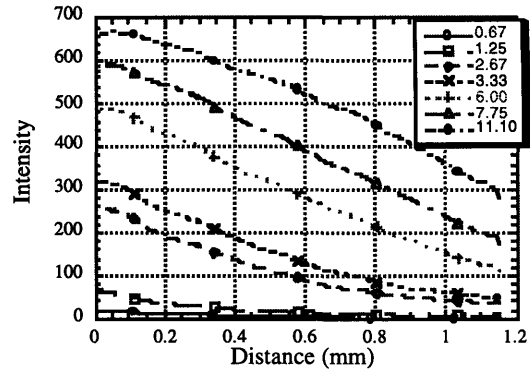
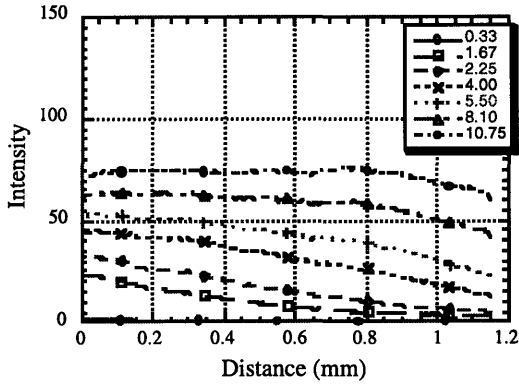


Figure C-4 (a) Experiment #10: spatial profiles of FITC-BSA (left) coinjected with TR-Dx 3K (right).

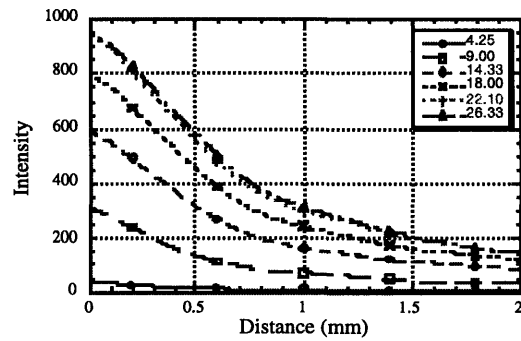
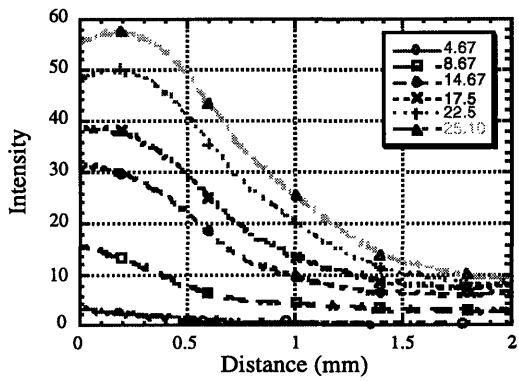


Figure C-4 (b) Experiment #11: spatial profiles of FITC-BSA (left) coinjected with TR-Dx 3K (right).

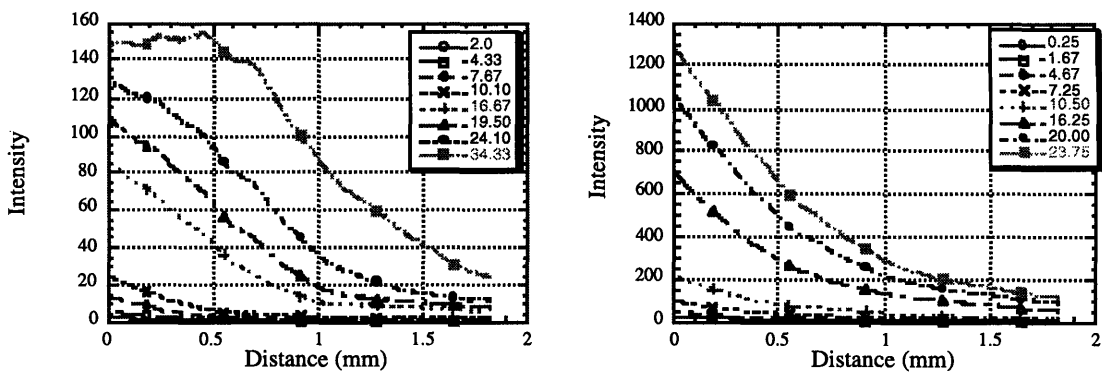


Figure C-4 (c) Experiment #12: spatial profiles of FITC-BSA (left) coinjected with TR-Dx 3K (right).

Bibliography

Aarli, B., Reed, R. K. and Aukland, K. (1991). Effect of long-standing venous stasis and hypoproteinaemia on lymph flow in the rat tail. *Acta Physiol. Scand.* **142**: 1-9.

Aarli, V. and Aukland, K. (1991). Oedema-preventing mechanisms in a low-compliant tissue: studies on the rat tail. *Acta Physiol. Scand.* **141**: 489-495.

Abernathy, V.J., Pou, A., Wilson, T.L., and Roselli, R.J. (1995). Noninvasive measurements of albumin flux into lung interstitium with increased microvascular pressure. *Am. J. Physiol.* **269**: H288-H296.

Adair, T. H., Moffatt, D. S., Paulson, A. W. and Guyton, A. C. (1982). Quantitation of changes in lymph protein concentration during lymph node transit. *Am. J. Physiol.* **243**: H351-H359.

Aris, R. and Amundson, A. (1973). *Mathematical Methods in Chemical Engineering*. Prentice-Hall, Inc., Englewood Cliffs, N.J.

Aukland, K., Kramer, G. C. and Renkin, E. M. (1984). Protein concentration of lymph and interstitial fluid in the rat tail. *Am. J. Physiol.* **247**: H74-79.

Aukland, K. and Nicolaysen, G. (1981). Interstitial fluid volume: local regulatory mechanisms. *Physiol. Rev.* **61**: 556-643.

Aukland, K. and Reed, R. K. (1993). Interstitial-lymphatic mechanisms in the control of extracellular fluid volume. *Physiol. Rev.* **73**: 1-78.

Aukland, K. and Wiig, H. (1984). Hemodynamics and interstitial fluid pressure in the rat tail. *Am. J. Physiol.* **247**: H80-H87.

Auriault, J. L. and Adler, P. M. (1995). Taylor dispersion in porous media: analysis by multiple scale expansions. *Adv. Water Res.* **18**: 217-226.

Bancroft, J. D. and Stevens, A. (1982). *Theory and Practice of Histological Techniques*. New York: Churchill Livingstone.

Barry, S. and Aldis, G. (1990). Comparison of models for flow induced deformation of soft biological tissue. *J. Biomech.* **23**: 647-654.

Barsky, S. H., Baker, A., Siegal, G. P., Togo, S. and Liotta, L. A. (1983). Use of anti-basement membrane antibodies to distinguish blood vessel capillaries from lymphatic capillaries. *Am. J. Surg. Pathol.* **7**: 667-677.

Basha, H. A. and El-Habel, F. S. (1993). Analytical solution of the one-dimensional time-dependent transport equation. *Water Resour. Res.* **29**: 3209-3214.

Bates, D. O., Levick, J. R. and Mortimer, P. S. (1994). Starling pressures in the human arm and their alteration in postmastectomy oedema. *J. Physiol.* **477**:

Baumeister, R. G. and Sivda, S. (1990). Treatment of lymphedemas by microsurgical lymphatic grafting: what is proved? *Plast. Reconstr. Surg.* **85**: 64-74.

Baxter, L. T. (1990). *Transport of fluid and macromolecules in normal and neoplastic tissue*. Pittsburgh, PA: Carnegie-Mellon University.

Bear, J. (1972). *Dynamics of Fluids in Porous Media*. Elsevier, New York.

Bergqvist, L., Strand, S.-E., and Persson, B. R. R. (1983). Particle sizing and biokinetics of interstitial lymphoscintigraphic agents. *Sem. in Nucl. Med.* **13**: 9.

Berk, D. A., Swartz, M. A., Leu, A. J. and Jain, R. K. (1996). Transport in lymphatic capillaries: II. Microscopic velocity measurement with fluorescence recovery after photobleaching. *Am. J. Physiol.* **270**: H330-337.

Berk, D. A., Yuan, F., Leunig, M. and Jain, R. K. (1993). Fluorescence photobleaching with spatial Fourier analysis: measurement of diffusion in light-scattering media. *Biophys. J.* **65**: 2428-2436.

Bert, J. and Fatt, I. (1970). Relation of water transport to water content in swelling biological membranes. In "Surface Chemistry of Biological Systems" (M. Blank, ed.), pp. 287-294. Plenum Press, New York.

Bert, J. L. and Reed, R. K. (1995). Flow conductivity of rat dermis is determined by hydration. *Biorheology* **32**: 17-27.

Blake, T. R. (1989). A theoretical view of interstitial fluid pressure-volume measurements. *Microvasc. Res.* **37**: 178-187.

Bollinger, A. (1993). Microlymphatics of human skin. *Int. J. Microcirc: Clin. Exp.* **12**: 1-15.

Bollinger, A. and Fagrell, B. (1990). *Clinical Capillaroscopy: A Guide to its Use in Clinical Research and Practice*. Hogrefe & Huber, Toronto.

Bollinger, A., Jäger, K., Sgier, F. and Segalias, J. (1981). Fluorescence microlymphography. *Circ.* **64**: 1195-1200.

Borron, P. and Hay, J. B. (1994). Characterization of ovine lymphatic endothelial cells and their interactions with lymphocytes. *Lymphology* **27**: 6-13.

Boucher, Y. and Jain, R. K. (1992). Microvascular pressure is the principal driving force for interstitial hypertension in solid tumors: implications for vascular collapse. *Cancer Res.* **52**: 5110-5114.

Brenner, H. (1980). Dispersion resulting from flow through spatially periodic media. *Phil. Trans. R. Soc. (London)* **A297**: 81-133.

Brenner, H. and Edwards, D. A. (1993). *Macrotransport Processes*. Butterworth-Heinemann, Boston.

Brodt, P. (1991). Adhesion mechanisms in lymphatic metastasis. *Cancer and Met. Rev.* **10**: 23-32.

Brodt, P., Fallavollita, L., Sawka, R. J., Shibata, P., Nip, J., Kim, U. and Shibata, H. (1990). Tumor cell adhesion to frozen lymph node sections - a correlate of lymphatic metastasis in breast carcinoma models of human and rat origin. *Breast Cancer Res. Treat.* **17**: 109-120.

Browse, N. L., Rutt, D. R., Sizeland, D. and Taylor, A. (1974). The velocity of lymph flow in the canine thoracic duct. *J. Physiol.* **237**: 401-413.

Buckley, N. D. and Carlsen, S. A. (1988). Involvement of soybean agglutinin binding cells in the lymphatic metastasis of the R3230AC rat mammary adenocarcinoma. *Cancer Res.* **48**: 512-516.

Campisi, C., Boccardo, F., Alitta, P. and Tacchella, M. (1995). Derivative lymphatic microsurgery: indications, techniques, and results. *Microsurgery* **16**: 463-468.

Carr, I. and Carr, J. (1982). Experimental models of lymphatic metastasis. In "Tumor Invasion and Metastasis" (L. A. Liotta and I. R. Hart, ed.), pp. 189-205. Nijhoff, Amsterdam.

Carr, I., Watson, P., and Pettigrew, N.M. (1989). Mechanisms of invasion and lymphatic penetration in human colorectal cancer. *Clin. Exp. Met.* **7**: 507-16.

Carr, I., Pettigrew, N.M. and Weinerman, B. (1987). Lymphatic metastasis and its treatment. *Cancer Treat. Rev.* **14**: 53-64.

Carslaw, H. S. and Jaeger, J. C. (1959). Conduction of Heat in Solids. In pp. 64. The Clarendon Press, Oxford.

Casley-Smith, J. R. (1983). Varying total tissue pressures and the concentration of initial lymphatic lymph. *Microvasc. Res.* **25**: 369-379.

Casley-Smith, J. R. (1992). Modern treatment of lymphoedema. II. The benzopyrones. *Aust. J. Dermatol.* **33**: 69-74.

Casley-Smith, J. R. and Gaffney, R. M. (1981). Excess plasma proteins as a cause of chronic inflammation and lymphoedema: quantitative microscopy. *J. Pathol.* **133**: 243-272.

Casley-Smith, J. R., Morgan, R. G. and Piller, N. B. (1993). Treatment of lymphedema of the arms and legs with 5,6-benzo-[alpha]-pyrone. *New England J. Med.* **329**: 1158-1163.

Castenholz, A. (1984). Morphological characteristics of initial lymphatics in the tongue as shown by scanning electron microscopy. *Scanning Electron Microscopy 1984* 1343-1352.

Castenholz, A., Hauck, G. and Rettberg, U. (1991). Light and electron microscopy of the structural organization of the tissue-lymphatic fluid drainage system in the mesentery: an experimental study. *Lymphology* **24**: 82-92.

Castenholz, A. and Ruhling, H. (1991). Fluorescence microscopy representation of micro-lymphologic phenomena. *Int. J. Microcirc. Clin. Exp.* **10**: 246.

Charman, W. N. and Stella, V. J., eds. (1992). *Lymphatic Transport of Drugs*. CRC Press, Boca Raton.

Chary, S. R. and Jain, R. K. (1989). Direct measurement of interstitial convection and diffusion of albumin in normal and neoplastic tissues by fluorescence photobleaching. *Proc. Natl. Acad. Sci. USA* **86**: 5385-5389.

Cornford, M. E. and Oldendorf, W. H. (1993). Terminal endothelial cells of lymph capillaries as active transport structures involved in the formation of lymph in rat skin. *Lymphology* **26**: 67-78.

Cox, P. H. (1981). The kinetics of macromolecular transport in lymph and colloid accumulation in lymph nodes. In "Progress in Radiopharmacology" (P. H. Cox, ed.), vol. 2, p. 267, Elsevier, Amsterdam.

Craik, J. E. and McNeil, I. R. R. (1965). Histological studies of stressed skin. In "Biomechanics and Related Bio-Engineering Topics." (R. M. Kenedi, ed.), Pergamon, Oxford.

Cressman, R. D. and Blalock, A. (1939). The effect of the pulse upon the flow of lymph. *Proc. Soc. Exp. Biol. Med.* **41**: 140-144.

Danckwerts, P. V. (1953). Continuous flow systems (distribution of residence times). *Chem. Eng. Sci.* **2**: 1-13.

Daroczy, J. (1995). Pathology of lymphedema. *Clinics in Dermatology* **13**: 433-444.

DeSmedt, F. and Wierenga, P. J. (1979). A generalized solution for solute flow in soils with mobile and immobile water. *Water Resour. Res.* **15**: 1137-1141.

Djoneidi, M. and Brodt, P. (1991). Isolation and characterization of rat lymphatic endothelial cells. *Microcirc. Endoth. Lymphatics* **7**: 161-181.

D.M. Eckmann, Swartz, M.A., Glucksberg, M.R., Gavriely, N. and Grotberg, J.B. (1998) Perfluorocarbon induced alterations in pulmonary mechanics. *Artificial Cells, Blood Substitutes and Immobilization Biotechnology* (in press).

Eliassen, E., Folkow, B., Hilton, S. M., Öberg, B. and Rippe, B. (1974). Pressure-volume characteristics of the interstitial fluid space in the skeletal muscle of the cat. *Acta Physiol. Scand.* **90**: 583-589.

Endo, M., Nakayama, A., Fukuta, Y., Saito, N., Segawa, K., Yokota, M., Ohya, T., Kudo, K. and Satoh, M. (1994). Enzyme-histochemical staining method for lymphatic capillaries of oral carcinomas. *Head Neck Cancer* **20**: 44-49.

Engeset, A. and Tjøtta, E. (1960). Lymphatic pathways from the tails in rats and mice. *Cancer Res.* **20**: 613-614.

Fabian, G. (1983). Investigations into the lymphatic vessels and their valves in the forelimb of the pig. *Lymphology* **16**: 172-180.

Fischer, M., Herrig, I., Costanzo, U., Wen, S., Schiesser, M., Franzeck, U. K., Hoffmann, U. and Bollinger, A. (1994). Flow velocity in single lymphatic human skin capillaries of healthy controls. Rome:

Flamion, B., Bungay, P. M., Gibson, C. C. and Spring, K. R. (1991). Flow rate measurements in isolated perfused kidney tubules by fluorescence photobleaching recovery. *Biophys. J.* **60**: 1229-1242.

Foeldi, E., Foeldi, M. and Weissleder, H. (1985). Conservative treatment of lymphedema of the limbs. *Angiol. J. Vasc. Dis.* **36**: 171.

Folkman, J. and Klagsbrun, M. (1987). Angiogenic factors. *Science* **235**: 442-447.

Frank, E. H. and Grodzinsky, A. J. (1987). Cartilage electromechanics - II. A continuum model of cartilage electrokinetics and correlation with experiments. *J. Biomech.* **20**: 629-639.

Fung, Y. C. (1981). *Biomechanics: Mechanical Properties of Living Tissues*. Springer-Verlag, New York.

Fung, Y. C. (1984). *Biodynamics: Circulation*. Springer-Verlag, New York.

Gerli, R., Iba, L. and Fruschelli, C. (1991). Ultrastructural cytochemistry of anchoring filaments of human lymphatic capillaries and their relation to elastic fibers. *Lymphology* **24**: 105-112.

Gnepp, D. R. (1976). The bicuspid nature of the valves of the peripheral collecting lymphatic vessels of the dog. *Lymphology* **9**: 75-77.

Granger, H. J. (1979). Role of the interstitial matrix and lymphatic pump in regulation of transcapillary fluid balance. *Microvascular Res.* **18**: 209-216.

Granger, H. J. (1981). Physicochemical properties of the extracellular matrix. In "Tissue Fluid Pressure and Composition" (A. R. Hargens, ed.), pp. 43-61. Williams & Wilkins, Baltimore.

Grodzinsky, A. J. (1983). Electromechanical and physicochemical properties of connective tissue. *Crit. Rev. Biomed. Eng.* **9**: 133-199.

Guyton, A. C. (1965). Interstitial fluid pressure: II. Pressure-volume curves of interstitial space. *Circ. Res.* **16**: 452-460.

Guyton, A. C. (1976). Interstitial fluid pressure and dynamics of lymph formation. *Fed. Proc.* **35**: 1861-1862.

Guyton, A. C., Sheel, K. and Murphree, D. (1966). Interstitial fluid pressure. III. Its effect on resistance to tissue fluid mobility. *Circ. Res.* **19**: 412-419.

Hagiwara, A., Ahn, T., Ueda, T., Iwamoto, A., Ueda, T., Torii, T., and Takahashi, T. (1985). Anticancer agents absorbed by activated carbon particles: a new form of dosage enhancing efficacy on lymphnodal metastases. *Anticancer Res.* **6**: 1005.

Hagiwara, A., Takahashi, T., and Oku, N. (1989). Cancer chemotherapy administered by activated carbon particles and liposomes. *Crit. Rev. Oncol. Hematol.* **9**: 319.

Hagiwara, A. and Takahashi, T. (1987). A new drug-delivery system of anticancer agents: activated carbon particles adsorbing anticancer agents. *In vivo* **1**: 241.

Hammersen, F. and Hammersen, E. (1985). On the fine structure of lymphatic capillaries. In "The Initial Lymphatics" (A. Bollinger, H. Partsch and J. H. N. Wolfe, ed.), pp. 58-65. Thieme-Verlag, Stuttgart.

Hargens, A. R. (1981). Tissue Fluid Pressure and Composition. Williams & Wilkins, Baltimore.

Hendriksen, J. H. (1985). Estimation of lymphatic conductance. *Scand. J. Clin. Lab. Invest.* **45**: 123-130.

Hirano, K., Hunt, C. A., Strubbe, A., and MacGregor, R. D. (1985). Lymphatic transport of liposome-encapsulated drugs following intraperitoneal administration: effect of lipid composition. *Pharm. Res.* **2**: 271.

Hogan, R. D. and Unthank, J. L. (1986). The initial lymphatics as sensors of interstitial fluid volume. *Microvasc. Res.* **31**: 317-324.

Hollander, W., Reilly, P. and Burrows, B. A. (1961). Lymphatic flow in human subjects as indicated by the disappearance of ¹³¹I-labeled albumin from the subcutaneous tissue. *J. Clin. Invest.* **40**: 222-233.

Holmes, M. H. (1986). Finite deformation of soft tissue: analysis of a mixture model in uni-axial compression. *J. Biomech. Eng.* **108**: 372-381.

Huang, G. K., Hu, R. Q., Liu, Z. Z., Shen, Y. L., Lan, T. D. and Pan, G. P. (1985). Microlymphaticovenous anastomosis in the treatment of lower limb obstructive lymphedema: analysis of 91 cases. *Plast. Reconstr. Surg.* **76**: 671.

Hudak, S. S. and McMaster, P. D. (1933). A study of the minute lymphatics of living skin. *J. Exp. Med.* **57**: 751-774.

Ikomi, F., Hunt, J., Hanna, G. and Schmidt-Schönbein, G. W. (1996). Interstitial fluid, plasma protein, colloid, and leukocyte uptake into initial lymphatics. *J. Appl. Physiol.* **81**: 2060-2067.

Ikomi, F., Schmid-Schönbein, G. W. and Ohhashi, T. (1994). Effects of periodic movement on lymph formation in the rabbit hindlimb. *Microcirc. Ann. Jap. Soc. Microcirc.* **10**: 183-4.

Ikomi, F., Zweifach, B. W. and Schmid-Schönbein, G. W. (1997). Fluid pressures in the rabbit popliteal afferent lymphatics during passive tissue motion. *Lymphology* **30**: 13-23.

Ivens, D., Hoe, A. L., Podd, T. J., Hamilton, C. R., Taylor, I. and Royle, G. T. (1992). Assessment of morbidity from complete axillary dissection. *Br. J. Cancer* **66**: 136-138.

Jackson, A.J. (1981). Intramuscular absorption and regional lymphatic uptake of liposome-entrapped inulin. *Drug Metab. Dispos.* **9**: 535.

Jackson, R. L., Busch, S. J. and Cardin, A. D. (1991). Glycosaminoglycans: molecular properties, protein interactions, and role in physiological processes. *Physiol. Rev.* **71**: 481-539.

Jain, R. K. (1988). Determinants of tumor blood flow: a review. *Cancer Res.* **48**: 2641-2658.

Jeltsch, M., Kaipainen, A., Joukov, V., Meng, X., Lakso, M., Rauvala, H., Swartz, M., Fukumara, D., Jain, R. and Alitalo, K. (1997). Hyperplasia of lymphatic vessels in VEGF-C transgenic mice. *Science* **276**: 1423-5.

Johnson, M., Kamm, R., Ethier, C. R. and Pedley, T. (1987). Scaling laws and the effects of concentration polarization on the permeability of hyaluronic acid. *Physicochem. Hydrodyn.* **9**: 427-441.

Jönsson, K. and Jönsson, B. (1992). Fluid flow in compressible porous media: II. Dynamic behavior. *AIChE J.* **38**: 1349-1356.

Kaipainen, A., Korhonen, J., Mustonen, T., van Hinsberg, V. W. M., Fong, G.-H., Dumont, D., Breitment, M. and Alitalo, K. (1995). Expression of the FLT4 receptor tyrosine kinase becomes restricted to lymphatic endothelium during development. *Proc. Natl. Acad. Sci. USA* **92**: 3566-3570.

Kaipainen, A., Korhonen, J., Pajusola, K., Aprelikova, O., Persico, M. G., Terman, B. I. and Alitalo, K. (1993). The related FLT4, FLT1, and KDR receptor tyrosine kinases show distinct expression patterns in human fetal endothelial cells. *J. Exp. Med.* **178**: 2077-88.

Kampmeier, O. F. (1928). The genetic history of the valves in the lymphatic system of man. *Am. J. Anat.* **40**: 413-457.

Kanter, M. A., Slavin, S. A. and Kaplan, W. D. (1990). An experimental model for chronic lymphedema. *Plast. Reconstr. Surg.* **85**: 573-580.

Kenedi, R. M., Gibson, T. and Daly, C. H. (1965). Bio-engineering studies of the human skin. In "Biomechanics and Related Bio-Engineering Topics" (R. M. Kenedi, ed.), pp. 147-158. Pergamon, Oxford.

Kim, A., Wang, C., Johnson, M., and Kamm, R. (1989). The specific hydraulic conductivity of BSA. *Biorheology* **28**: 401-419.

Kleinman, L. I. and Radford, E. P. (1964). Ventilation standards for small mammals. *J. Appl. Physiol.* **19**: 360-362.

Kukk, E., Lymboussaki, A., Taira, S., Kaipainen, A., Jeltsch, M., Joukov, V. and Alitalo, K. (1996). VEGF-C receptor binding and pattern of expression with VEGFR-3 suggests a role in lymphatic vascular development. *Development* **122**: 3829-3837.

Laurent, T. C. and Granath, K. A. (1983). The molecular weight of hyaluronate in the aqueous humour and vitreous body of rabbit and cattle eyes. *Exp. Eye Res.* **36**: 481-492.

Laurent, U. B. G., Dahl, L. B. and Reed, R. K. (1991). Catabolism of hyaluronan in rabbit skin takes place locally, in lymph nodes and liver. *Exp. Physiol.* **76**: 695-703.

Lauweryns, J. M. (1971). Stereomicroscopic funnel-like architecture of pulmonary lymphatic valves. *Lymphology* **4**: 125-132.

Leak, L. V. (1970). Electron microscopic observations on lymphatic capillaries and the structural components of the connective tissue-lymph interface. *Microvasc. Res.* **2**: 361-391.

Leak, L. V. (1976). The structure of lymphatic capillaries in lymph formation. *Fed. Proc.* **35**: 1863-1871.

Leak, L. V. and Burke, J. F. (1966). Fine structures of lymphatic capillaries and the adjoining connective tissue area. *American Journal of Anatomy* **118**: 785.

Lebel, L., Smith, L., Risberg, B., Laurent, T. C. and Gerdin, B. (1988). Effect of increased hydrostatic pressure on lymphatic elimination of hyaluronan from sheep lung. *J. Appl. Physiol.* **64**: 1327-1332.

Leu, A. J., Berk, D. A., Yuan, F. and Jain, R. K. (1994). Flow velocity in the superficial lymphatic network of the mouse tail. *Am. J. Physiol.* **267**: H1507-H1513.

Leu, H. J. and Lie, J. T. (1995). Disease of the veins and lymphatic vessels, including angiodyplasia. In "Vascular pathology" (W. E. Stehbens and J. T. Lie, ed.), pp. 489-516. Chapman & Hall Medical, London.

Levick, J. (1987). Flow through interstitium and other fibrous matrices. *Quart. Rev. Exp. Physiol.* **72**: 409-438.

Levick, J. R. (1980). Contributions of the lymphatic and microvascular systems to fluid absorption from the synovial cavity of the rabbit knee. *J. Physiol.* **306**: 445-461.

Lochter, A., and Bissell, M.J. (1995). Involvement of extracellular matrix constituents in breast cancer. *Sem. Cancer Biol.* **6**: 165-73.

Logan, J. D. (1996). Solute transport in porous media with scale-dependent dispersion and periodic boundary conditions. *J. Hydrology* **184**: 261-276.

Mandell, G. A., Alexander, M. A. and Harke, H. T. (1993). A multiscentigraphic approach to imaging of lymphedema and other causes of the congenitally enlarged extremity. *Sem. Nucl. Med.* **23**: 334-346.

Mangat, S. and Patel, H. M. (1985). Lymph node localisation of non-specific antibody-coated liposomes. *Life Sci.* **36**: 1917.

Markenscoff, X. and Yannas, I. V. (1979). On the stress-strain relation for skin. *J. Biomech.* **12**: 127-129.

McDonald, J. and Levick, J. (1993). Effect of extravascular plasma proteins on pressure-flow relations across synovium in anesthetized rabbits. *Journal of Physiology* **465**: 539-559.

McNeill, G. C., Witte, M. H., Witte, C. L., Williams, W. H., Hall, J. N., Patton, D. D., Pond, G. D. and Woolfenden, J. M. (1989). Whole-body lymphangioscintigraphy:

preferred method for initial assessment of the peripheral lymphatic system. *Radiology* **172**: 495-502.

Miserocchi, G., Pistolesi, M., Miniati, M., Bellina, C. R., Negrini, D. and Giuntini, C. (1984). Pleural liquid pressure gradients and intrapleural distribution of injected bolus. *J. Appl. Physiol.* **56**: 526-532.

Mortimer, P. S. (1997). Therapy approaches for lymphedema. *Angiology* **48**: 87-91.

Mortimer, P. S., Simmonds, R., Rezvani, M., Robbins, M., Hopewell, J. W. and Ryan, T. J. (1990). The measurement of skin lymph flow by isotope clearance - reliability, reproducibility, injection dynamics, and the effect of massage. *J. Invest. Dermatol.* **95**: 677-682.

Mow, V. C., Holmes, M. H. and Lai, W. M. (1984). Fluid transport and mechanical properties of articular cartilage: a review. *J. Biomech.* **17**: 377-394.

Mow, V. C., Kwan, M. K., Lai, W. M. and Holmes, M. H. (1986). A finite deformation theory for nonlinearly permeable hydrated soft biological tissues. In "Frontiers in Biomechanics" (G. W. Schmid-Schönbein, S. L.-Y. Woo and B. W. Zweifach, ed.), pp. 153-179. Springer, New York.

Murphy, G. M. (1960). Ordinary Differential Equations and Their Solutions. D. Van Nostrand Company, Inc., Princeton, N.J.

Negrini, D., Ballard, S. T. and Benoit, J. N. (1994). Contribution of lymphatic myogenic activity and respiratory movements to pleural lymph flow. *J. Appl. Physiol.* **76**: 2267-2274.

Negrini, D., Passi, A., de Luca, G. and Miserocchi, G. (1996). Pulmonary interstitial pressure and proteoglycans during development of pulmonary edema. *Am. J. Physiol.* **270**: H2000-2007.

Netti, P. A., Baxter, L. T., Boucher, Y., Skalak, R. and Jain, R. K. (1997). Macro- and microscopic fluid transport in living tissues: application to solid tumors. *AIChE J.* **43**: 818-834.

Nicoll, P. A. and Taylor, A. E. (1977). Lymph formation and flow. *Annu. Rev. Physiol.* **39**: 73-95.

O'Brien, B. M., Mellow, C. G., Khazanchi, R. K., Dvir, E., Kumar, V. and Pederson, W. C. (1990). Long-term results after microlymphaticovenous anastomoses for the treatment of obstructive lymphedema. *Plast. Reconstr. Surg.* **85**: 562-572.

Ohtani, O., Ohtsuka, A. A. and Owen, R. L. (1986). Three-dimensional organization of the lymphatics in the rabbit appendix: A scanning electron and light microscopic study. *Gastroenterology* **91**: 947-955.

Ohsawa, T., Matsukawa, Y., Takakura, Y., Hashida, M., and Sezaki, H. (1985). Fate of lipid and encapsulated drug after intramuscular administration of liposomes prepared by the freeze-thawing method in rats. *Chem. Pharm. Bull.* **33**: 5013.

Parsons, R. J. and McMaster, P. D. (1938). The effect of the pulse upon the formation and flow of lymph. *J. Exp. Med.* **68**: 353-376.

Patel, H.M. (1988). Fate of liposomes in the lymphatics. In: "Liposomes as drug carriers" (G. Gregoriadis, ed.), p. 51. John Wiley and Sons, New York.

Pepper, M. S., Wasi, S., Ferrara, N., Orci, L. and Montesano, R. (1994). In vitro angiogenic and proteolytic properties of bovine lymphatic endothelial cells. *Exp. Cell Res.* **210**: 298-305.

Pertovaara, L., Kaipainen, A., Ferrara, N., Saksela, O. and Alitalo, K. (1994). Vascular endothelial growth factor is induced in response to transforming growth factor-beta in fibroblastic and epithelial cells. *J. Biol. Chem.* **269**: 6271-6274.

Pezner, R. D., Patterson, M. P., Hill, L. R., Lipsett, J. A., Desai, K. R., Vora, N., Wong, J. Y. and Luk, K. H. (1986). Arm lymphedema in patients treated conservatively

for breast cancer: relationship to patient age and axillary node dissection technique. *Int. J. Rad. Oncol. Biol. Phys.* **12**: 2079-83.

Piller, N. B. and Casley-Smith, J. R. (1975). The effect of coumarin on protein and PVP clearance from rat legs with various high protein oedemas. *Br. J. Exp. Path.* **56**: 439-445.

Prehm, P. (1984). Hyaluronate is synthesized at plasma membranes. *Biochem. J.* **220**: 597-600.

Preston, B. N., Laurent, T. C. and Comper, W. D. (1984). Transport of molecules in connective tissue polysaccharide solutions. In "Molecular Biophysics of the Extracellular Matrix" (S. Arnott, D. A. Rees and E. R. Morris, ed.), pp. 119-162. Humana, Clifton, NJ.

Puckett, C. L., Jacob, G. R., Hurvitz, J. S. and Silver, D. (1980). Evaluation of lymphovenous anastomoses in obstructive lymphedema. *Plast. Reconstr. Surg.* **66**: 562.

Reddy, N. P., Krouskop, T. A. and Newell, P. H. (1975). A note on the mechanisms of lymph flow through the terminal lymphatics. *Microvasc. Res.* **10**: 214-216.

Reed, R. K., Laurent, U. B. G., Fraser, J. R. E. and Laurent, T. C. (1990). Hyaluronan in prenodal lymph from skin: changes with lymph flow. *Am. J. Physiol.* **259**: H1097-H1100.

Reed, R. K., Lepsoe, S. and Wiig, H. (1989). Interstitial exclusion of albumin in rat dermis and subcutis in over- and dehydration. *Am. J. Physiol.* **257**: H1819-1827.

Reed, R. K. and Rodt, S. A. (1991). Increased negativity of interstitial fluid pressure during the onset stage of inflammatory edema in rat skin. *Am. J. Physiol.* **260**: H985-H991.

Renkin, E. M. and Wiig, H. (1994). Limits to steady-state lymph flow rates derived from plasma-to-tissue uptake measurements. *Microvasc. Res.* **47**: 318-328.

Roscoe, B. (1966). *Biology of the Laboratory Mouse*. Blakiston Division, McGraw-Hill, New York.

Rubinstein, J. and Mauri, R. (1986). Dispersion and convection in periodic porous media. *SIAM J. Appl. Math.* **46**: 1018-1023.

Ryan, T. J. (1989). Structure and function of lymphatics. *J. Invest. Dermatol.* **93**: 18S-24S.

Ryman, B. E., Jewkes, R. F., Jeyasingh, K., Osborne, M. P., Patel, H. M., Richardson, V. J., Tattersall, M. H. N., and Tyrell, D. A. (1978). Potential Applications of liposomes to therapy. *Ann. N.Y. Acad. Sci.* **308**: 281.

Savage, R. C. (1984). The surgical management of lymphedema. *Surg. Gynecol. Obstet.* **159**: 501-8.

Schmid-Schönbein, G. W. (1990). Microlymphatics and lymph flow. *Physiol. Rev.* **70**: 987-1028.

Simon, B. R. (1992). Multiphase poroelastic finite element models for soft tissue structure. *Appl. Mech. Rev.* **45**: 191-218.

Simon, J. R., Gough, A., Urbanik, E., Wang, F., Lanni, F., Ware, B. R. and Taylor, D. L. (1988). Analysis of rhodamine and fluorescein-labelled F-actin diffusion in vitro by fluorescence recovery after photobleaching. *Biophys. J.* **59**: 801-815.

Skalak, T. C., Schmid-Schönbein, G. W. and Zweifach, B. W. (1984). New morphological evidence for a mechanism of lymph formation in skeletal muscle. *Microvasc. Res.* **28**: 95-112.

Slavin, S. A., Upton, J., Kaplan, W. D. and Van den Abbeele, A. D. (1997). An investigation of lymphatic function following free-tissue transfer. *Plast. Reconstr. Surg.* **99**: 730-741.

Smith, A. R., van Allphen, W. A. and Van Der Pompe, W. B. (1987). Lymphatic drainage in patients after replantation of extremities. *Plast. Reconstr. Surg.* **79**: 169.

Strand, S.-E. and Bergqvist, L. (1989). Radiolabeled colloids and macromolecules in the lymphatic system. *CRC Crit. Rev. Ther. Drug Carrier Syst.* **6**: 211.

Swabb, E. A., Wei, J. and Gullino, P. M. (1974). Diffusion and convection in normal and neoplastic tissues. *Cancer Res.* **34**: 2814-2822.

Swartz, M. A., Berk, D. A. and Jain, R. K. (1996). Transport in lymphatic capillaries: I. Macroscopic measurement using residence time distribution analysis. *Am. J. Physiol.* **270**: H324-329.

Takada, M. (1971). The ultrastructure of lymphatic valves in rabbits and mice. *Am. J. Anat.* **132**: 207-218.

Taylor, G. I. (1953). Dispersion of soluble matter in solvent flowing slowly through a tube. *Proc. Soc. Lond.* **A219**: 186-203.

Torchilin, V. P. (1996). Affinity liposomes *in vivo*: factors influencing target accumulation. *J. Molec. Recognition* **9**: 335-346.

Tumer, A., Kirby, C., Senior, J., and Gregoriadis, G. (1983). Fate of cholesterol-rich liposomes after subcutaneous injection into rats. *Biochim. Biophys. Acta* **760**: 119.

Ullrich, A. and Schlessinger, J. (1990). Signal transduction by receptors with tyrosine kinase activity. *Cell* **61**: 203-212.

154. Watson, K. K. and Jones, M. J. (1984). Algebraic equations for solute movement during absorption. *Water Resour. Res.* **20**: 1131-1136.

Watson, P. D. and Grodins, F. S. (1978). An analysis of the effects of the interstitial matrix on plasma-lymph transport. *Microvasc. Res.* **16**: 19-41.

Weinstein, J.N. (1984). Liposomes as drug carriers in cancer chemotherapy. *Cancer Treat. Rep.* **68**: 127.

Wen, S., Dörffler-Melly, J., Herrig, I., Schiesser, M., Franzeck, U. K. and Bollinger, A. (1994). Fluctuation of skin lymphatic capillary pressure in controls and in patients with primary lymphedema. *Int. J. Microcirc.* **14**: 139-143.

Wieringa, P. A., Van Putten, M. J. A. M. and Duling, B. R. (1993). A technique for the estimation of plasma flow in single capillaries using photobleached dyes. *Microvasc. Res.* **46**: 263-282.

Wiig, H., DeCarlo, M., Sibley, L. and Renkin, E. M. (1992). Interstitial exclusion of albumin in rat tissues measured by a continuous infusion method. *Am. J. Physiol.* **263**: H1222-H1233.

Wiig, H. and Reed, R. (1987). Volume-pressure relationship of interstitium in dog skin and muscle. *Am. J. Physiol.* **253**: H291-H298.

Wiig, H. and Reed, R. K. (1981). Compliance of the interstitial space in rats. II. Studies on skin. *Acta Physiol. Scand.* **113**: 307-315.

Wiig, H. and Reed, R. K. (1985). Interstitial compliance and transcapillary Starling pressures in cat skin and skeletal muscle. *American Journal of Physiology* **248**: H666-H673.

Wiig, H., Reed, R. K. and Aukland, K. (1981). Micropuncture measurement of interstitial fluid pressure in rat subcutis and skeletal muscle: comparison to wick-in-needle technique. *Microvasc. Res.* **21**: 308-319.

Yates, S. R. (1990). An analytical solution for one-dimensional transport in heterogeneous porous media. *Water Resour. Res.* **26**: 2331-2338.

Yates, S. R. (1992). An analytical solution for one-dimensional transport in porous media with an exponential dispersion function. *Water Resour. Res.* **28**: 2149-54.

Yong, L. C. and Jones, B. E. (1991). A comparative study of cultured vascular and lymphatic endothelium. *Exp. Pathol.* **42**: 11-25.

Yoshikawa, H., Nakao, Y., Takada, K., Muranishi, S., Wada, R., Tabata, Y., Hyon, S.-H., and Ikada, Y. (1989). Targeted and sustained delivery of aclarubicin to lymphatics by lactic-acid oligomer microspheres in rat. *Chem. Pharm. Bull.* **37**: 802.

Yoshizawa, M., Shingaki, S., Nakajima, T. and Saku, T. (1994). Histopathological study of lymphatic invasion in squamous cell carcinoma (O-1N) with high potential of lymph node metastasis. *Clin. Exp. Metastasis* **12**: 347-356.

Zaugg-Vesti, B., Dörffler-Melly, J., Spiegel, M., Wen, S., Franzeck, U. K. and Bollinger, A. (1993). Lymphatic capillary pressure in patients with primary lymphedema. *Microvasc. Res.* **46**: 128-134.

Zelikovski, A., Haddad, M. and Reiss, R. (1986). The "Lympha-Press" intermittent sequential pneumatic device for the treatment of lymphoedema: five years of clinical experience. *J. Cardiovasc. Surg.* **27**: 288-90.

Zweifach, B. W. and Prather, J. W. (1975). Micromanipulation of pressure in terminal lymphatics in the mesentery. *Am. J. Physiol.* **228**: 1326-1335.